



Review

Applications of cosmic-ray muons

G. Bonomi^{a,b,*}, P. Checchia^c, M. D'Errico^{d,e}, D. Pagano^{a,b}, G. Saracino^{d,e}^a Department of Mechanical and Industrial Engineering, University of Brescia, Italy^b Istituto Nazionale di Fisica Nucleare (INFN), Pavia, Italy^c Istituto Nazionale di Fisica Nucleare (INFN), Padova, Italy^d Department of Physics, University of Napoli "Federico II", Italy^e Istituto Nazionale di Fisica Nucleare (INFN), Napoli, Italy

ARTICLE INFO

Article history:

Available online 24 February 2020

Keywords:

Cosmic-ray muons
Muon radiography
Muon tomography
Muon metrology
Muography
Particle detectors

ABSTRACT

Applications of cosmic-ray muons have grown in numbers in the last decades. This was possible thanks to the development of detectors and techniques employed in particle and nuclear physics. Indeed the first famous application, the scanning of the Chephren's pyramid, was performed by L. W. Alvarez, that was a great expert in particle detectors and indeed was awarded a Nobel prize for his work on the hydrogen bubble chambers. After a first period in which the applications exploited mainly the absorption of the cosmic-ray muons when crossing a structure under investigation, more recently also the deflection of the muons has been used to design new applications. Nowadays more and more groups around the world are working on this research field. In the present review, after an introduction on cosmic-ray muons, the principles of the interaction of muons with matter will be briefly summarised. This description is important to classify the applications in three main categories: *muon radiography*, *muon tomography* and *muon metrology*. In the following, for each class, an overview of the basic ideas and a detailed description of the technologies will be presented along with a list of past and present applications.

© 2020 Elsevier B.V. All rights reserved.

Contents

1.	Introduction.....	2
2.	Cosmic rays.....	3
2.1.	Primary and secondary cosmic rays.....	3
2.2.	Interaction with matter.....	4
2.2.1.	Energy loss.....	4
2.2.2.	Multiple Coulomb scattering.....	6
2.3.	Simulation tools.....	8
3.	Detectors.....	8
3.1.	Detectors for muon radiography.....	8
3.1.1.	Nuclear emulsion detectors.....	9
3.1.2.	Scintillation detectors.....	9
3.1.3.	Gaseous detectors.....	9
3.2.	Detectors for muon tomography.....	10
3.2.1.	Gaseous detectors.....	10

* Corresponding author at: Department of Mechanical and Industrial Engineering, University of Brescia, Italy.
E-mail address: germano.bonomi@unibs.it (G. Bonomi).

3.2.2.	Momentum measurement.....	10
3.2.3.	An example of a detector for MCS tomography.....	11
4.	Muon radiography.....	11
4.1.	Introduction.....	11
4.2.	Basic principles.....	13
4.2.1.	The muon spectrum.....	14
4.2.2.	Density distribution measurement.....	14
4.2.3.	Relative transmission for the detection of cavities.....	15
4.2.4.	Feasibility studies.....	16
4.2.5.	Angular aperture, resolutions and geometrical acceptance of a typical detector.....	17
4.2.6.	3D imaging.....	17
4.2.7.	Joint inversion of muographic and gravimetry data.....	18
4.2.8.	Back-projection method.....	20
4.2.9.	3D modelling of a cavity.....	20
4.2.10.	Background.....	20
4.3.	The study of volcanoes.....	23
4.3.1.	Volcanoes in Japan.....	23
4.3.2.	Volcanoes in Italy.....	24
4.3.3.	Volcanoes in France.....	26
4.4.	Geological applications.....	26
4.4.1.	Mineral exploration.....	27
4.4.2.	Monitoring of carbon dioxide geo-storage.....	27
4.4.3.	Bedrock profiles in glaciers.....	28
4.4.4.	Fault lines and hydrogeological measurements.....	28
4.5.	Detection of cavities for archaeological and civil engineering applications.....	29
4.5.1.	Exploring the interior of pyramids.....	29
4.5.2.	Underground cavities and tunnels.....	29
4.6.	Industrial applications.....	30
5.	Muon tomography.....	31
5.1.	Basic principles.....	31
5.1.1.	Algorithms for 3D imaging.....	31
5.2.	Experimental results.....	34
5.3.	Main applications: state of the art.....	35
5.3.1.	Transport controls.....	35
5.3.2.	Industrial applications.....	35
5.3.3.	Nuclear controls.....	36
5.3.4.	Historical building controls.....	37
5.4.	A detailed example: the inspection of dry storage casks.....	37
6.	Muon metrology.....	39
6.1.	Introduction.....	39
6.2.	Cosmic muons for the alignment of tracking detectors.....	40
6.2.1.	Introduction to track-based alignment.....	41
6.2.2.	The Millepede and Millepede II algorithms.....	41
6.2.3.	Alignment of the CMS tracker with cosmic muons.....	42
6.3.	The stability monitoring of historical buildings with cosmic muons.....	43
6.3.1.	The method.....	44
6.3.2.	Results.....	44
7.	Summary and conclusions.....	45
	References.....	46

1. Introduction

Cosmic-ray muons is a general expression to indicate muons that drop on Earth due to cosmic radiation. A description of the origin of such particles along with the physical processes of interaction with matter is given in Section 2. The world knew that it was possible to inspect the content of a large structure with such cosmic-ray muons in 1970, when Nobel prize winner Luis W. Alvarez investigated the interior of the Chephren's pyramid at Giza, looking for hidden and unknown chambers in the stonework. The result of the study was that *"no chambers with volumes similar to the known chambers in Cheops's and Snereru's pyramids exist in the mass of limestone investigated by cosmic-ray absorption"* [1]. Nevertheless the endeavour received great attention from the media and the public. In his Article Alvarez reported that indeed his one was not the first application of cosmic-ray muons in history, since previously, in 1955, E. P. George [2] gave *"an independent measure of the thickness of rock overlying an underground powerhouse in Australia's Snowy Mountains Scheme"*. Another application of cosmic-ray muons was introduced in 1995 when Nagamine and collaborators [3] performed measurements

on Mt. Tsukuba proving that “nearly horizontal cosmic-ray muons can be used to explore the inner-structure of a gigantic geophysical substance, such as the top region of a volcano”.

All these first applications were based on the measurement of the attenuation of the cosmic-ray muons flux. By counting the number of muons exiting the volume under inspection and assuming the composition of the crossed material, the total thickness of the material could be inferred. The details and an extensive overview of all the possible applications are presented and described below in Section 4. In the following we will refer to this technique as either **muon radiography** or **muon absorption radiography**, since it is based on the effects of “absorption/transmission” similarly to common x-ray radiography. Alternatively, in brief, it will also be cited as **muography**.

As described in Section 2.2, the energy loss and the consequent absorption of muons it is not the only effect of the passage through matter. Indeed, in 2003 a Los Alamos research group [4] proposed an innovative idea, to use the scattering angle of the surviving muons to measure the properties of the crossed material. Clearly both the incoming and the outgoing trajectories of the cosmic-ray muons need to be measured. In this case, a three-dimensional image of the volume under investigation can be obtained. This novel approach opened up new scenarios and, since then, more and more groups are investigating the possibility to apply such methods for new applications. The technique, based on the *scattering* effect, in the following is referred to as **muon tomography** or more extensively and more precisely **muon scattering tomography** or **muon MCS tomography**, where MCS stands for Multiple Coulomb Scattering. Indeed muon tomography can also be achieved through multiple-views muon radiography as described below. The details and an extensive overview of all the possible applications of muon tomography are presented and described below in Section 5. In the literature the term *muography* is sometime used to name both muon radiography and muon tomography, while in the present report it is used as a more general and more appropriate, for various reasons as it will be clear in the following, definition of muon radiography.

In addition to muon radiography and muon tomography, recently another way to use the cosmic-ray muons for civil applications has been suggested [5]. Basically, even if each cosmic-ray muon is deviated from its original course, as described in Section 2.2, for a sample of many particles the mean scattering angle is zero. In other words, *on average*, they travel along straight paths. Similarly to what it is done with laser positioning systems, it is thus possible to estimate the relative position of different parts of a given structure. Since decades this approach is indeed quite typical in experiments of particle and nuclear physics for the calibration and the alignment of their apparatuses. This technique is referred to as **muon metrology** and an overview is given in Section 6.

All cosmic-ray muons applications share the common fact that they need a detector to reveal and measure the passage of muons. Due to different requirements, nevertheless, the detectors may have specific characteristics for each application. An overview of the possible technologies and class of detectors is given in Section 3.

The overall research field of applications of cosmic-ray muons has experienced a sensible growth especially in the last decade. This fact can be summarised by the distribution of the number of publications containing “muon and radiography”, “muon and tomography” or “muography” in the title as a function of time as shown in Fig. 1. Because of the number of projects and research developments, the ensemble of applications described in this article, though extensive, may be not exhaustive.

2. Cosmic rays

2.1. Primary and secondary cosmic rays

The Earth, as all other planets in the Universe, is hit by particles and nuclei that originate from different sources, mainly from astrophysical sources like supernovae. Such particles are generally called *primary cosmic rays*¹ and can be characterised by very high energies. When they interact with the atmosphere they undergo nuclear reactions generating a cascade of processes that leads to the creation of a *shower* of many particles. The air shower, in general, has a hadronic core that on the other hand operates as a source for electromagnetic subshowers. In particular decays of π^0 into two γ 's determine the creation of many electron-positron pairs, that are the most numerous charged particles in the shower. At high altitude the presence of muons, from the decay of charged pions, is one order of magnitude lower. These muons, nevertheless, have a mean lifetime of about 2 μ s and, at the speed of light, they are able to reach the Earth's surface. All the particles belonging to the air shower are generally called *secondary cosmic rays*. They were discovered at the beginning of the 20th century by Pacini [6], Hess [7] and other physicists when investigating on the electric conductivity of air. They gradually realised that, using Pacini's words, “a sizeable cause of ionisation exists in the atmosphere, originating from penetrating radiation, independent of the direct action of radioactive substances in the crust.”. It was Millikan that for the first time, after these experiments, called this extraterrestrial radiation *cosmic rays*. The cosmic rays, after discovery and for few decades before the takeover of particle accelerators, have been the main instrument for the early development of particle physics. From 1932 through 1950 many new particles were discovered studying the cosmic rays, such as the positron [8], the muon [9], the π mesons [10], the K mesons [11] and the Λ baryons [12].

¹ Technically *primary cosmic rays* are only the particles originating from astrophysical sources while those produced in interaction with the interstellar gas are considered *secondaries*. Literally electrons, protons, helium and other nuclei synthesised in stars are primaries. Nevertheless, for the purposes of this report everything hitting the atmosphere from outside will be considered, in the following, as *primary*.

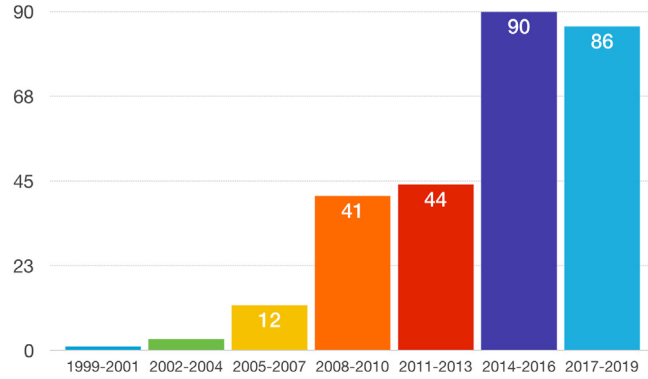


Fig. 1. Number of publications regarding muon radiography or muon tomography in the last years. The search has been performed on Scopus looking for “Muon AND tomography”, “Muon AND radiography” OR “Muography” in the title of publications.

Even if the relative composition varies as a function of the kinetic energy, overall, about 99% of the primary cosmic rays are nuclei and about 1% single electrons. There is also a tiny fraction of antimatter, such as positrons and antiprotons. Among the nuclei, protons are the more abundant (90%), followed by helium (9%) while the remaining 1% is due to nuclei of heavier elements [13]. Neutrinos are not considered here and in the following. The composition of the secondaries, on the other hand, varies as a function of the altitude. Above 5–6 km of altitude protons are more abundant than muons while at about 2 km the muons are about 10 times more. At the sea level protons are 2 orders of magnitude less frequent than muons ([13] and references therein). Other particles reach the Earth surface, such as electrons, pions, protons and neutrons but their fraction is, in general, negligible with respect to muons. For this reason and for the purposes of this review, in the following the terms *muons*, *cosmic rays*, *cosmic muons* and *cosmic-ray muons*, somehow improperly, will be anyhow used as synonymous.

The flux of muons at sea level, with a momentum greater than 1 GeV/c, has been measured to be around $60\text{--}70\text{ m}^{-2}\text{ s}^{-1}\text{ sr}^{-1}$ ([13] and references therein). As a general statement, it can be said that 10 000 of muons per minute and per square (horizontal) meter, or alternatively $\sim 170\text{ Hz/m}^2$, hit the ground [13]. On average about 600 of them cross a human body every minute. Another easy to remember rule of thumb is that 1 muon per second intercepts the palm of a hand. These are indicative values, since the flux depends on many variables such as altitude, solar activity, Earth and solar magnetic field and other factors. The average energy is comprised between 3 and 4 GeV and the flux is maximum at the zenith (vertical direction) and it scales approximately with $\cos^2(\theta)$, θ being the angle with respect to the vertical. The flux as a function of the muon momentum is shown in Fig. 2 [14].

2.2. Interaction with matter

To better comprehend the applications of cosmic-ray muons, it is important to describe what happens when they cross the matter. Passage of muons through a given material determines (I) a loss of their energy and (II) a deflection of their incident direction. These effects are primarily due to collective results of two processes, inelastic collisions with the atomic electrons and elastic scattering from nuclei. Other processes, such as emission of Cherenkov radiation, bremsstrahlung and nuclear reactions, can give contributions in specific energy ranges (see for example [13] and [15] for a more exhaustive description).

2.2.1. Energy loss

The energy loss is expressed through the so called *mass stopping power*, $\langle -dE/dX \rangle$, as defined in Eq. (1) in units of $\text{MeV g}^{-1}\text{ cm}^2$. The dX that appears in the denominator is indeed the product $dx \cdot \rho$, being ρ the density of the crossed materials in g/cm^3 . Expressed in this way, the mass stopping power is practically independent on the material the particle is crossing. In the following $X = x \cdot \rho$ is also called *opacity*. The mean rate of energy loss per unit path length, namely the *linear stopping power*, in MeV cm^{-1} , is thus $\langle -dE/dx \rangle = \langle -dE/dX \rangle \rho$. As an example the mass stopping power as a function of $\beta\gamma = p/Mc$ (where p is the momentum and M the mass) and of the muon momentum is shown in Fig. 3 for positive muons in copper [13]. The region between $0.1 \leq \beta\gamma \leq 1000$, for intermediate-Z materials, is well-described by the “Bethe–Bloch equation”, first published in 1930 [16] and then modified to account for better approximations (see for example [13] and [15]), with an accuracy of a few percent. The Bethe–Bloch equation, can be expressed as

$$\left\langle -\frac{dE}{dX} \right\rangle = Kz^2 \frac{Z}{A} \frac{1}{\beta^2} \left[\frac{1}{2} \ln \frac{2m_e c^2 \beta^2 \gamma^2 W_{\max}}{I^2} - \beta^2 - \frac{\delta(\beta\gamma)}{2} \right] \quad (1)$$

where K is a proportionality coefficient, z the charge number of the incident particle ($z = 1$ for muons), Z and A the atomic number and mass of the absorber, I the mean excitation energy, m_e the mass of the electron, W_{\max} the maximum energy

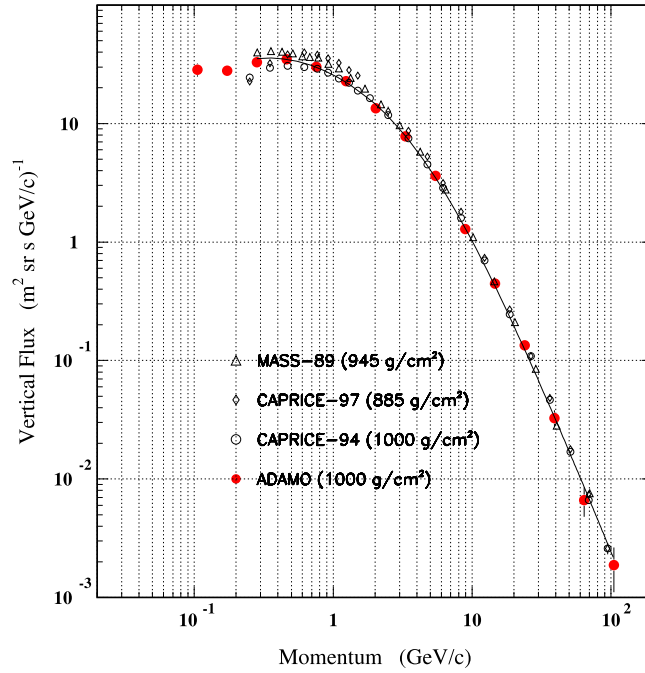


Fig. 2. Spectrum of muons ([14] and references therein) as a function of the muon momentum.
Source: Courtesy of L. Bonechi.

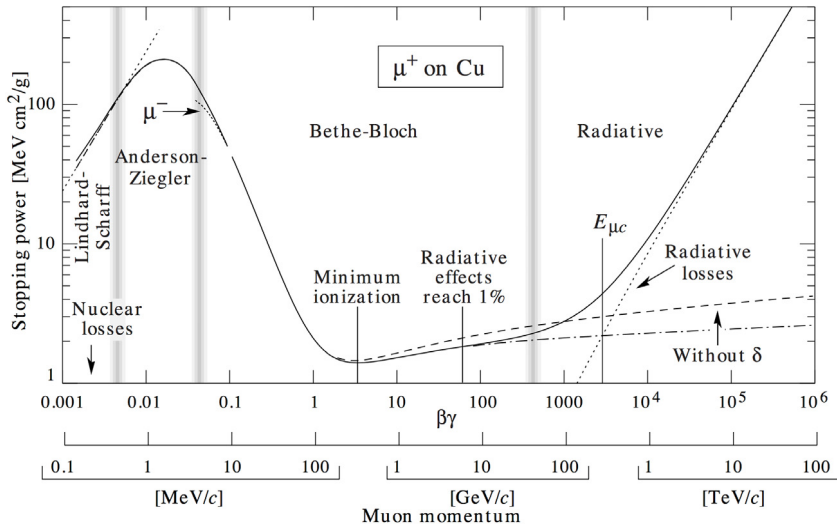


Fig. 3. Mass stopping power ($= -dE/dX$) for positive muons in copper as a function of $\beta\gamma = p/Mc$ over nine orders of magnitude in momentum (12 orders of magnitude in kinetic energy) as reported in [13]. Solid curves indicate the total stopping power. Vertical bands indicate boundaries between different approximations. The short dotted lines labelled “ μ^- ” illustrate the “Barkas effect”, the dependence of stopping power on projectile charge at very low energies.

transfer in a single collision and $\delta(\beta\gamma)$ the density effect correction to ionisation energy loss. At non-relativistic energies, $\langle -dE/dX \rangle$ is dominated by an overall $1/\beta^2$ factor and decreases with increasing velocity until about $v = 0.96 c$, where a minimum is reached. The stopping power function is then characterised by a broad minimum whose position drops from $\beta\gamma = 3.5$ to 3.0 as Z goes from 7 to 100 . In practical cases, most relativistic particles, such as cosmic-ray muons, have mean energy loss rates close to the minimum. Particles at this point are known as *minimum ionising particles* or in brief *mips*. The mean energy loss rate in this region for various materials is shown in Fig. 4 [13].

The $\langle dE/dX \rangle$ we have presented so far applies to pure elements. In general a mixture or compound can be described as a succession of thin layers of pure elements. In this case a good approximate value can be calculated by averaging over

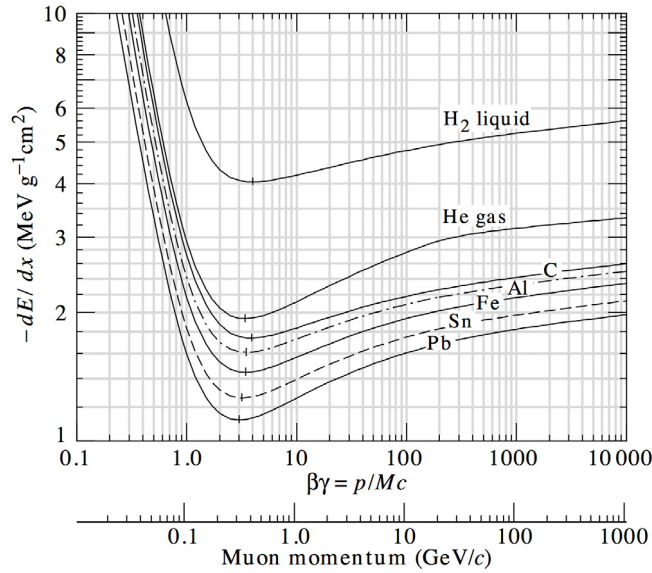


Fig. 4. Mean energy loss rate in liquid hydrogen, gaseous helium, carbon, aluminum, iron, tin, and lead. Radiative effects, relevant for muons in iron for $\beta\gamma \geq 1000$ and at lower momenta in higher-Z absorbers, are not included.

Source: Fig. from [13].

each element in the compound (Bragg's additivity), that is

$$\frac{1}{\rho} \frac{dE}{dx} = \sum_i \frac{w_i}{\rho_i} \left(\frac{dE}{dx} \right)_i$$

where w_i is the fraction by weight of the i th element in the compound.

Given the (dE/dx) , in practical applications it is important to know how far muons can penetrate in matter before they lose all their energy, or saying it differently, before they are stopped and absorbed. This path is known as the *range* of the particle and it clearly depends on the type of material and on the incoming muon energy. Useful information and tables about muon stopping power and range can be found in [17]. In general it is common use to express the range in units of $\text{g cm}^{-2} \text{ GeV}^{-1}$ (R) and in the form of R/M , where M is the mass of the incident particle. Since the overall effect of slowing down is due to many collisions with electrons, muons with the same energy and crossing the same thickness will have different ranges. This phenomenon is known as *range straggling* and the corresponding distribution is in first approximation Gaussian. The fractional range straggling defined as $\sqrt{\text{variance}(\text{range})}/\text{range}$ is inversely proportional to the square root of the mass of the particle, so that, for muons with respect to more massive particles such as the proton, is not negligible. The fractional straggling depends on the energy of the muon and on the material crossed and it can be of few percent (see [17] for details). The thickness that determines the absorption of all the particles is also called *practical range*. R/M as a function of $\beta\gamma = p/Mc$ is shown for a variety of materials in Fig. 5 [13]. To calculate the range in units of cm, R/M needs to be divided by the density of the material and multiplied by the mass of the particle (in units of GeV/c^2). As an example a 1 GeV muon penetrates many meters through light materials, but can be stopped in about half a meter in heavy materials similar to lead. The muon range in rock is important for the application of muon radiography by absorption and is described with some details in 4.2.

2.2.2. Multiple Coulomb scattering

The deflection of the cosmic-ray muon when crossing a given material is mostly due to repeated elastic Coulomb scatterings from nuclei. Each collision, in general, results in a small angular deflection of the muon. As a cumulative effect, the incident particle is scattered and moves along in a random course exiting with a net deflection from the original direction. An extensive treatment of the effect can be found in [13] and [15]. The process of Coulomb scattering in matter, mathematically, can be treated differently, depending on the thickness of the crossed material, as *single*, *plural* or *multiple* scattering. Since in applications of the cosmic-ray muons the thicknesses are not *small*, only the multiple scattering approximation is important and will be described here. The effect is summarised in Fig. 6 along with some variables used to describe the multiple Coulomb scattering (MCS). In this case, where the average number of scatterings is greater than 20 and the energy loss is small, a probability distribution of the deflection as a function of the thickness can be obtained treating the process statistically, such as in the theory of Molière [19]. In the literature detailed and accurate formulations and reviews have been presented by various authors, for example [20] and [21]. In the following the description of the phenomenon reported in [13] will be presented. This formulation is generally valid for particles

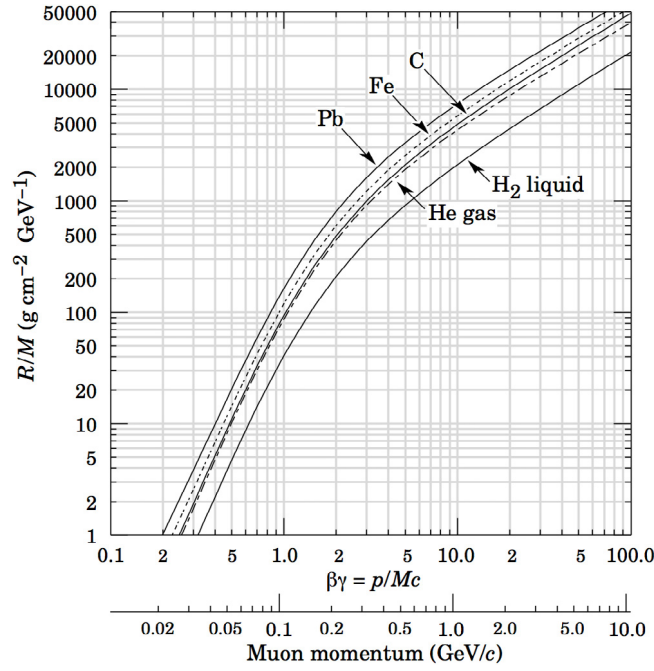


Fig. 5. Range of muons in liquid (bubble chamber) hydrogen, helium gas, carbon, iron, and lead.
Source: Fig. from [13].

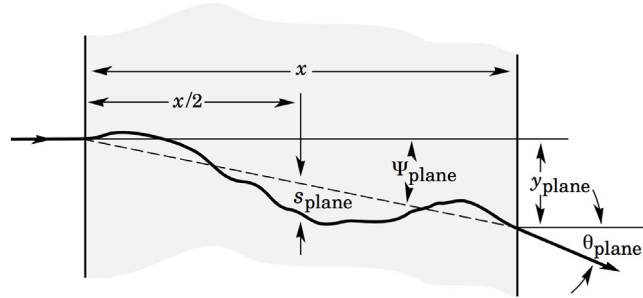


Fig. 6. Quantities used to describe multiple Coulomb scattering (Fig. from [18]). The particle is incident in the plane of the figure.

with a net deflection up to angles of $\theta \sim 30^\circ$ [15]. For many applications the net scattering distribution, and also the displacement distribution, can be approximated by a Gaussian via the central limit theorem. Such approximation does not take into account the less frequent “hard” scatters responsible for non-Gaussian tails. Usually such events account only for a few percent of the total. The root mean square (rms) of the Gaussian approximation of the projected angular distribution has been calculated in [22] and can be expressed as follows:

$$\sigma_\theta = \frac{13.6 \text{ MeV}}{\beta c p} z \sqrt{\frac{x}{X_0}} \left[1 + 0.038 \ln \left(\frac{x z^2}{X_0 \beta^2} \right) \right] \quad (2)$$

where p , βc , and z are the particle momentum, velocity, and charge (for the muons $z = 1$), x is the thickness of the scattering medium, $\sigma_\theta = \theta_{\text{plane}}^{\text{rms}} = 1/\sqrt{2} \theta_{\text{space}}^{\text{rms}}$ and X_0 , the material radiation length, is given by:

$$X_0 = 716.4 \text{ g/cm}^2 \frac{A}{Z(Z+1) \ln(287/\sqrt{Z})} \quad (3)$$

where Z is the atomic number and A the atomic mass number. The definition of the radiation length given here, taken from [15], is a useful approximation and it is convenient for quick calculations. For a more accurate description see [13] and [15] and references therein. The presence of the radiation length in Eq. (2) is somehow incidental, used as a simplification even if it is not related to the physics of the scattering.

The approximation of Eq. (2) is generally good but for small x and large Z [22]. When a cosmic-ray muon crosses a compound or a series of layers of different materials, adding the individual σ_θ in quadrature results in a too small overall rms. In such cases it is much more accurate to find x and X_0 of the compound and apply Eq. (2). Having defined σ_θ , the angular distributions in space can thus be expressed as follows:

$$P(\theta_{space}) = \frac{1}{2\pi\sigma_\theta^2} \exp\left(-\frac{\theta_{space}^2}{2\sigma_\theta^2}\right) d\Omega \quad (4)$$

Correspondingly in the plane the distribution takes the form:

$$P(\theta_{plane}) = \frac{1}{\sqrt{2\pi}\sigma_\theta} \exp\left(-\frac{\theta_{plane}^2}{2\sigma_\theta^2}\right) d\theta_{plane} \quad (5)$$

where θ is the deflection angle. Assuming that the x and y axes are perpendicular to the direction of the incoming muon and $d\Omega \simeq d\theta_{plane,x} d\theta_{plane,y}$, then $\theta_{space}^2 \simeq (\theta_{plane,x}^2 + \theta_{plane,y}^2)$. The deflection angles in the two orthogonal planes are independent and identically distributed.

2.3. Simulation tools

When developing a particular technique or application based on cosmic rays it is very important to design the detectors and the overall application itself relying on a simulation tool that could generate the cosmic ray muons and track them when passing through the apparatus setup. In many cases the tracking is provided by a simulation tool called GEANT [23], while the muon generator algorithm is generally *hand-made*. Clearly the simulation of cosmic-ray muons is quite widespread in nuclear and particle physics. Most of the collaborations have their own generator tool based on particular experimental data, on some assumptions and approximations and on a specific generation algorithm. Nevertheless there are some packages that have been made publicly available and/or described in literature. A bunch of them are actually simulating the whole process from the first interaction of the primary cosmic ray with the nuclei of the atmosphere, while others rely on parameterisations of experimental data at different altitudes. A list of such tools, without the pretension to be comprehensive, is the following: Sybill [24], CRY [25], FLUKA cosmic ray generator [26], MUPAGE [27], CMSCGEN [28]. Clearly a good muon generator for civil applications should simulate as accurately as possible the momentum, the direction of arrival and the charge ratio of the muons over the area of interest, namely the detectors used to measure the passage of the cosmic ray muons. Since a perfect simulator is not possible, due to incompleteness and uncertainties on the experimental data, to the approximation in parameterising the data and to the limitation in computing time, some compromises have to be made. Given the specific nature of civil applications such compromises are generally different from the ones of nuclear and particle experiments and also vary from application to application.

3. Detectors

Since decades, many types of muon detectors and, in general, of charged particle detectors have been developed, designed and realised for particle physics experiments. They are all ensuring high reliability and excellent performance with differences depending on the specific technology.

Concerning cosmic muon applications, specific requirements are needed according to the kind of application. Detectors used in muon radiography by absorption must usually operate in difficult environmental conditions. Stability with respect to environmental variations and low power consumption are necessary. In order to reach the site of installation the detector must be easily transportable and installable. Dedicated front end electronics and data acquisition are usually needed in order to fulfil these requirements. The detectors for MCS tomography have typically larger sensitive areas, $O(10) \text{ m}^2$ compared to $O(1) \text{ m}^2$ of the absorption case. While for the absorption methodology just one tracking detector can be used, in MCS two trackers must be used to measure simultaneously the muon upstream and downstream with respect to the object under investigation. A comprehensive, though not exhaustive, list of detectors for cosmic-ray muon applications is contained in Refs. [29–46].

Technologies in use are basically of three types, nuclear emulsion detectors, scintillation detectors and gaseous detectors. Recently a fourth technology based on Ring Image Cherenkov detectors has been proposed [47]. In the following sections some more details are given.

3.1. Detectors for muon radiography

As discussed above, the detectors for muon-based absorption radiography must ensure good tracking performance; provide good angular resolution ($\Delta\theta < O(10) \text{ mrad}$); produce bi-dimensional measurements and guarantee stability in time and position. Furthermore, since the corresponding applications could require to install the apparatus in difficult environmental conditions, robustness against weather variations and low power consumption are also necessary.

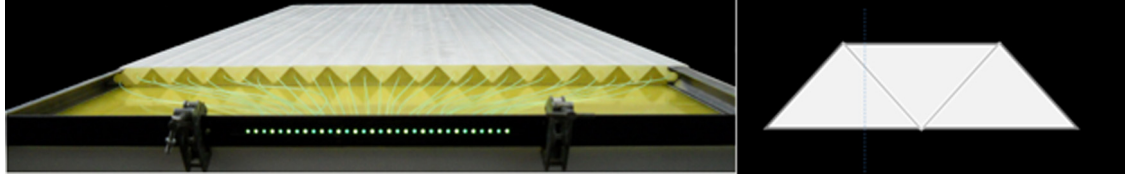


Fig. 7. Example of scintillator detector based on triangular bars. Left: a module of the MURAVES detector made of 32 scintillating bars with WLS fibres. Right: schematic view of the *centre of mass* principle for the position reconstruction of the muon. The relative amount of energy released by the muon in two adjacent bars depends on the distance between the centres of the two bars, while the sum is constant.

3.1.1. Nuclear emulsion detectors

Several requirements are fulfilled by nuclear emulsions. Nuclear emulsion detectors were among the first tracking devices to be used [48]. They are similar to photographic emulsions but they reveal the passage of charged particles. After the chemical development the track of the ionising particle is visible as a path of Ag grains. All tracks are registered together and no time information is available. Nuclear emulsions have been replaced over the years by electronic devices because of the large effort needed to visually scan the images and retrieve the track information. The development of emulsion analysis by automated microscope for the OPERA experiment [49] gives the possibility for applications in muon radiography by absorption. An interesting use of the nuclear emulsions is in the Emulsion Cloud Chamber (ECC) which consists of several layers of nuclear emulsion interleaved with lead or other high density absorber. In this way low momentum background muons can be rejected [50].

Nuclear emulsions have many advantages. They do not require electric power, are very compact and easy to transport and install. Their spatial resolution is $O(10) \mu\text{m}$ and allows to obtain $O(1)$ mrad angular resolutions with ECC of ~ 1 cm of thickness. As a drawback, this technology requires dedicated post exposure processing and read out by sophisticated and dedicated scanning systems. In addition, no time information is available and hence this detector can be used only for static situations. Recently progresses on the automatic scanning system have been reported [51].

3.1.2. Scintillation detectors

The detector technology used in a large variety of absorption applications is based on scintillator hodoscopes. A typical scintillator telescope consists of two or more double layers of orthogonal plastic bars used to track particles in two independent projections [52–57]. The bars can be easily shaped with different size. The typical length is of the order of 1 m for muon absorption small detectors. Longer bars, up to 6 m, can be produced by extrusion [58,59]. Arc shaped bars have been proposed for cylindrical bore hole detectors [60]. The position resolution is determined by the shape and the lateral size of bars. With a rectangular shape, particles produce mainly a single hit per plane and hence the spatial resolution σ is directly related to the bar lateral size L , in particular $\sigma = L/\sqrt{12}$.

The scintillation light signal propagates to the bar end faces directly (this requires highly transparent scintillators) or it is transported by secondary light emission in wavelength shifting optical fibres. The light signal is read by photodetectors optically coupled to the bar lateral edges. Commonly used photodetectors are photo-multiplier tubes (single or multi anodes) and more recently silicon photomultipliers (SiPM). The latter are cost effective, efficient, robust, have low power consumption and, due to their small dimension $O(1) \text{ mm}^2$, are ideal for compact assembly. SiPM are more sensitive to temperature variation with respect to phototubes.

A triangular shape, as shown in Fig. 7, measuring the signal fraction released in adjacent bars can be used to improve the spatial resolution ($\sim 3 \text{ mm}$ for $L = 33 \text{ mm}$) [54,55]. When better spatial resolution is required and/or detectors must be compact, scintillator fibres can be used. For example scintillating fibres with a helical winding were used for a small diameter cylindrical bore-hole detector [61,62]. Other example of scintillating bars based bore-hole detectors are reported in [63–66] for the monitoring of a subsurface reservoir.

3.1.3. Gaseous detectors

Gaseous detectors are less common in muon radiography by absorption because they are more difficult to operate and control in field experiments with respect to scintillation detectors. In the Tomuvol project [67,68] Glass Resistive Plate Chambers have been used, while multi wire proportional chambers are in use at the Sakurajima laboratory in Japan [69]. A relatively new technology, based on micro-pattern gaseous detectors (Micromegas) has also been used to realise telescopes for muon tomography applications [70]. These detectors can reach a $O(1) \text{ m}^2$ active surface and can be equipped with $O(1000)$ strips in both orthogonal coordinates. A position resolution of $\sim 300 \mu\text{m}$ can be obtained. Therefore, either an angular resolution similar to the one of scintillator telescopes can be obtained with a compact detector, or a much higher resolution ($\sim 1 \text{ mrad}$) can be obtained with a telescope having layers spaced by about 1 m.

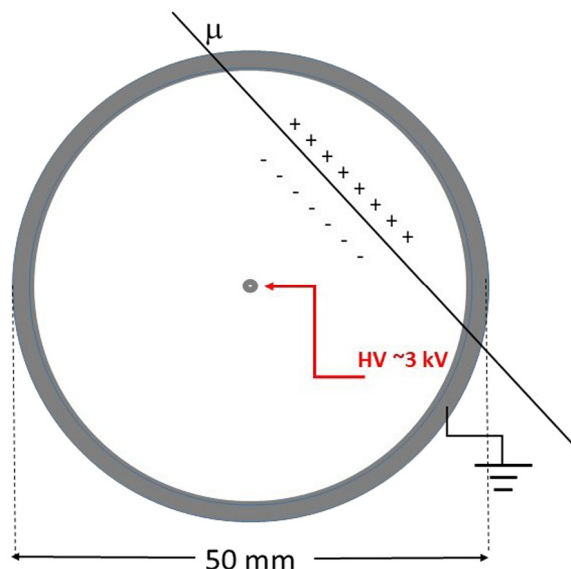


Fig. 8. Cross section of a drift tube with the passage of an ionising particle.

3.2. Detectors for muon tomography

MCS tomography requires at least two detectors, one measuring muons at the entrance of the volume to inspect, the other at the exit. They must fulfil the same requirements in terms of efficiency and resolution described above, but in addition they should also cover large areas (detectors must be cost effective). An additional useful requirement, although difficult to obtain, would be the detector capability to provide information about the individual muon momentum.

Telescopes made with one of the technologies (scintillators or Micromegas) used for absorption analysis could be implemented also for MCS tomography. However, given the dimensions of the objects to inspect (e.g. transport containers, dry storage casks for nuclear spent fuel) that can exceed a dozen of square meters, the number of channels required could be not affordable at a reasonable cost. Large muon detectors can be realised, as in particle physics experiments, using gaseous detectors as drift chambers or resistive plate chambers (RPC).

3.2.1. Gaseous detectors

Drift chambers can have different cell structure but the simplest shape to ensure construction simplicity, robustness and good performance is a ~ 5 cm diameter metallic tube with a coaxial anodic wire (Fig. 8). When a charged particle crosses the cell, it ionises the gas atoms along its path. If the central conductive wire is electrically connected to a sufficient positive high voltage, and the external tube is ground connected, the presence of an electric field obliges the ions to move towards the cathode and the electrons to drift towards the anode. In the proximity of the wire, with a typical diameter of $20 \div 100 \mu\text{m}$, the electric field is high enough to allow drifting electrons to accelerate and to ionise in turn the gas atoms. An avalanche process then starts, with a charge multiplication that induces on the wire an electric signal high enough to be read-out by front end electronics. The electron drift velocity is much lower than the velocity one would expect in vacuum, since it is determined by collision of electrons with the gas atoms. Therefore, it depends on the gas type and on the electric field. It is important to avoid electronegative gases (as oxygen in the air). A typical gas used in drift detectors is argon with the addition of molecular gases (quencher e.g. isobutane, CO_2) to limit the discharge along the wire. Despite the quite large cell size, a good space resolution ($\sim 300 \mu\text{m}$) is obtained thanks to the measurement of the drift time of electrons. A typical detector module can be constructed by several layers of tubes. Layers oriented in the orthogonal direction ensure measurement of both coordinates and provide tracking in two orthogonal planes. On the other hand, RPC's are fast devices which can measure, with good precision, the time of flight required for the muon to travel between the two detector modules. Therefore, in principle they could provide momentum measurement at least for the low energy part of the muon spectrum [71].

It could be convenient to realise hybrid detectors having both drift chambers and RPC to profit of the advantages of both techniques.

Also gas electron multipliers (GEM) have been proposed for cosmic muons measurement [72].

3.2.2. Momentum measurement.

It would be highly recommended, to improve the performance of MCS tomography, to include momentum measurement in the detector system. However it is not easy to add a devoted spectrometer without increasing enormously the

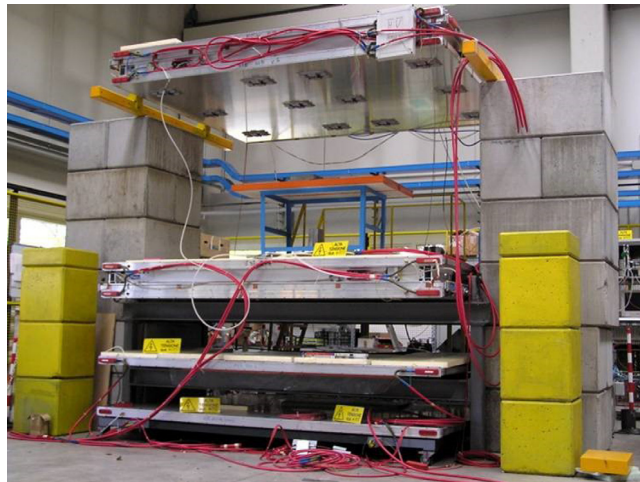


Fig. 9. Picture of the INFN muon tomography system. The two chambers enclosing the test volume are located in the upper part. In the lower parts the additional detectors for particle momentum analysis are visible.

costs or adding unacceptable complexity to the system. In addition to time of flight measurements discussed above, solutions could be obtained by adding a measurement of scattering inside the detector itself [73–75] or in additional layers of known materials [76].

3.2.3. An example of a detector for MCS tomography

A system to study muon tomography has been operating for more than ten years at the INFN national laboratory of Legnaro, near Padova [77,78]. It has been the first muon tomography system of large dimensions, realised using two spare detectors from the set of muon chambers produced for the CMS experiment [79]. As shown in Fig. 9, two chambers are placed parallel to the horizontal plane with a vertical gap of ~ 160 cm. The detectors have $300\text{ cm} \times 250\text{ cm}$ lateral dimensions and are both realised with twelve layers of rectangular drift cells in groups of four (quadruplets). To guarantee measurement of both coordinates, one quadruplet is oriented in the orthogonal direction compared to the other two. The two detectors enclose a total volume of more than 11 m^3 and the system includes, in the lower position, two more quadruplets and two 11 cm thick iron plates to provide momentum information in a similar way as in Ref. [76].

An example of the system reconstruction capability is shown in Fig. 10 where a small car (FIAT 500) is inserted in the system and the structure of its front part is reconstructed.

4. Muon radiography

4.1. Introduction

As already described in Section 2 muon radiography by absorption is based on the measurement of the attenuation of the muon flux intensity by a *large* massive object. The flux measurement is done downstream of the object to be investigated, i.e. after that the muons have crossed it. This implies the possible use of just one detector without a second detector that measures, upstream, the incoming muon, as in the case of the muon tomography based on multiple scattering. Of course more detectors can be used to enlarge the total detection area, but all are positioned downstream with respect to the object to be investigated (see Fig. 11).

The calculation of the attenuation of the flux of muons is done using dedicated measurement campaign of *free sky* muons, i.e. measuring the muon flux when no object is interposed between the detector and the sky, and/or by models and experimental measurements of the expected flux of the incoming muon. One key issue for the interpretation of the data is the knowledge of the differential muon energy spectra and of the interaction of the muons in matter as discussed in Section 2.

This technique has been applied to investigate large volume objects as volcanoes, hills, mineral deposits or pyramids. In most of these cases the multiple scattering measurement technique cannot be used, because the two detectors measuring the same muon upstream and downstream reduce drastically the solid angle seen from the detector system, and the scattering angle would be too big.

Usually the size of the detector ($\sim 1\text{ m}^3$) can be considered negligible with respect to the size and distance of the structure under investigation. In this case the detector can be considered point-like and muons with the same direction as coming from the same zone of interest independently from the actual position they hit the detector. When this is not

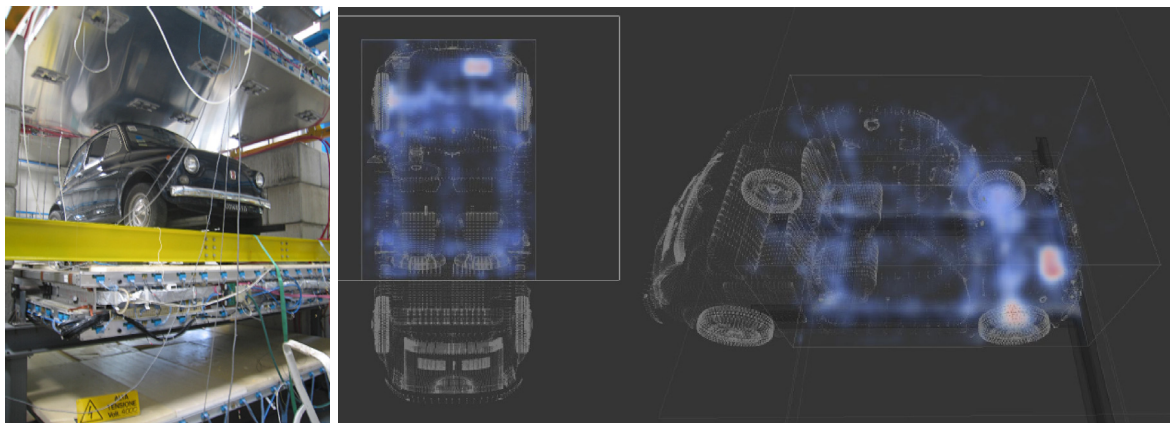


Fig. 10. Left: picture of a 1967 FIAT 500 inside the INFN muon tomography system. Right: reconstruction of the front part of the car superposed to the car layout. The battery is clearly visible.

Source: Picture and images are taken from [80].

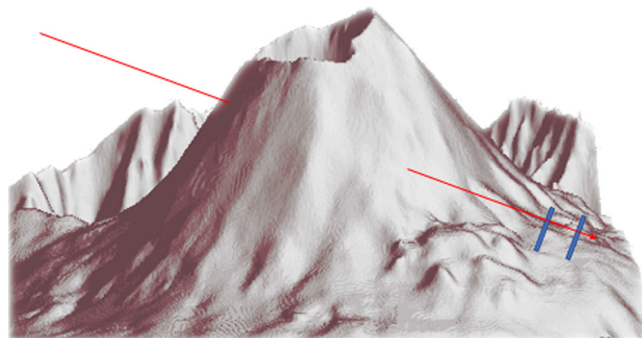


Fig. 11. Pictorial representation of a muon radiography by absorption. A detector is placed on the flank of a volcano and measures the number of muons that cross the rock. Detector size is not to scale.

the case, and the distance and size of the object are small, it is possible to deduce some information about the distance and linear dimensions of the object under study (see Section 4.2.6).

Muography provides, typically, a single bi-dimensional (2D) projective measurement from a certain position. Combining different measurements from different locations, it is possible to get three-dimensional (3D) informations about the internal structure of the object or about the position and dimension of a void. Sometime this kind of measurement is referred to as *muon tomography*, not to be confused with the above mentioned muon MCS tomography.

In the last years many advances have been reported in the development of algorithms devoted to the 3D-reconstructions from muon data or in joint with gravimetric data (see Section 4.2.6).

Recently progresses have been reported in the attempt to provide *real time* information about volcanoes activity, by measuring, for example, the magma dynamics in an erupting volcano (see Section 4.3). This is very encouraging for possible applications of this technique to the monitoring of volcano activity for mitigation of the volcanic risk.

The main advantages of muography, with respect to traditional geophysical prospecting techniques, are: the spatial resolution (that can reach few meters), the range (~ 1 km of crossed rock) and the volume of investigation (the field of view has a conical shape with semi-aperture angle in the range $40^\circ \div 60^\circ$). Moreover the *inverse problem* is well defined and does not suffer of non uniqueness of the solution. The source (cosmic muons) is for free and available everywhere and always. Once installed the detector can operate without human presence and from a certain distance from the object of investigation (order 1 km in the case of volcanoes, this can be relevant in case of emergency during eruptions) and can provide real-time information, in the case of electronic detectors. Power consumption is low (tens of W/m² for the electronic devices) or absent for nuclear emulsions.

The main limitations of the muography, on the other hand, are the muon flux, that is “low” and consequently the measurement of thick structures can require large detection area and/or long acquisition time and the fact that only the volumes on a higher level than the detector can be studied. In the following, typologies of applications in geology, mineral exploration, archeology/civil engineering and industry are discussed.

In *geological muography*, or in short *geomuography*, the study concerns geological cases as the measurement of the size of a volcano conduit or the mass distribution inside a cone of a volcano (see Section 4.3), mine inspection, glacier

monitoring and hydrogeological measurements (see Section 4.4). In a second case the study concerns sharp discontinuities of small size, as cavities/tunnels in the underground or inside a building and can be applied to archeology and civil engineering, as illustrated in Section 4.5. A third class concerns applications in the industrial field (see Section 4.6).

4.2. Basic principles

Muography is based on the measurement of the attenuation of the muon flux. Due to their interaction with the matter muons lose their energy proportionally to the length and to the mass density of the crossed rock. As described in Section 2, high energy muons can be assumed to cross the matter almost in a straight line. Considering a stretch of rock of length L with mass density ρ , the opacity X is defined as:

$$X(L) = \int_L \rho(x) dx \quad (6)$$

If the density is constant along L the equation becomes:

$$X(L) = L\rho \quad (7)$$

while, if this is not the case, the opacity can be written in terms of the average density $\bar{\rho}$:

$$\bar{\rho} = \frac{1}{L} \int_L \rho(x) dx \quad (8)$$

$$X(L) = L\bar{\rho} \quad (9)$$

For a certain value of opacity X only muons with an energy greater than a minimum input value E_{min} will emerge from the rock and will be measured. Since the cosmic muons have a continuous energy spectrum the number of muons measured after the rock is correlated to the opacity X and can be therefore evaluated. From the opacity the average density $\bar{\rho}$ can be obtained, if the length L of crossed rock is known. Conversely, the length of crossed rock can be measured if the density is known.

As described in Section 2.2 the energy loss suffered by the muon in matter is well described by Eq. (1). The expression can be rewritten making explicit the dependence on the energy E :

$$\left\langle -\frac{dE}{dX} \right\rangle = a(E) + b(E)E \quad (10)$$

In general the parameters a and b depend on the muon energy and on the atomic composition of rock through the average of the ratio Z/A and Z^2/A , where Z is the atomic number and A the mass number of the elements composing the rock [17].

For the typical composition of the rock, when no heavy elements are present, $Z/A \sim 1/2$ and the a and b coefficients can be considered constant with $a \sim 2 \text{ MeV g}^{-1} \text{ cm}^2$ and $b \sim 4 \times 10^{-6} \text{ g}^{-1} \text{ cm}^2$.

Often an ideal rock, called standard rock, is introduced with the following values: $Z/A = 0.5$, $Z^2/A = 5.5$, $Z = 11$, and $\rho = 2.65 \text{ g/cm}^3$. In many cases the use of the standard rock gives reasonable results, but, as reported in a recent study on the effect of the rock composition [81], it can introduce a bias in the muon flux calculation particularly when the target consists of high Z^2/A rocks (like basalts and limestones) and if the rock thickness exceeds 300 m. As an example, in the case where the target is 600 m thick and made of limestone ($\rho = 2.711 \text{ g/cm}^3$) the standard rock assumption underestimates the flux by $7 \div 8\%$.

If a and b are considered constant, by integrating Eq. (10) it is possible to calculate an analytic expression of the exit energy E^e of a muon with an initial energy E^0 after the muon crossed a rock thickness of opacity X [17,82]:

$$E^e = (E^0 + \frac{a}{b})e^{-bX} - \frac{a}{b} \quad (11)$$

Better estimations of this value can be obtained by considering energy dependent coefficients in the equation and by considering rock composition close to the real one (see [17,83]). In [84] the energy loss of muons in the standard rock obtained by energy dependent coefficients a and b are fitted with a fourth order polynomial function providing an analytic curve with relative errors never exceeding 2%. More detailed results can be obtained with Monte Carlo simulation programs as GEANT4, that take in account all known physical processes involved. From Eq. (11) it is possible to evaluate the minimum energy $E^0 = E^{min}$ that a muon needs to cross a certain amount of opacity X . Setting the exit energy E^e to zero:

$$E^{min}(X) = \frac{a}{b}(e^{bX} - 1) \quad (12)$$

In Fig. 12 the minimum energy as a function of the standard rock thickness is shown.

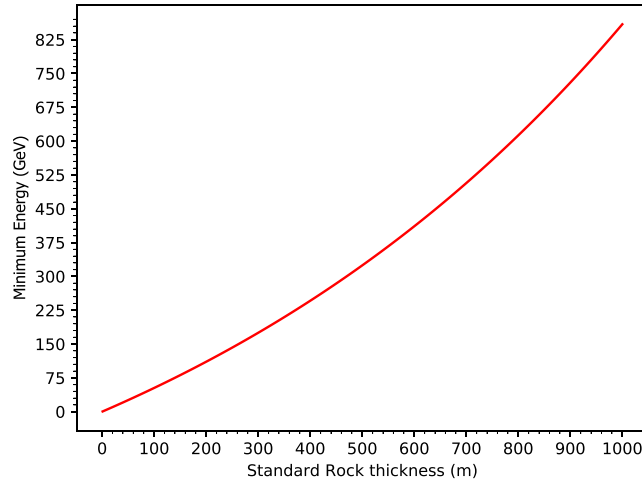


Fig. 12. Minimum energy required for a muon to cross a certain amount of standard rock, evaluated from Eq. (12).

Table 1

Parameters from [87] used in Eq. (13).

P ₁	P ₂	P ₃	P ₄	P ₅
0.102573	−0.06828	0.958633	0.0407253	0.817285

4.2.1. The muon spectrum

Knowledge of the muon energy spectrum is a key element for data analysis and feasibility studies. Many data are available in the literature and many models can describe with a certain amount of precision the number of expected muons as a function of the energy and of the zenith angle. A review can be found in [85]. Basically two approaches are possible. A first class consists in full Monte Carlo simulations where air showers are produced starting from primary cosmic radiation, and muon interactions within the atmosphere are evaluated taking in account also geomagnetic and altitude dependence. A common software is, for example, *CORSICA* [86]. The second class is based on parametric curves fitted with the experimental values and provides analytic expressions of the muon spectrum. As an example in Fig. 13 the differential flux as a function of the muon energy is reported for different zenith angles. It has been obtained using Eq. (13), that is a modified parametrisation of Gaisser's formula [87] to correct for the curvature of the Earth and muon decay.

$$\frac{dI_{\mu}}{dE_{\mu}} = 0.14 \left[\frac{E_{\mu}}{\text{GeV}} \left(1 + \frac{3.64 \text{ GeV}}{E_{\mu} (\cos \theta^*)^{1.29}} \right) \right]^{-2.7} \times \left[\frac{1}{1 + \frac{1.1 E_{\mu} \cos \theta^*}{115 \text{ GeV}}} + \frac{0.054}{1 + \frac{1.1 E_{\mu} \cos \theta^*}{859 \text{ GeV}}} \right] \quad (13)$$

where:

$$\cos \theta^* = \sqrt{\frac{(\cos \theta)^2 + P_1^2 + P_2 (\cos \theta)^{P_3} + P_4 (\cos \theta)^{P_5}}{1 + P_1^2 + P_2 + P_4}} \quad (14)$$

P₁, P₂, P₃, P₄, and P₅ are parameters given in Table 1. Other models and experimental data are presented in [88].

4.2.2. Density distribution measurement

In the context of muon radiography the direct problem can be defined as the following: given a certain detector, estimate the number $N(\theta, \phi; X)$ of muons measured in the time interval ΔT as a function of the opacity $X(\theta, \phi)$ and direction (θ, ϕ) , (where θ and ϕ are the zenith and azimuthal angle). Formally $N(\theta, \phi; X)$ can be written as:

$$N(\theta, \phi; X) = \Delta T \times S_{\text{eff}}(\theta, \phi) \times I(\theta, X) \quad (15)$$

where

$$I(\theta, X) = \int_{E^{\min}(X)}^{\infty} \Phi(\theta, E) dE \quad (16)$$

is the integrated flux.

$\Phi(\theta, E)$ gives the differential flux, ΔT is the effective data acquisition time while S_{eff} is called *effective surface* and takes in account the sensitive area S , the geometrical acceptance $A(\theta, \phi)$ and the efficiency of the detector and of the selection

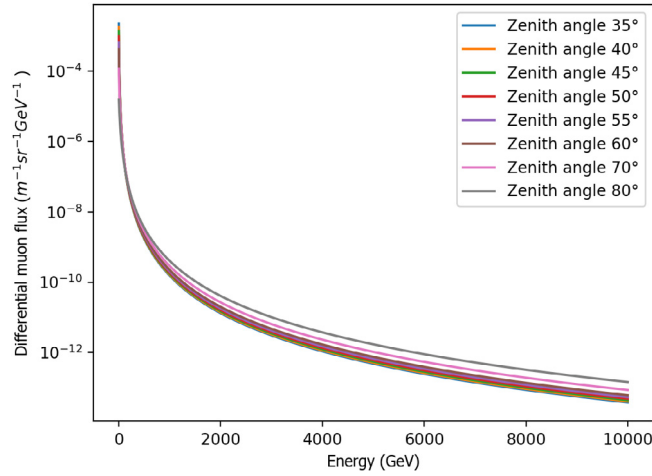


Fig. 13. The differential flux of muons evaluated with Eq. (13).

algorithm ϵ :

$$S_{eff} = S \epsilon A(\theta, \phi) \quad (17)$$

The *inverse problem* consists in the evaluation of the opacity $X(\theta, \phi)$ from the measured number of muons $N(\theta, \phi; X)$. The problem is well posed in the sense that the answer is unique. Once $X(\theta, \phi)$ is known the average density $\bar{\rho}(\theta, \phi)$ can be calculated from the knowledge of the length of rock $L(\theta, \phi)$ that the muon crossed along the direction (θ, ϕ) . The value of L is typically computed from Digital Elevation Models (DEM) of the investigated area. The function $\bar{\rho}(\theta, \phi)$ is the bi-dimensional muographic density image of the investigated object obtained from a certain position and represents a projection of the mass distribution inside the object. Three-dimensional images can be obtained by performing measurements from different positions and/or integrating gravimetry data with muographic data, as is discussed in Section 4.2.6.

4.2.3. Relative transmission for the detection of cavities

In the detection of cavities an alternative approach can be followed [89–91]. The transmission $T(\theta, \phi)$ is defined as the fraction of muons that have been able to cross the object. The expected transmission T_E can be evaluated using an average density of the object and in the hypothesis of absence of voids:

$$T_E(\theta, \phi) = \frac{\int_{E^{min}(X)}^{\infty} \Phi(\theta, E) dE}{\int_{E_0}^{\infty} \Phi(\theta, E) dE} \quad (18)$$

where $E^{min}(X)$ is the minimum energy required for a muon to cross the amount of rock of opacity X and E_0 is the minimum energy for a muon to be detected by the telescope, typically of the order of 100 MeV, much less than $E^{min}(X)$.

The measured transmission can be evaluated from the number of muons measured in presence of the object $N_u(\theta, \phi; X)$ and a sample N_{fs} that can be measured acquiring free sky muons, i.e. without the presence of any object between the detector and the sky. From Eqs. (15) and (16) it follows that:

$$N_u(\theta, \phi; X) = \Delta T_u \times S_{eff}(\theta, \phi) \times \int_{E^{min}(X)}^{\infty} \Phi(\theta, E) dE \quad (19)$$

$$N_{fs}(\theta, \phi) = \Delta T_{fs} \times S_{eff}(\theta, \phi) \times \int_{E_0}^{\infty} \Phi(\theta, E) dE \quad (20)$$

where ΔT_u and ΔT_{fs} are the acquisition time of the two measurement campaign. If we assume that the effective surface is the same, from the ratio of the two previous equations we obtain:

$$\frac{N_u(\theta, \phi; X)}{N_{fs}(\theta, \phi)} = \frac{\Delta T_u \int_{E^{min}(X)}^{\infty} \Phi(\theta, E) dE}{\Delta T_{fs} \int_{E_0}^{\infty} \Phi(\theta, E) dE} \quad (21)$$

Defining the measured transmission $T_M(\theta, \phi)$ as

$$T_M(\theta, \phi) = \frac{\Delta T_{fs} N_u(\theta, \phi)}{\Delta T_u N_{fs}(\theta, \phi)} \quad (22)$$

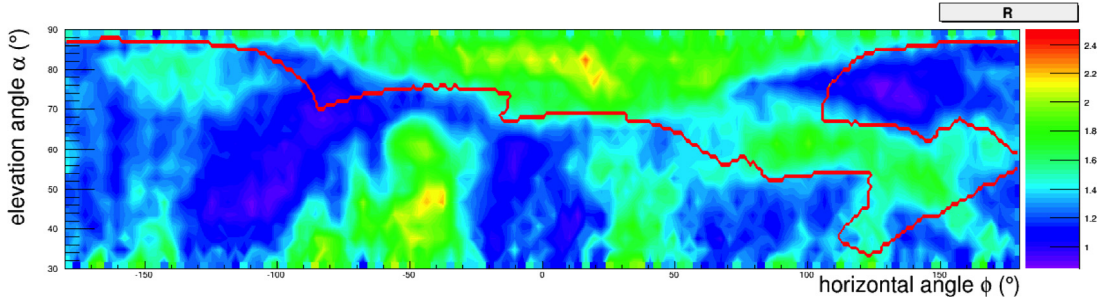


Fig. 14. Example of relative transmission measured in [89–91]. R values greater than 1 (green regions) indicate directions where cavities are supposed to be encountered. The red line represents the expected signal shape of a known test chamber. Other green regions correspond to other cavities in the detector acceptance.

and if no void is encountered Eq. (21) can be written as:

$$T_M(\theta, \phi) = T_E(\theta, \phi) \quad (23)$$

The relative transmission $R(\theta, \phi)$ is defined as:

$$R(\theta, \phi) = \frac{T_M(\theta, \phi)}{T_E(\theta, \phi)} \quad (24)$$

If muons that cross the object along the direction (θ, ϕ) do not cross any void (or other density anomalies) the relative transmission is expected to be close to 1:

$$R(\theta, \phi) \sim 1 \quad \text{for each direction where no void is encountered.} \quad (25)$$

Conversely if a cavity is encountered along a direction (θ, ϕ) the number of measured muons is greater than the expected one, the measured transmission is therefore greater than the expected one and the relative transmission is greater than 1:

$$R(\theta, \phi) > 1 \quad \text{for each direction where a void is encountered.} \quad (26)$$

In Fig. 14 an example from [89] of the relative transmission R is shown.

4.2.4. Feasibility studies

The estimation of the number of muons detected by a telescope, expressed in Eq. (15), can be used for feasibility studies. The main parameters involved are the opacity X , the effective surface $S_{eff}(\theta, \phi)$, that is directly connected to the sensitive area of the detectors, and the acquisition time ΔT . The number of detected muons, for a given opacity, is directly proportional to the product $S_{eff}(\theta, \phi) \times \Delta T$, therefore the same number of muons can be collected in a certain time integral ΔT by increasing the effective surface (i.e. the sensitive area of the detectors and/or increasing the number of detectors) or, for a certain effective surface, increasing the acquisition time.

Following the discussion reported in [84] it is possible to define the detection surface and acquisition time needed to resolve, from the point of view of the statistical uncertainty, a difference in the opacity. Conversely, for a given sample it is possible to establish the corresponding density resolution.

For two opacities X_0 and $X_0 + \delta X$ the expected difference $\Delta N(X_0, \delta X)$ is:

$$\Delta N(X_0, \delta X) = N(X_0 + \delta X) - N(X_0) = \Delta T \times S_{eff}(\theta, \phi) \times \Delta I \quad (27)$$

where $\Delta I = I(\theta, X + \delta X) - I(\theta, X)$ is the variation of the integrated flux for a variation δX of opacity.

Let us assume that N muons are detected and that N is large enough so that the Poissonian distribution may be reasonably approximated by a Gaussian distribution with mean N and standard deviation \sqrt{N} . The opacity X can be resolved with an error δX at a confidence level of 68% if:

$$\Delta N(X_0, \delta X) > \sigma = \sqrt{N(X_0)} \quad (68\% \text{ confidence level}) \quad (28)$$

From Eqs. (16) and (27) the following inequality can be set:

$$\Delta T \times S_{eff} \times \frac{\Delta I^2(X_0, \delta X)}{I(X_0)} > 1 \quad (29)$$

The previous discussion is valid only if the contribution of the background in the number of muons detected is negligible. If this is not the case, a better estimation of the sensitivity can be obtained from the signal to background

ratio $N/\sqrt{N_B}$, where N_B is the number of background events in the sample. If the flux of background Φ_B is known, the signal to noise ratio can be described by:

$$\frac{\Delta T \times S_{\text{eff}} \times I}{\sqrt{\Delta T \times S_{\text{eff}} \times \Phi_B}} = \sqrt{\Delta T \times S_{\text{eff}}} \frac{I}{\sqrt{\Phi_B}} \quad (30)$$

An example of comparison of sensitivity between two different experiments in presence of background is reported in [82].

4.2.5. Angular aperture, resolutions and geometrical acceptance of a typical detector

A typical detector consists of two or more sensitive planes of size L with a distance D between the first and the last plane. Each plane can measure the position of the impact point of the muon with a resolution d . The detector is at a distance R from the object to be investigated, called in the following the target. The angular resolution of the detector is of the order $\Delta\theta \sim d/D$ while the maximum angle that can be observed is of the order $\text{tg}(\theta_{\text{max}}) \sim L/D$. Increasing the distance between the planes therefore improves the angular resolution but decreases the angular aperture. The spatial resolution achievable on the target is of order $\Delta x \sim \frac{d}{D}R$. These simple considerations allow to have a quick estimation of the main geometrical parameters involved in a muography. As an example, if the spatial resolution is $d = 5$ mm and the detector has a size $L = 1$ m and a distance $D = 1$ m, the maximum angle observable is $\theta_{\text{max}} = 45^\circ$, the angular resolution is $\Delta\theta \sim 5$ mrad. A target at a distance $R = 1000$ m can be resolved with a spatial resolution of ~ 5 m. At the maximum angle it corresponds to the minimal effective surface since only tracks at the edges of the detector can have the maximum angle. Conversely, the direction orthogonal to the planes has an effective surface corresponding to the sensitive area of a plane. Numerically this is described by the geometrical acceptance or geometrical factor. For a simple geometry, as the one described, it can be calculated analytically. For more complex geometry numerical computation can be used.

In the case of the investigation of large objects with size of order of a few hundred meter or more the effect of the multiple scattering of muons within the object must be considered. Since the effect of multiple scattering is inversely proportional to the muon energy, while the range is directly proportional, the dispersion of the muons at the exit of the object is not very sensitive to the opacity of the object and is of order 10 mrad [69]. This means that in principal it is not necessary to have detectors with spatial resolution much better than this value. However, better resolution can be used to estimate the momentum of low energy muons (\leq few GeV) by measuring their multiple scattering in iron/lead plates inserted between the detector planes. In this way the signal to background ratio can be improved [92].

4.2.6. 3D imaging

As already mentioned in the previous sections muography can provide 2D distributions of the average opacity or of the relative transmission. A single measurement can give the mass density angular distribution, or detect the presence of a void region, with an indication of its direction and angular dimension, neither the exact position in space nor its size. A remarkable exception, that can be applied in some particular cases with sharp discontinuity as for cavities, is the *back-projection method*, that is described at the end of this section.

In the last years many advances in the study and application of algorithms for the reconstruction of 3D information have been developed. They consist in combining only muographic data from different locations, or joint muographic data with other geophysical data, such as gravimetry, electromagnetic, seismic etc. In the following a short review of the main principal methods will be reported.

A standard procedure for the determination of the 3D density distribution consists in dividing the region of interest in voxels, i.e. basic volumetric units, which size depends strongly on the spatial resolution and on the amount of available data. If the density function ρ^j is known for each voxel j the opacity X^i seen from each telescope direction i is given by

$$X^i = \sum_j^M L^{ij} \rho^j \quad (31)$$

where L^{ij} is the matrix of the length crossed by the telescope angles views i in each voxel j . The direct problem is, as for the 2D case, the determination of the expected flux measured by each detector in the i th direction. This is equivalent to know the mean opacity X^i for each direction, since mean opacity and flux are unambiguously correlated. The direct problem does not have ambiguity, and from the density function ρ^j the opacity X^i can be calculated. The inverse problem consists in evaluating the density vector ρ^j that reproduces the measured opacity vector (i.e. the measured flux) for each direction i of all the detectors.

In other terms, an inverse problem is solved by minimising an objective function related to the proximity of model-based reconstructed data to the real observed data (for a general introduction to inverse problem see [93]).

Differently from the 2D inversion problem, typically, the number of measurements is not sufficient to have a unique solution. The problem so suffers of ambiguities that need further assumptions to be resolved.

One of the first applications of this method was performed by Tanaka et al. [94] by installing two muon detectors around Mount Asama, on the Japanese island of Hunshu [95]. Assuming the density changes smoothly within the detector resolution they produced a 3D representation of a low density crater area found in 2006. These results were encouraging

concerning the development of inversion techniques for three dimensional imaging, but still had limitations due to some a priori assumptions needed before solving the inversion problem.

As already mentioned, muography is capable of finding low-density or vacuum regions underground. In this scenario it is also possible to obtain a 3D reconstruction of cavities by solving inverse problems. An example is explained in [96] by Lesparre et al. where a 3D density imaging of low density regions from underground galleries in the Tournemire experimental platform (France) has been attempted. Measurements were performed from three different sites with a partial overlap of muon trajectories, and an inverse problem has been posed to interpolate the different data to model a volumetric image of the density distribution. Once the voxels have been defined, the inversion problem is resolved using a simulated annealing which is a two-loop iterative nonlinear method. The iteration stops according to the minimisation of an objective function. The inverse problem is first solved in 2D since structural geometries extend roughly in a direction parallel to the N-S axis, then the data were analysed with a nonlinear 3D inversion process to check the validity of a medium homogeneity along the N-S axis. The resulting density image shows a very low density zone in the region just above one of the sites of measurements. A N-S corridor of low density is still observed with values varying between 0 and 1.5 g/cm³.

Muographic imaging of underground hidden objects is not restricted to cavities, more frequent in the field of archaeology. Indeed, in the field of ore detection the interest is typically focused on high-density regions that can be detected and geometrically reconstructed with two or more overlapping muographies (see Section 4.4.1). Examples of inversion problem applications on 3D reconstruction of very dense objects with a strong density contrast respect to the surrounding material are reported in [97–100].

4.2.7. Joint inversion of muographic and gravimetry data

The inverse problems that have been described so far solve a density distribution involving only muography data. It has been demonstrated that combining muographic images with gravimetric data, which are related to the density values as well, improves the results of the three dimensional density map reconstruction.

Gravimetry provides a traditional method to measure densities of large objects such as volcanoes, measuring the vertical component of the local gravity field; a number of gravity studies have been performed to infer subsurface density structures of volcanoes. However, these studies suffer from the well-known problem of non-uniqueness. Joint inversion methods are able to solve the question of how to use both muographic and gravimetric data to obtain a density map of the target.

Previous studies tried to solve the non-uniqueness of the solution of gravimetric data inversion introducing additional constraints given by seismic exploration data, but the spatial resolution of seismological/gravimetric imaging is limited to the wavelength of seismic waves (> 1 km). Muon radiography has a typical angular resolution of a few tens of milliradians, achieving a spatial resolution of tens of meters which is much better than that of conventional geo-exploration techniques. Muon radiography and gravimetry used alone present different drawbacks: while gravimetric data cannot provide a unique solution, muon radiography has no resolution beneath the detector. Several applications show that a hybrid measurement based on both gravity and muography is useful especially for *small* structures with sizes of a few hundreds of meters near the surface, and also for measuring density in the regions not covered by the muographic data. In this context, Davis K., Oldenberg D. W. et al. [101] have tested on simulated situations, an algorithm to invert muography and gravity data, to recover a 3D distribution of density contrast. Similar studies have been performed by Nyshiyama et al. [92] which applied a joint inversion method to the Howa-Shinzan lava dome, Hokkaido, Japan, after a solid validation on synthesised data. The mathematical approach is very similar in the studies of both Davis and Nishiyama.

Once the volume of interest is divided into a discrete number N of voxels, and assuming a starting value of the density function $\rho^j = \rho_0$, a gravimetric anomaly can be defined as:

$$\Delta g^i = \sum_j^n G^{ij} \rho^j \quad (32)$$

where G^{ij} can be written as:

$$G^{ij} = \int_{x_{\min}^j}^{x_{\max}^j} \int_{y_{\min}^j}^{y_{\max}^j} \int_{z_{\min}^j}^{z_{\max}^j} \frac{\varsigma(z^i - z)}{\sqrt{(x^i - x)^2 + (y^i - y)^2 + (z^i - z)^2}} dx dy dz \quad (33)$$

where $\varsigma = 6.674 \times 10^{-11}$ N m² kg⁻² is the universal gravitational constant. Muography provides the opacity:

$$X^i = \sum_j^M L^{ij} \rho^j \quad (34)$$

where L^{ij} is the length of the i th muon path crossing the j th voxel. Gravimetric and muographic data can be joined as:

$$\mathbf{d} = \begin{pmatrix} \mathbf{X} \\ \Delta \mathbf{g} \end{pmatrix} \quad (35)$$

Eqs. (32) and (34) can be simplified in:

$$\mathbf{d} = \mathbf{A}\rho \quad (36)$$

where $\mathbf{A} = \begin{pmatrix} 1 \\ l \end{pmatrix}$. Nishiyama et al. adopted a Bayesian approach to solve Eq. (36) for ρ including a priori information. They assumed that the true value of data \mathbf{d} can be described by a Gaussian probability density function with observation \mathbf{d}_{obs} and a covariance matrix \mathbf{C}_d . Moreover, a smoothing constraint has been imposed through an exponential covariance

$$C_\rho(i, j) = \sigma_\rho^2 \exp(-d(i, j)/l) \quad (37)$$

where σ_ρ is the a priori error of the density, l is the correlation length, and $d(i, j)$ is the distance between the i th and j th voxels.

Before having been applied to the Showa-Shizan lava dome data taken by Tanaka et al. [95], the inversion method has been tested on synthesised data expected for a known density model and the actual survey configuration. This test allowed to find the best a priori parameters verifying a minimal chi-square criterion. Once the a priori hypotheses have been fixed, data from Showa-Shizan lava dome have been inverted. Muographic results show the existence of a lava plug narrowing downward, characterised by a higher density than the surrounding deposits.

The joint inversion has been applied to resolve the three-dimensional, detailed shape of the plug, especially of the lower part, which might extend to the underground magma reservoir.

The work of Nishiyama et al. demonstrated that a combination of gravity and muon radiography data enables us to determine the 3D density structure of a geological target with a higher spatial resolution than using the conventional methods.

A more recent work, by Jourde et al. [102] develops a similar mathematical approach to the problem, applying it to examples taken from field experiments performed on La Soufrière of Guadeloupe, France. The mathematical engine used here is based on a resolving kernel, a function, defined in the whole space, that acts as spatial filter relating the true unknown density structure to the density distribution recoverable from data. Results on available data from La Soufrière of Guadeloupe show that the information provided by muon tomography is dominant relative to gravimetry, for points inside the volume of the lava dome spanned by the lines of sight of the telescopes. The situation strongly changes when a point below the lines of sight of the muon detector is moved. Indeed, muon data compensate the great sensitivity of gravimetry at near-surface locations by shifting the centre of mass of the resolving kernel downward. This improves the vertical resolution achievable in the deepest parts of the volcano. The method of resolving kernels allows also to include some prior information by defining a weighted scalar product in the space X of continuous L^2 functions going from \mathbb{R}^3 into \mathbb{R} , which contains the 3D density distribution ρ . The weight function in the scalar product may be used, for example, to neglect the impact of the free air zone around the studied structure for gravimetry and muography, or to introduce correlations for density variations. This study anticipated the estimation of the three-dimensional density structure of the La Soufrière de Guadeloupe lava dome discussed in [103]. Rosas-Carbajal et al. jointly inverted muon data from three simultaneous telescope acquisitions together with gravity data by minimising an objective function consisting of a weighted data misfit term and a model regularisation term:

$$\phi(\mathbf{m}) = (\mathbf{d} - \mathbf{G}\mathbf{m})^T \mathbf{C}_d^{-1} (\mathbf{d} - \mathbf{G}\mathbf{m}) + \epsilon^2 (\mathbf{m} - \mathbf{m}_{prior})^T \mathbf{C}_\rho^{-1} (\mathbf{m} - \mathbf{m}_{prior}) \quad (38)$$

where $\mathbf{m} = [\rho_\mu, \Delta\rho]$, \mathbf{m}_{prior} is the a priori density model, \mathbf{C}_d^{-1} is the data covariance matrix, \mathbf{C}_ρ^{-1} is the model regularisation matrix, and ϵ^2 the trade-off parameter, which establishes the relative weight of the regularisation in the cost function. Their approach performs a scaling of the regularisation matrix to counteract the natural decay of the sensitivity with depth for both gravity and muon data. Before inverting the real data, synthetic tests have been performed to assess the influence of the regularisation scaling and the resolution that can be expected. Without scaling, the inversion places the largest density contrasts close to the muon telescopes. In turn, the matrix scaling places the density contrasts where the true anomaly is located. Inversions without the gravity data confirm the importance of these data in the delimitation of the density anomalies in cases where the spatial coverage of the telescopes is not complete. Thus, the application of this method to La Soufrière de Guadeloupe data resulted in the first 3-D density model of a volcano lava dome from the joint inversion of simultaneous muon radiographies and gravity data. Several density anomalies have been detected, especially an extensive low-density zone located below the southern part of the summit where most of the increasingly active fumaroles are observed, reinforcing inferences from previous studies.

Several attempts to invert jointly muography and gravity data do not account for the fact that the two types of measurements respond differently to the same physical quantity. A possibility to solve this issue is to take into account an offset parameter between the density distributions inferred from the two different type of measurements. In [104] several solutions have been evaluated and applied to a synthetic volcano imaging scenario based on the Puy de Dôme volcano in the Central Massif region of France. In this work different methods to evaluate this offset have been considered, assuming that the offset can be approximated to first order as a constant for all measurements. They presented strategies assuming the same density model for both measurements types or by trying couplings between two different models. The relative density offset correction can be added in the objective function of Eq. (38) as a constant c to be subtracted to muography observed data in the muography misfit function, where c can be evaluated by minimising Eq. (38) in a least-square sense (LSM method). Another approach is, for example, to treat c as an unknown scalar parameter in the inversion. They evaluated the impact of several different approaches on a specific scenario, that is the Puy de Dôme, and verified that the most successful one is the least squares minimisation method, but many of the other approaches tested provided somewhat helpful results and may have some merit for general scenarios.

4.2.8. Back-projection method

As already mentioned, typically the muographic imaging provides a 2D map of muon transmission as a function of the angular coordinates which define the directions of particles, assuming the detector to be considered as a single point. The point-like approximation of the detector is valid only if the distance between the detector location and the target is big enough with respect to the size of the detector, as is the case of volcanoes. Otherwise the detector has a sort of stereographic view that means different parts of the detector see the same object under different angles. This feature can be used to localise objects or cavities hidden inside large material volumes. The algorithm, called *back-projection method* [105] allows to obtain the size and distance from the detector of an object which is observed as an *anomalous region* on the muography. The algorithm consists in the definition of custom surfaces at different distances from the detector where the reconstructed tracks can be projected by backward propagation as straight lines. A higher density of hit points is thus expected in correspondence of the projection of the object on each surface. The angular width subtended by these regions with respect to the detector's centre depends on the position of the back-projection plane. The size of the angular width just defined decreases going from the detector to the object location, and then increases slowly at higher distances, remaining near the minimum value along the extension of the object. The minimum angular width is thus reached when the back-projection surface approaches the object. The distance between the plane where the minimum is reached and the detector thus allows the localisation of the object while the linear extension is given by the linear extension of the anomalous region on the plane corresponding to the minimum angular width. This method has been tested with both laboratory measurements for metal detection and on-field measurements inside the Temperino mine in Tuscany (Italy) for the identification of large cavities [106].

4.2.9. 3D modelling of a cavity

A new approach to the three-dimensional muography of underground structures, capable of directly localising hidden cavities and of reconstructing their shape in space has been developed by Cimmino et al. [91], merging informations of measurements performed from different locations around the object. The example in [91] concerns the 3D modelling of a cavity in the Mt. Echia environment, a tuff hill with several cavities, combining three different 2D muographies of the cavity. The novel method to reconstruct in space a hidden cavity, starts by defining a grid of points in a cubic volume that encloses the region of space where the cavity is supposed to be. As a general criterion, a point was considered to be located inside a cavity if in each of the three projective muographies it corresponded to a direction lying inside a signal cluster. This procedure was tested by simulating the presence of differently shaped voids, approximately located at the presumed position of the hidden cavity and having a similar size. The results of the simulation show that the real structure is always comprised in the reconstructed object, but it contains also points that in a projection appear in the shadow of the cavity, rather than inside. This contribution can be more and more reduced by adding other points of view. Compared with the single muographies, that are 2D muographic images, they demonstrated that this method has a high power in identifying, localising and reconstructing in space hidden cavities in complex systems, resolving in matter ambiguities that affect 2D muographies.

4.2.10. Background

As mentioned in Section 4.2.4 the possibility of achieving a high precision on density measurements is strictly related to an adequate control of the signal to background ratio. Indeed, several attempts to obtain a muographic image of volcanoes failed to make clear observations due to background noise. The background contamination can be significantly elevated, especially when large rock thicknesses (hundreds of meters or more) are involved. This can lead to an overestimation of the muon flux and consequently to an underestimation of the average density. In the last years, thanks to on field experiments and to synthetic models, many advances in the understanding of the possible sources of background and on models for quantitative estimation of their intensity and of their energy spectrum have been achieved.

A possible way to classify the different typologies of background is the following (see also Fig. 15): accidental tracks, scattered (non ballistic) muons, scattered electrons and hadronic background (see also [56,107]).

Accidental coincidences happen when two or more different particles hit, in the coincidence time window of the electronic detector, the sensitive planes of the detector. This can happen for un-correlated particles or for particles coming from the same cosmic shower, in the last case the particles are spatially and temporally correlated. In the case of a detector with just two sensitive planes the two hits define automatically a background track. This was the case of the *first generation* detectors used, for example, in [53,108]. The occurrence probability of accidental tracks may be considerably reduced by using three or more detection planes, as already proposed in [109] and requiring the alignment of the three or more points measured. Moreover, a short coincidence time window could reduce false tracks further, at least for non correlated particles.

A muon coming from a direction different from the measured one is called a *scattered* or *non ballistic* muon. The scattered muon can come from the *backward* direction, and sometimes they are called *upward-going* background muons or from the *forward* direction, and in this case they are also called *downward-going* muons. In the first case measuring the direction with a time of flight technique or by a Cherenkov detector [110] they can be identified. The forward scattered muons are indistinguishable from the signal muons, and the only way to control their contribution to the signal/background ratio is an energy cut that is favourable, as it is described below.

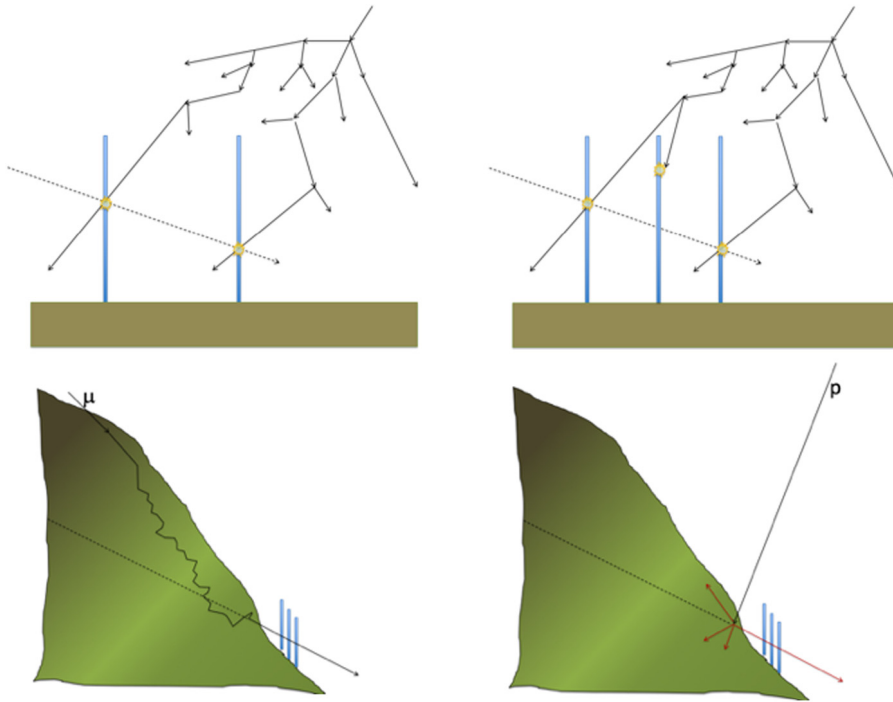


Fig. 15. Pictorial representation of some background types. Top-left: two particles hit simultaneously the two detector layers, producing a fake track represented by the dashed line. Top-right: a third detector layer reduces the probability to have simultaneously aligned background hits. Bottom-left: a muon (solid line) is scattered by the shallow part of the mountain and it is reconstructed as a muon coming from the inner part of the mountain (dashed line). Bottom-right: a hadron, a proton in the example, interacts with a nucleus of the mountain producing new particles that can be interpreted as muons that have crossed the mountain.

Scattered electrons are similar to scattered muons, they are electrons coming from the atmosphere that deviated from their original direction and entered in the detector acceptance. Since electrons lose their energy in matter much more than muons (of the same energy) and can produce *bremsstrahlung* radiation, they can be more easily absorbed or identified by the use of absorber material interposed inside the detector that can stop, deflect or generate electromagnetic showers.

Hadronic background can be of different types: protons from the primary cosmic radiation or any other particle (including electrons and muons) produced by hadronic interaction of the protons or neutrons with the matter, in particular with the topographic material surrounding the detector.

The decay products of radioactive materials present around the detector are usually considered negligible because their energy is not sufficient to generate a track through the detector planes or their activity is not sufficiently intense to generate accidental coincidences.

Many experiments on volcanoes had to deal with background. As already mentioned in 4.3 the results published in [111] were quantitatively re-evaluated in [112] mainly because in the first data analysis the background contribution at low elevation angles was underestimated. The experiment of [53] at the Mt Etna showed clearly that the low measured value of the density was due to a large component of background. Successively the analysis conducted by Jourde et al. [113] of datasets acquired on Mount Etna and on La Soufrière of Guadeloupe [114] revealed that upward going background flux is present when the rear side of the telescopes is exposed to large and deep valleys, and its intensity may amount to 50% of the measured total flux in given directions.

The contribution of low energy particles to the background of a muography experiment has been studied in detail by R. Nishiyama et al. using emulsion film detectors [92]. In particular they used two types of emulsion detectors with different momentum thresholds: one is a stack of four emulsion films (Quartet detector). The other is a stack of 20 emulsion films and nine 1-mm-thick lead plates, the so-called Emulsion Cloud Chamber [115]. Stacking several emulsion films allows to impose an energy threshold on the incident particles by analysing the straightness of the tracks. The straightness is evaluated by using the deflection angle of the tracks in the adjacent films. Owing to the lead plates inserted between the films in the ECC detector, this straightness leads to the detector gaining a higher energy threshold (~ 1 GeV) than the Quartet detector (~ 50 MeV). The particle-flux estimated from the quartet detector is much higher than that from the ECC detector. Considering the different momentum thresholds for the two detectors, this difference in flux arises from the low-momenta particles in $0.2 \text{ GeV}/c < p < 2 \text{ GeV}/c$. While the density values determined from the ECC detector are consistent with the density of typical volcanic rocks, the density values determined from the quartet detector are significantly lower. This fact suggests that while the ECC detects only the signal muons, the quartet detector is affected by contamination from

other low-momentum particles. This soft background is mainly composed of electromagnetic components of air showers, and by muons deflected at large angles through the material.

In [116] a background measurement at Puy de Dôme volcano is presented. MU-RAY and TOMUVOL collaborations made independent measurements of the atmospheric muon flux transmitted through the Puy de Dôme volcano using their first prototype detectors. The results confirmed that an important bias comes from background contamination mimicking a higher transmittance. Indeed, they measured, behind rock depths larger than 1000 m, remnant fluxes of 1.83 ± 0.50 (syst) ± 0.07 (stat) $\text{m}^{-2} \text{d}^{-1} \text{deg}^{-2}$ (MU-RAY) and 1.95 ± 0.16 (syst) ± 0.05 (stat) $\text{m}^{-2} \text{d}^{-1} \text{deg}^{-2}$ (TOMUVOL), that roughly correspond to the expected flux of high-energy atmospheric muons crossing 600 m of water equivalent (mwe) at 18 degree elevation. These results show the necessity of technologies able to reduce the background, for example using time of flight measurement, to reject upward going muons, or particle identification capability to reduce the soft component of cosmic rays.

Different simulations have been performed in order to understand the composition, the energy and angular distribution of the background. It should be emphasised that *full* Monte Carlo Simulation, i.e. a complete transport simulation of the muons and/or other cosmic particle through the real geometry under investigation and in the atmosphere are not computationally feasible. For this reason simplified object geometries and/or optimisation of the transport of the particles have been used in the literature.

In [107] the focus was on the composition of the background and of its energy spectrum. For this reason the energy spectra of major cosmic particles produced by primary protons and helium nuclei have been simulated using the air-shower simulation code COSMOS. The propagation near a detector and a mountain has been simulated with the GEANT4 toolkit. In order to simplify the computational problem, an ideal topography with a rotationally symmetric shape of the Mt. Showa-Shinzan was simulated together with a virtual detector, with the same symmetry of the mountain. The results showed that the background is composed by low-energy electrons, muons and protons, with energy below 1 GeV. The simulation also verified the existence of both backward and forward background that decreases with an increase of the elevation angle. The synthetic results are in good agreement with the experimental values of background measured with nuclear emulsions at the Mt. Showa-Shinzan and reported in [92]. Furthermore good agreement with the background estimation reported in [113] was found.

In [117] the Monte Carlo simulations were focused to evaluate the effect of the forward scattered muons, for different object geometries and compositions. In particular two physics cases have been studied. The first one concerns an archaeological target, the Apollonia tumulus near Thessaloniki in Greece, and the second case of study is La Soufrière volcano in Guadeloupe Islands of the Lesser Antilles. In order to solve the computational problem two steps were performed. In the first step a full GEANT4 simulation was performed for muons of energy below 10 GeV and for different incident angles with respect to the ground. From this simulation the expected background flux for forward muons can be evaluated. In the second step the expected signal and background were estimated for the two targets with a simplified geometry and without performing the full simulation.

The result concerning the archaeological structure, that can be in some way extended to similar structure, shows that the forward scattered muons on the object surface do not significantly disturb the muographic image. Different conclusions are reported concerning the volcano simulation. The contribution for muons of energy greater than 5 GeV is negligible for all the impact directions. For the lower energy muons, most of the *efficient* scattering processes (i.e. when the scattered particle exits the medium) occur if the zenith angle of the incident direction is higher than 85 degrees and do not exist if this angle is lower than 80 degrees. The contamination of forward scattered muons is not negligible and needs to be corrected. Indeed, a significant influence of the forward scattered has been observed muons through a model based on La Soufrière volcano in the measurement, which can represent up to 50% of the detected muons, and even more for incident zenith angles higher than 85 degrees.

The problem of the estimation, with a full transport simulation of the muons through a not simplified but realistic model of the mountain was solved by V. Niess et al. [118]. They implemented a backward Monte-Carlo technique for the muon transport problem. Backward sampling can provide drastic CPU gains by simulating only events that can be observed, because it provides a simple way to invert the simulation flow in a muon transport MC starting from final states. This technique is a more flexible version of an adjoint MC, where the detector is considered a source of muons that are propagated backward through the mountain gaining energy and experience multiple scattering.

A proof of principle has been provided using a dedicated library implemented for muography imaging: PUMAS. The agreement between the forward and backward sampling results is better than the 0.1% MC error at high energies. At low energy, due to an approximate backward procedure for the fluctuations in the ionisation loss, systematics of 1% can be observed. However, this systematic is washed out when considering that muography imaging uses atmospheric muons with a broad energy spectrum.

Despite the fact that the simulation can provide only the scattered muon component of the background, the detailed transport approach and the use of a realistic model of the mountain (a Digital Elevation Model can be used) provide important information on the expected background flux. The PUMAS code has definitively shown that the amount of background is very dependent, for the same mountain, on the detector position since the real topography of the mountain flank and of the areas surrounding the observation site can have important effects. The use of such a simulation is recommended for the choice of the site of observation of a mountain.

4.3. The study of volcanoes

4.3.1. Volcanoes in Japan

The revival of the muon radiography, after the pioneering experiment of L.W. Alvarez, has been triggered by the application of this technique to the study of Japanese volcanoes. In 1994 the use of muography to investigate the structure of a volcano was proposed [109]. A simple tracking system made of plastic scintillator bars was used to measure the muon flux across the Mt. Tsukuba and a possible use for volcanic eruption predictions was proposed. In 2013, about 20 years later, for the first time, evidence of a measurement of the magma dynamics in a volcanic conduit was given [119], showing that radiography can be potentially used as a tool to detect precursors of eruptions (see Fig. 16). The experiment measured the change in the average density along the conduit of the Satsuma-Iwojima, a small scale volcano with a large amplitude and low frequency motion of magma. For this kind of measurements one of the most crucial element is the *time resolution*, i.e. the time needed to resolve a density variation inside the volcano. This is of course strictly connected to the number of muons collected per day. The statistics is proportional to the time of acquisition and to the sensitive area of the detector. The detector size was $1.7 \times 1.7 \text{ m}^2$ of sensitive area with a distance of 3 m between the first and last plane. Six layers of scintillation-sensitive planes were present and five 10 cm thick lead plates supported by ten 3 cm thick steel plates were alternating for the background reduction (see Section 4.2.10). The detector collected 1.75 muons per day in each bin ($33 \times 33 \text{ mrad}^2$) after passing 800 m of rock ($\rho = 2.0 \text{ g/cm}^3$) in the case the conduit, 400 m large, is empty. In the hypothesis the conduit is filled with magma with the same density of the rock the muon flux reduces to 0.37 muons per day. The difference between an empty and full conduit can be detected in 3 days at a 2σ (95%) confidence level.

The previous example shows clearly that large area detectors are needed if the time resolution must be reduced. Gas based detectors, which can be less expensive with respect to plastic scintillator based detectors to cover large areas, can be a valid alternative to increase the effective surface, as in the case of the muographic laboratory at the active volcano Sakurajima (Kyushu, Japan). For this laboratory, which has the largest active area of detectors in the world, multi-wire proportional chamber gas detectors (MWPPC) are in use [120]. Each detector has $0.8 \times 0.8 \text{ m}^2$ of sensitive area and 4 mm spatial resolution. The distance between the first and last plane is 2 m, corresponding to an angular resolution of about 2 mrad. Since the distance between the observatory and the volcano is $\sim 2.7 \text{ km}$, the spatial resolution on the volcano is $\sim 7 \text{ m}$. Each tracker is made of at least five planes and five 2 cm thick lead plates for background suppression. Seven detectors are installed in the laboratory, with a total sensitive surface of 5.5 m^2 . The modularity of the detectors allow to increase the total surface in case of need. The system showed quite stable operating conditions during long data tacking campaigns (larger than 100 days), with tracking efficiencies above 95%.

The Sakurajima-Iwojima volcano was initially studied with a simple detector, consisting of just two layers of plastic scintillator bars with an active area of 1 m^2 and a distance of 2 m between the two planes. The angular resolution was 16 mrad and the distance from the summit crater about 1.4 km. The results published in [111] were quantitatively re-evaluated in [112] mainly because in the first data analysis background contribution at low elevation angles was underestimated. The presence of a low density region, $0.9 - 1.0 \text{ g/cm}^3$ with a diameter of 300 m at $135 \div 190 \text{ m}$ from the summit crater was, anyway, confirmed and interpreted as a rhyolitic magma with a 60% vesicularity.

In the time period between the first experience of Mt Tsukuba, in the year 1994, and the recent realisation of a laboratory to study Mt Sakurajima, many other volcanoes have been studied in Japan. For these measurements both electronic detectors and nuclear emulsion (NE) were used. The first experimental measurement of the density distribution concerned The Mount Asama, in 2007 [50,121], where a Nuclear Emulsion detector of 0.4 m^2 area was installed in a 1 m deep underground chamber at about 1 km distance from the volcano, taking data for 2 months. Two strong density anomalies were observed, with an accuracy of 1%–2% and vertical and horizontal spatial resolution of 30 m and 60 m, respectively. Successively Mount Asama was monitored with a real time muon detector with an angular resolution of $\sim 60 \text{ mrad}$ corresponding to $\sim 72 \text{ m}$ of spatial resolution at the centre of the crater, 1.2 km distant from the telescope. The detector was operating since October 12 2008 when, on the 2nd of February 2009, the volcano erupted and a large amount of volcanic ash was ejected. The comparison of the measurement before and after the eruption allowed for an estimation of the amount of material ejected, in good agreement with the model calculation of volcanic ash flow. Moreover, the visualisation of the mass density images suggested that a *boiling liquid expanding vapour explosion* occurred, since no mass variation was observed below the crater.

In [122] an airborne muography of the Heisei-Shinzan lava dome of the Unzen volcano is described. An array of 14 scintillator bars was used to form a segmented detector with an active area of $49 \times 49 \text{ cm}^2$. The distance between these segmented detectors was 16 cm, corresponding to a spatial resolution of $\sim 90 \text{ m}$ on the target. The detector was installed inside a helicopter and the muon flux was measured for 2.5 h at an altitude of 1350 m and a horizontal distance of a few meters from the steep surface of the Heisei-Shinzan lava dome. The principal claimed advantage of this technique consists in a shorten exposure time of the measurement. By getting the detector as close to the target of interest as possible the viewing solid angle of the region of interest is maximised and, as a consequence, the recorded number of muons that pass through the region is also increased. If the distance to the target is reduced to a half of the original value, it will take a quarter of the original time to produce the same quality images. Another advantage is that the rock thickness to look through the target volume is minimised. The topography around a volcano is usually complicated and it is generally difficult to get a clear pathway from the target volcano to the land-based detector. Reducing the thickness of rock is very efficient: if the rock thickness is reduced to a half of the original value, the transmitted muon flux will be 10 times

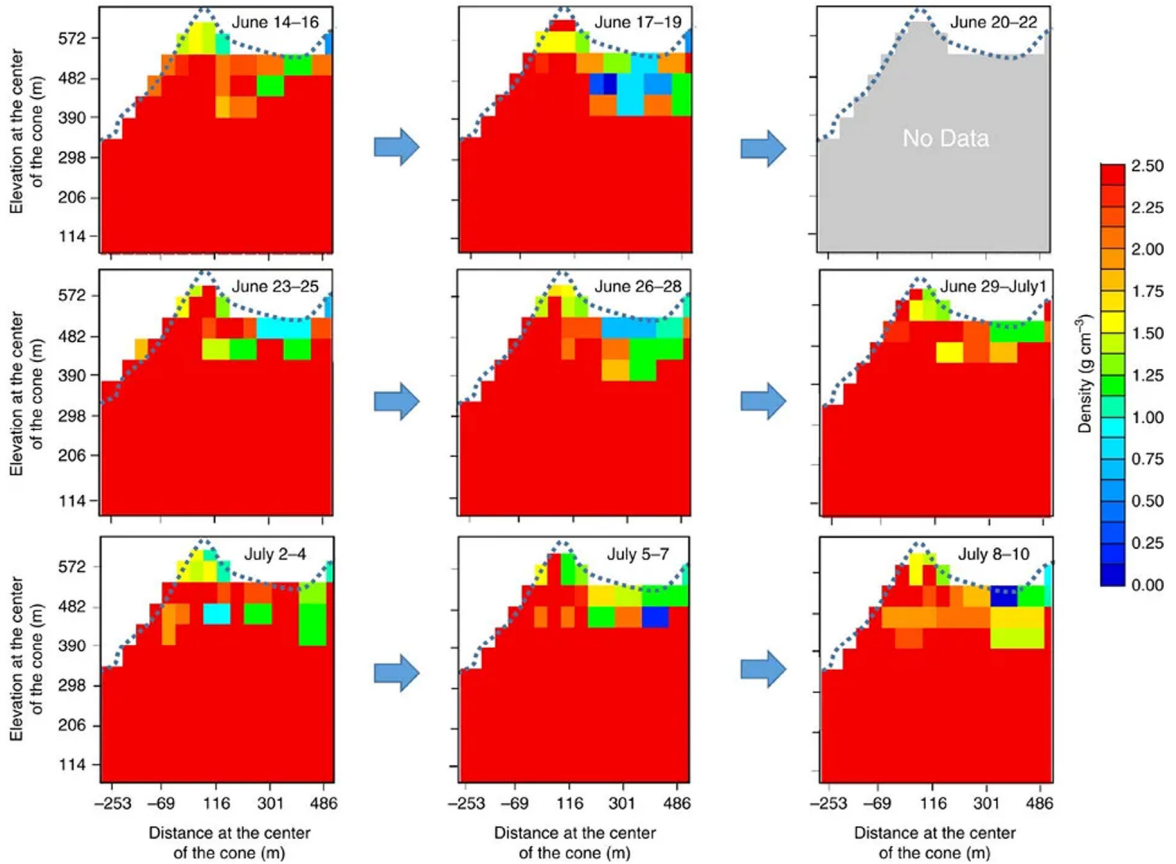


Fig. 16. Magma dynamics during the Satsuma-Iwojima eruption. The plots show the angular distribution of 1σ (68% CL) upper limit of the average density along the muon path. The frame rate is 10 frames per month. The data were not taken during 20–22 June due to a blackout. Horizontally adjacent two bins were packed in order to achieve higher and more accurate statistics. The elevation and horizontal distances at the centre of the cone are shown.

Source: Courtesy of [119].

higher. As a consequence of this effect the airborne measurement is expected to shorten the time required for imaging the peak region of the dome by more than 2 orders of magnitude in comparison to other 2 land-based measurements that were performed. Other advantages are: no topographic and infrastructural restrictions, electricity availability, fast transportation and installation of the detector.

In the bibliography a list of articles concerning the research in Japan is available. As last examples it is worth mentioning the 3D reconstruction of Mt Asama [94] performed by two observation points and the comparison of muographic results with classical gravimetry [123]. The 3D inversion methods have been discussed in more detail in Section 4.2.6.

4.3.2. Volcanoes in Italy

As in Japan, in Italy there are active volcanoes: Vesuvius, Etna and Stromboli have been object of investigation in these years by the use of cosmic muons. The state of research on these volcanoes will be briefly discussed below.

Vesuvius is considered one of the most dangerous volcanoes of Europe and of the world. It can manifest very violent eruptions (*Plinian eruptions*) and a large population, about 3 million, lives around the volcano. More than half a million inhabitants lives inside of the so-called *red zone* that must be evacuated in case of a possible eruption. In the 2009–2012 period, the Italian National Institute of Nuclear Physics (INFN) funded a research and development project on muon radiography applied in particular to the study of Vesuvius. The MU-RAY and MURAY2 [54,55,124] designed a new class of particle detectors based on plastic scintillator bars coupled to silicon photomultipliers (SiPM). A prototype (1 m² of active area) was realised and operated for a test run at the Vesuvius, in collaboration with the Italian National Institute of Geophysics and Volcanology (INGV) [125] and successively at the Puy de Dôme volcano, France, in the framework of a collaboration with the project TOMUVOL [116,126]. MURAVES is a INFN-INGV project funded by the Italian Ministry of Research and Education based on the experience of the MU-RAY program. The experiment is taking data at the Vesuvius [56,106,127,128]. Three 1 m² muon hodoscopes have been installed in a laboratory realised on the slope of Vesuvius and equipped with a photovoltaic system. Each tracker consists of four XY layers and a 60 cm thick lead wall

placed before the last XY layer to suppress the background. With a sample equivalent to two years of data taking the experiment could resolve density variations of 5% in the upper part of the Vesuvius Gran Cono. Due to existing gravimetry and electrical maps it will be possible to combine them with the muographic data to provide a better understanding of the structure of the Gran Cono.

Stromboli is a large strato-volcano of the Aeolian archipelago, in the south of Italy. Its altitude is about 920 m above the sea level but the submarine portion extends down to about 1000 m depth into the sea. The volcano is characterised by the emission of huge amounts of gas, explosive activity (the so called *Strombolian activity*) and repeated collapse episodes that can produce tsunamis with potential danger for the islands of the archipelago and for the coast facing to the south Tyrrhenian sea of Italy. A muography of the internal structure of the summit crater area has been performed by the use of emulsion films [129]. The detector, with an area of 0.96 m^2 took data for about five months. It was placed at an altitude of 640 m a.s.l., optimised for the study of the crater region that is around 750 m a.s.l. A clear excess of muon flux in the crater zone, from the surface to the depth of about 50 m, indicates the presence of a lower integrated density region that extends laterally for about 200 m below the crater region. This excess corresponds to a decrease of the average density along the muon path down to 1.4 g/cm^3 (calculated with a reference rock density of 2.2 g/cm^3). Mt. Etna, located in the East coast of Sicily, is a very active *strato-volcano* that can present eruptions from its four summit craters or from vents or fissures. It has a height of about 3350 m, and the base is about 40 km in diameter.

A first attempt to study this volcano by muography was performed in 2010 [53]. The target of the measurement was the Southeastern Crater (240 m tall, about 500 m of base diameter). The muon detector was made of two XY planes made of plastic scintillator strips. The sensitive area of each plane was 1 m^2 and the distance between them was 170 cm. One of the goals of the experiment was to understand if the amount of background present in a two-plane detector was sufficiently low to permit a density measurement of geological structures with thickness of the order of 500 m, confirming the results presented in [111], with a similar target, or if detectors with three XY planes have to be preferred to reduce the amount of background. For more details on the background see Section 4.2.10.

The results obtained showed clearly that the measured muon flux across the volcano exceeded the expected flux by a factor of about ten. The expected flux was computed with a bulk density of the rock of 0.7 g/cm^3 , on the base of a gravity/GPS measurement campaign performed in 2010. Therefore the excess of muons measured with respect to the expected one cannot be attributed to a too high value of the density of the rock in the synthetic model with respect to the real one. The origin was attributed to the accidental background component due to false muon tracks that may arise, for example, from vertical particles that hit simultaneously the two planes of the detector (see Section 4.2.10). In the article a rough estimation of the probability to have this accidental track is presented and the result is compatible with the observed measurement. In spite of the huge amount of background in the measurement, that is incompatible with an accurate estimation of the density distribution inside the volcano, an indication of a lower opacity region was shown, after the subtraction of the background as predicted by the synthetic model.

Mt Etna is also studied by two other projects. In the MEV experiment [130,131] a dedicated detector, based on plastic scintillator bars, has been realised. The tracker consists of three XY planes of 1 m^2 of area and a distance, between the first and the last plane, of 97 cm. The planes are inserted with the light sensor and required electronics, in a cubic box with external side of 1.5 m to ensure light and water insulation. The detector is powered with two photovoltaic panels and the overall power consumption is about 25 W. In 2017 a test phase of about 110 days of data acquisition was performed, measuring the extinct volcanic cone of Monte Rossi (Catania, Sicily) that is similar, in shape, size and distance from the telescope, to the real object of investigation, the North-East crater of the Etna volcano. The test confirmed the good performance of the detectors but also the need to improve the data analysis. The detector was, successively, placed close to the North-East crater and two data samples were acquired, in 2017 and 2018. Data analysis of the samples is in progress. The logistic conditions exclude the possible use of a lead wall or other shielding techniques to suppress background. For this reason the group is looking for the introduction of a time of flight measurement or of a Cherenkov based detector to discriminate forward muons from backward muons [47,110].

The other group is proposing a different detection technique, in particular a Cherenkov telescope designed in the context of the ASTRI project [132] for γ ray astronomy by the use of an Imaging Atmospheric Cherenkov Telescope. The proposed detector is a simplified version of the ASTRI prototype: dimensions are smaller and weight lighter in order to be less expensive and easy to install [47,82]. A muon in the atmosphere needs to have an energy greater than about 5 GeV (at sea level) in order to emit Cherenkov light. The intrinsic threshold on the muon energy makes the detector much less sensitive to backward muons than other technologies. The actual energy threshold is higher because a minimum amount of photons is needed to reconstruct the muon direction with sufficient precision (the ASTRI-SST-2M prototype will be able to reconstruct muons with a precision on the direction of about 0.14° , if the muon energy is higher than 20 GeV). On the other hand a high threshold reduces the number of signal muons emerging from the rock. Another disadvantage of this technology is that they can only operate at night, reducing the effective data taking capability.

A feasibility study was performed, with a simplified model based on the ASTRI-SST-2M prototype and a volcano geometry represented by a simple cone of base 500 m and height of 240 m, roughly corresponding to the dimensions of the South-Est(SE) mouth of the Etna volcano. With a distance between the telescope and the volcano of 1500 m the projected spatial resolution referred to the axis cone is about 4.5 m. Cylinders of various dimensions (200, 144, 75 and 27 m diameter) have been simulated and the time necessary to resolve, at a 68% confidence level, the difference between an empty conduit and a full one was estimated. As an example a minimum of 3.7 nights is necessary in the case of a 200 m

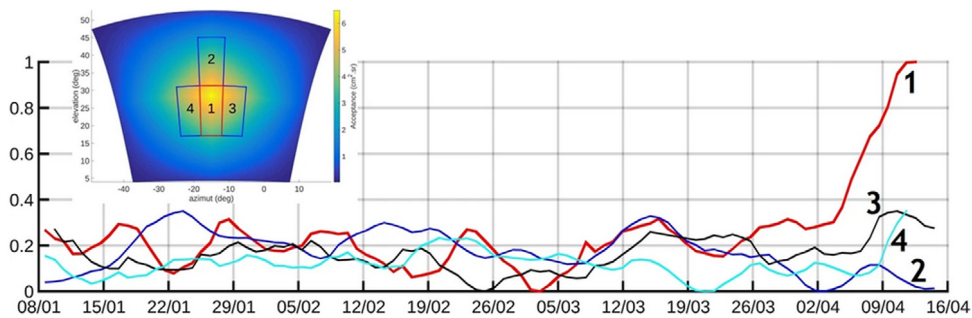


Fig. 17. Time variations of the muon flux across different domains of the lava dome. The red curve is for the bundle of lines of sight covering the seismic source zone and corresponding to the direction of the hydrothermal source. The other three curves are for adjacent areas labelled 2, 3 and 4 in the inset showing the acceptance function of the telescopes view-field. Oscillation amplitudes are arbitrarily set to a common value. The total acceptance of bundles of lines of sight crossing the source area 1 is $54.3 \text{ cm}^2 \text{ sr}$. The acceptances of the merged lines of sight in the areas 2, 3 and 4 are respectively $34.8 \text{ cm}^2 \text{ sr}$, $40.3 \text{ cm}^2 \text{ sr}$, and $45.8 \text{ cm}^2 \text{ sr}$. For comparison, the maximum acceptance of the field of view of the telescope equals $6.5 \text{ cm}^2 \text{ sr}$. The abrupt increase of the muon flux showed in curve 1 is interpreted as a genuine decrease of the density in the hydrothermal source, since the other three curves are not changing.

Source: Courtesy of [135].

in diameter and 135 m in height conduit, corresponding to a maximum magma velocity of 5 m/h. The authors report also a sensitivity comparison between the simulated experimental setup and the measurement performed in [119]. Taking in account the two different background fluxes, a factor of ten improvement is expected, in spite of the reduced duty-cycle of the Cherenkov detector. A validation test of the synthetic model will be possible when the ASTRI SST-2M prototype will be operative, pointing the telescope to the Etna from a distance of 5 km and measuring the attenuation across the South-Est crater, 500 m thick.

4.3.3. Volcanoes in France

Two main collaborations are active on the front of the study of Volcanoes in France. The TOMUVOL collaboration [67,68] focused the research activity at Puy de Dôme, located in the Chaîne de Puys volcanic district in France. The DAFNE group focused its attention mainly on La Soufrière of Guadeloupe, an active volcano in the Lesser Antilles.

Puy de Dôme is an extinct volcano with an altitude of 1465 m a.s.l. and a lateral extension of more than 2 km at the base. Even if it is not very significative from the geological point of view the Puy de Dôme was chosen as a *test laboratory* for the development of muon radiography (detectors and methods) applied to volcanoes. As a matter of fact the volcano edifice is isolated, so that there is no muon absorption from other structures, the size is moderate enough allowing measurements of a large part of the edifice, and can be observed from many locations, most of them with infrastructure reachable by roads and served by electricity. Two measurement campaigns, with almost orthogonal directions, were performed in 2011 and 2012. There was then a third campaign of 41 day between 2013 and 2014. The used technology was gas based detectors (Glass Resistive Plate Chambers GRPC). The results of these last measurements were published in [116] together with the results of a measurement campaign performed at the Puy de Dôme by the MU-RAY group. The comparison of the results obtained by the two groups with different detector technologies and independent analyses showed how important the contribution of the background and the necessity of its reduction for the study of structures with 500 m or more of rock (see Section 4.2.10) can be. The Puy de Dôme was also used as model for the study of joint inversion methods [104,133] that are reported in Section 4.2.6.

The La Soufrière of Guadeloupe volcano has been object of an intense program of investigation by muon radiography, sometimes in combination with other classic methods, gravimetry in particular [102,113,114,134,135]. In [134], for example, a calibration experiment has been performed using a water tower. In [135] an increasing of activity of a hydrothermal spot with excellent space and time resolution, using a combined analysis of the seismic noise and muon radiography, is reported. The measurement is particularly interesting because no reliable precursory signal is known for phreatic and hydrothermal eruption which can be very dangerous and have a very short timescale, between hours and days. A plastic scintillator based detector with three XY planes of $50 \times 50 \text{ cm}^2$ area measured an increase in the muon flux across the lava dome in the direction corresponding to a seismic source volume identified by seismic data analysis. A simultaneous change in the muon flux and in the temperature measured by probes in active vents was observed, due to a correlation with a hydrothermal event. A few days of time resolution have been estimated, that can be improved enlarging the sensitive area using several muon telescopes, which can also improve the space localisation of the hydrothermal source (see Fig. 17).

4.4. Geological applications

Besides the study of volcanoes other applications to geological cases concern the exploration of mines, monitoring CO_2 trapped in underground deposits, studies of glaciers and hydrogeological measurements. Some of them will be discussed in the next sections.

4.4.1. Mineral exploration

The possible use of muography for the application in mining geophysics was already studied in the year 1979 by Malmqvist et al. [136]. In their theoretical work the authors analysed two possible detectors, one for the use in a gallery, with a sensitive area of $0.75 \times 0.75 \text{ m}^2$, the other for the use in narrow boreholes with a diameter of 46 mm and a sensitive area of $1 \times 0.03 \text{ m}^2$. The feasibility study showed that the sensitivity of the method was enough for the detection of density anomalies. In fact they found a 1% change in the mean rock density which corresponds to a change of about 3% in the counting rate. Depending on the geologic situation, the depth and the design of the detector they found a characteristic time varying from a few hours to about 10 days. The method was found to be most applicable for massive sulfide and iron exploration. They estimated, as maximum depth for the use of the detectors, 600 m for the gallery application and 400 m for the borehole application. These numbers must be considered only as a rough indication, since the size of the detector, the size and density contrast of the target, and the maximum registration time accepted for each observation can modify them substantially.

The principle has been tested in recent years in real mines [97–100] and 3D images of dense ore bodies in complex geological environments were successfully obtained. In particular at the uranium deposit of the McArthur River mine in Canada the measurements, performed at a depth of 600 m with a gallery detector of $2.2 \times 1.1 \text{ m}^2$ of sensitive area, showed, with a 5 standard deviations statistical significance, the presence of uranium ore. The 3D density map obtained by muon data showed a good agreement with the one produced by drill assay data from the deposit. Several measurements were performed at different positions at a depth of about 600 m underground, a distance from the deposit ranging between 59 to 86 m and acquisition times between 54 days to 143 days. These measurements were performed by the CRM GeoTomography Technologies, Inc., a privately owned company spin-off from Advanced Applied Physics Solutions Inc. (AAPS, now TRIUMF Innovations), based in Vancouver; it is one of the first companies operating in this field. This kind of exploration, with a gallery telescope, is useful to search for extensions to existing ore bodies (the so called brownfield exploration). For geophysical surveys looking for new mines (greenfield exploration) miniaturised borehole detectors are needed.

In [97–99] other measurements of a different kind of ore deposit are reported. In particular at the Nyrstar Myra Falls mine in British Columbia, Canada, a volcanogenic massive sulphide deposit containing zinc, copper, lead and silver has been prospected by muography. Since the ore is only at about 70 m below the surface the data taking campaigns were of 15–20 days with a detector of 1 m^2 of active area with samples of about 1.5×10^5 muons (except one measurement of 43 weeks that collected 3×10^6 muons). The inverted 3D density images obtained had good correspondence with a model derived from drill core data.

An interesting test was performed at the Pend Oreille mine, located in northeastern Washington, USA, where a polymetallic deposit, at about 450 m below surface and with large density contrast to the surrounding dolomite, is present. Four samples were collected with two detectors positioned in four different locations in total. Data taking at each locations were of 68–153 days. The muon 3D density map was completed without any information about the ore existence and properties and compared with the known geometry of the deposit only at the end (blinded analysis). The agreement was good, also if a smearing out in depth was found. This effect has been attributed to a general issue of 3D reconstruction from 2D images. If the 2D images were acquired all from approximatively one side (below the ore in the case) the object geometry along the imaging direction is unconstrained.

4.4.2. Monitoring of carbon dioxide geo-storage

Another possible application concerns the monitoring of the carbon dioxide trapped in deep underground as proposed for the reduction of greenhouse gas in the atmosphere [63,137]. The muon detectors could be positioned under the deposit (depleted petroleum reservoir or other porous formation) using the well bore during the development of the storage site. The detector must be able to work in hostile environment (saline, high temperature). The storage sites are at least 1 km deep and must be monitored for decades if not centuries.

In [137] and [138] results from simulation are reported. They simulated a reservoir located at a depth of 1000 m beneath a cap rock with average density of 2.70 g/cm^3 . The porous rock was 250 m thick with a porosity of 35%, containing 65% of sandstone (density 2.70 g/cm^3) and 35% of brine (density 1.1 g/cm^3). Carbon dioxide is then injected (density 0.75 g/cm^3) up to a maximum of 10% of the reservoir volume. The muon flux is measured by a detector with a sensitive area of 1000 m^2 and a reference sample (before CO_2 was injected) of 1 year was simulated. Then samples equivalent to 1 year of data taking were evaluated for different fractions of injected CO_2 up to a maximum of 10% of the reservoir volume. A statistically significant difference is achieved after about 25% of CO_2 is injected.

The simulations have shown that large area ($\sim 1000 \text{ m}^2$) detectors are needed for this kind of measurement, to be posed below the reservoir. The only practical possible solution is to use an array of detectors to be placed in horizontal boreholes beneath the storage site. Boreholes of this kind are already in use in the oil industry. In [63] a prototype detector is described, based on plastic scintillator bars housed in a steel tube that can be inserted in a 9-5/8 in. borehole of the type used in the petroleum industry. The muon position along the bar is localised by measuring the arrival time of the photons. The detector was tested for two months at the Boulby mine at 1000 m of depth, in a horizontal borehole with 35° celsius of temperature showing stable conditions of work.

Another research activity concerning borehole detectors for the study of subsurface reservoirs is reported in [64–66]. A borehole detector prototype was assembled with the use of plastic scintillator rods, coated with TiO_2 , and with a hole

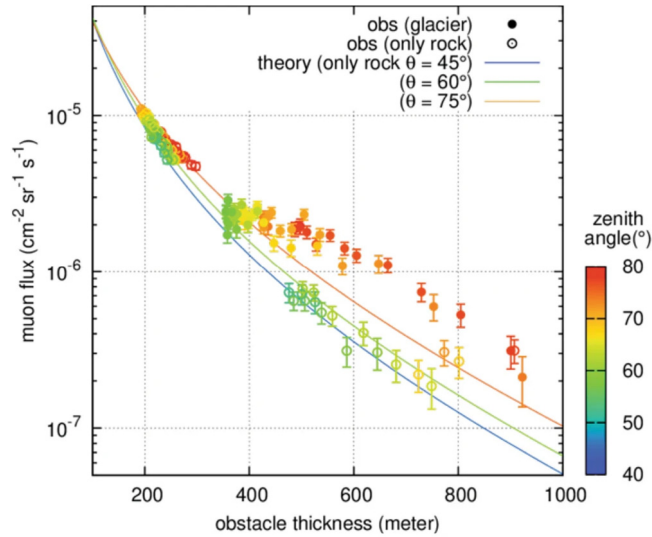


Fig. 18. Muon fluxes. Attenuation of muon flux (vertical axis) as a function of the obstacle thickness (horizontal axis). The colours of the data point represent the zenith angle of muons arriving at the detector. The open circles denote muons, which passed only through the bedrock. These data are used for calibration purposes by comparing them with the theoretical predictions of the flux attenuation in pure rock (density 2.68 g/cm^3) reported as solid lines for different zenith angles (45° , 60° and 75°). The solid circles denote muons, which crossed both the ice and the underlying bedrock. Source: Courtesy of [140].

in the centre for the insertion of a wavelength shifting fibre. Photons are read by SiPMs. The bars, of different lengths (15 cm and 68 cm) have $1 \times 1 \text{ cm}^2$ cross section and are assembled in two X-Y planes that can be inserted in a cylindrical casing of a 17.8 cm (7-in.) borehole. The angular resolution is about 3° .

Measurements were performed at the Los Alamos National Laboratory in five different locations with overburden thickness of rock between 0 m and 74 m. The measurements were performed together with another, gas based, detector with larger ($\sim 1 \text{ m}^2$ sensitive area) for comparison. Results showed the good performances of the borehole detector and its feasibility for borehole muon radiography measurements.

4.4.3. Bedrock profiles in glaciers

Recently the study of the bedrock erosion by glaciers has been performed by muography [139,140]. The study of active curving by a glacier is difficult because of the lack of information about the shape and thickness of the bedrock under the glaciers. Standard geophysical measurements are performed from the top surface of the glacier. For this reason they suffer from lower resolution in the lateral boundaries, for example between the ice and the bedrock.

A first pilot experiment was performed in 2015 [139]. Using nuclear emulsion detectors a small portion ($50 \times 100 \text{ m}^2$) of the Aletsch glacier (Central European Alps) was successfully mapped. Successively, in 2017, nuclear emulsion detectors were placed in three sites along the Jungfraubahn railway tunnel that runs under the Eiger glacier (Switzerland). The three detectors had an effective area of $\sim 1000 \text{ cm}^2$ and acquired data for ~ 100 days. The three 2D images obtained from the three different sites have been combined to obtain a 3D representation of the bedrock–glacier interface. The spatial resolution obtained on the elevation resolution of the bedrock ranges between 10 m to 30 m and the estimated ice thickness ranges between 50 m to 100 m. The reconstruction of the bedrock shape is based on the different density between the rock and the ice. For each direction the total thickness L (rock + ice) of matter crossed by muons is evaluated from a 2 m mesh digital elevation model of the mountain. The measurement of the attenuation allows the determination of the average density $\langle \rho \rangle$ that is related to the rock bulk density ρ_{rock} , known by samples of rock, and the ice density ρ_{ice} through the relationship:

$$\langle \rho \rangle = x\rho_{\text{rock}} + (1 - x)\rho_{\text{ice}} \quad (39)$$

where x represents the fraction of bedrock with respect to the ice. The boundary position is evaluated multiplying the thickness of rock L and x . The performed study showed that muography can give an important contribution to the understanding of the shape of the bedrock underneath an active glacier (see Fig. 18).

4.4.4. Fault lines and hydrogeological measurements

A possible use of muography for the measurement connected to fault lines and hydrogeological processes has been proposed in the past. In [44,141] a study of the Itoigawa-Shizuowa Tectonic Line (Japan) was proposed. A measurement campaign of 27 days was performed with a plastic scintillator bar detector of about 4000 cm^2 and 100 mrad angular

resolution. The detector was placed at a distance of 6 m from the fault outcrop. The analysis of the whole sample showed, with a 2 sigma confidence level, the presence of the fault, in the direction estimated from the geological survey.

Besides this analysis a novel approach based on the temporal variations of the density due to rainfall was presented. This method can be used to measure the depth dependent permeability of the fault. A general trend of the muon flux variation with respect to the rain-fall event was observed, also if uncertainties are too large for a clear evidence. Anyway, a permeable velocity as a function of the depth was estimated, with a trend that is consistent with expectations. Data analysis also suggests a possible unknown fault line almost parallel to the known one.

Another applications of muography to the study of hydrogeological processes are presented in [142]. Muography is proposed as a possible study of the investigation of landslides triggered by rainfall. The idea is the measurement of the time variation of the motion of the underground water table installing a detector in a drainage tunnel drilled underneath an estimated fault plane. Since there are limitations in the estimation of the underground water motion by borehole observations, the feasibility study suggests that muography can provide real time images of the water saturation levels.

In [143] another feasibility study is proposed concerning the variation of the rock density with respect to hydrogeological processes. Simulation of the variation of the measured flux is estimated for an ideal detector of 1 m² area, 10° angular aperture and 1 month of data tacking. The depth of investigation was between 60 m and 1000 m and the variation of the flux for different, water induced, density variations divided by the error have been computed for standard rock (2.65 g/cm³, $Z = 11$ and $A = 22$) as a function of the depth. A maximum depth of investigation can be defined for different levels of confidence (1 σ , 3 σ and 5 σ). As an example, a density variation of 2% can be detected with 3 σ confidence level until ~ 160 m of depth. The study also shows that the effect of the atomic composition of the rock on the variation of the muon flux is negligible with respect to the density variation at least for classical rocks without high Z elements.

A study of the time resolution needed to measure the opacity variation due to water content is reported in [144]. The muon flux variation was measured in correspondence of the variation of water level in a water tower. Two factors in particular have been studied: the effect of the statistics and variation of the signal not due to the target but to external factors as atmospheric variations.

4.5. Detection of cavities for archaeological and civil engineering applications

Muon radiography allows the search for cavities hidden inside large structures or underground. As already mentioned in Section 4.2, when muons encounter a void region while travelling across a structure, the flux measured by the detector is larger than expected in the directions corresponding to the positions of the cavity and this translates into a signal in the muography, i.e. a higher transmission is observed. The possibility of finding hidden cavities can be of interest in different fields such as archeology or civil engineering as will be described in the following sections.

4.5.1. Exploring the interior of pyramids

After the pioneering Alvarez experiment, described in Section 1, others attempted to follow his example looking for traces of undiscovered structures inside pyramids. The second pyramid examined with muography is the Pyramid of the Sun at Teotihuacan in Mexico, built by Aztecs in the 14th century. In the year 2000 this pyramid, which by volume is the third-largest pyramid in the world, attracted the attention of a group of physicists of the National Autonomous University of Mexico (UNAM), who decided to explore the internal body of the colossus by the use of muographic technologies. By chance, a deep underground tunnel exists beneath the massive structure, which is 75 m tall and 225×225 m² at its square base; this tunnel leads towards the pyramid's centre and ends with a small clover-shaped chamber. After about a decade from the start of the experiment, the most significant result is that within the pyramid there seems to be an area the shape of an equilateral triangle of 60 m side that is less dense than the rest of the structure [145].

Recently new measurements campaigns have been conducted in the terrain of Egyptian pyramids using several technologies; taking advantage of the presence of a long, walkable gallery, named Grand Gallery and two burial chambers (King's and Queen's chambers) scientists of the ScanPyramids collaboration imaged the internal structure of the Khufu's Pyramid using muon radiography [146]. Three different kinds of detectors have been installed: emulsion films along the Grand Gallery, electronic scintillator hodoscopes in the Queen's chamber and gaseous detectors from the outside of the pyramid. An indication for the existence of an unknown new chamber has been provided by emulsion detectors and confirmed by the two other technologies, installed later. This signal should correspond to a cavity similar to the Grand Gallery, with an estimated length of more than 30 m, and located 40–50 m away from the emulsion detector's position, 21 m above the ground level. The new observed chamber has been named ScanPyramid's Big Void.

4.5.2. Underground cavities and tunnels

A pioneering application of muon radiography in underground surveys has been performed in the ninety's, operating a muon tracking detector inside the *Grotta Gigante* natural cave near Trieste (Italy) [147]. The detector was a gas based tracker (glass spark counter) arranged in four layers of ~ 1 m² active area each and an angular resolution of less than a few degrees. The detector was placed in three different positions at ~ 115 m below the surface. The results showed a good agreement in the reconstruction of the thickness of rock overburden, with difference less than 2 m (in absolute value) for more than 80% of the represented surface. An anomaly of the muon flux was interpreted as the presence of a red-soil deposit confirmed by gravimetry measurement. They claimed a 3% mass variation sensitivity of the method.

Existing galleries are not always available where to install the muon detector. In these cases the construction of a borehole could be the only possibility to place a detector in depth. The first detector realised for the use in a borehole is described in [61,62]. The authors realised and tested a cylindrical tracker with a diameter of 14 cm and 224 cm height. The sensitive area has a cylindrical shape and is realised using 48 scintillating bars with wave length shifting fibres, that form the internal cylindrical surface, and two layers of scintillating fibres, 2 mm in diameter, disposed as counterclockwise helix and clockwise helix, respectively. Light pulses are fed to six photomultiplier tubes with 64 channels each. The front-end and readout electronics and a magnetic compass are positioned in the higher part of the detector. The total power consumption was 40 W, 20 W for the front-end and readout electronics and 20 W for the computer.

The performance of this detector has been evaluated in different data collection campaigns performed at two Italian archaeological sites: Aquileia near Udine and the Traiano and Claudio port, near Rome. Evidences found in these sites have been confirmed by comparison with an existing archaeological map (Aquileia site) or a geo-radar scan (Traiano and Claudio port).

A more recent study about void detection has been conducted inside the body of Mt. Echia, in Naples (Italy). Here a complex system of cavities was excavated in the yellow tuff starting from the VIII century BC. A plastic scintillator based detector, with 1 m² of sensitive area [54,55,124] was installed under a total rock overburden of about 40 m. The data analysis showed a correspondence between known chambers and muographic signals [89,90]. The observation of known cavities proved the validity of the muographic technique, so that also an unknown cavity has been found and modelled in three-dimensional shape by interpolating information from three different points of view. More details in Section 4.2.6 and in [91].

An interesting application of muography in the search for underground cavities has been developed in a cave system in Hungary under the Buda and Pilis mountains [148]; here a compact, low power consumption gaseous detector has been deployed in the Ajándék Cave to find and discover further hidden caverns. The detector has been developed accounting for all the features of this kind of site: difficulties on deployment of the detector itself, environmental parameters and in particular the high humidity, always near the dew point. The detector is based on Close Cathode MWPC and consists of four parallel layers of 1 cm thickness. Each of the detector layers provides a 2-dimensional position information with projective geometry, that is the measured hit positions in each of the coordinates of the detector plane. The first test of the telescope consisted of a data taking campaign of 50 days. After data analysis no evidence has been found for unknown caverns above the observational point of the detector.

Another case of application of muon radiography concerns the study of the ancient Temperino mine in the San Silvestro archaeo-mining park in Tuscany (Italy) [149]. The Temperino mine is now composed of a series of tunnels on multiple levels, with the shallower ones cutting through ancient mining shafts; in particular there is a large exploitation opening, named *Gran Cava*, directly connected to the surface, that was enlarged during the Renaissance era by modern industrial activity. For the measurement, the MIMA muon tracker, a transportable plastic scintillator based detector with a sensitive area of 40 cm × 40 cm was placed in a cave along the tunnel of the Temperino mine just below the *Gran Cava* and oriented vertically. The results of the experiment confirmed the good operation of the detector and the presence of the *Gran Cava* which is clearly observed with muographic measurements.

4.6. Industrial applications

Muon radiography by absorption has been tested also in some industrial applications.

In [150] a test on a blast furnace for iron making is reported. Two detectors made of plastic scintillator bars of 10 cm × 1 m with a total area of 2 × 1 m² and a distance between the planes of 1.5 m acquired data for 45 days in two different positions. The thickness of the base plane and side-walls of the furnace and the local density of the iron-rich part were measured with ±5 cm and 0.2 g/cm³ precision, respectively. The measurement was performed during a time of full operation of the furnace, that has a diameter of more than 17 m. The results open to the possibility of monitoring the status of degradation of a furnace without stopping the production.

In [151] a different method of using cosmic muons is proposed for the study of large industrial structures, in particular of blast surface. They studied the neutrons induced by nuclear absorption of negative muons. This allows to distinguish between high-Z and low-Z material. In a blast furnace up to 2 m of carbon is used internally to thermally isolate the steel vessel. Over the course of years the thickness reduces and it could become potentially critical when it reaches 50 cm. Due to the large difference in the atomic number between steel and carbon, the neutron induced method is sensitive to the relative amount of the two components of the furnace. A Monte Carlo simulation based on GEANT4 validated the trend observed in a small test experiment.

A portable muography detector for infrastructure degradation investigation is described in [152]. The detector consists of two layers of scintillating fibres connected to SiPMs. The detection area is 140 × 140 mm². The distance between planes was set to 100 mm, corresponding to 8 msrd of solid angle resolution. A test was performed on a seven story concrete building. From the measurement of the attenuation of the muon flux an image of the structural thickness was obtained that was in agreement with the expected one.

Feasibility studies for the investigation of nuclear waste silos have been performed by the use of extensive Monte Carlo simulations. In [153] the absorption technique is applied, and compared with muon MCS tomography, to a silo of cylindrical shell made of reinforced concrete, with a height of 4 m, external diameter of 4 m and 0.5 m thickness. A 1 cm

thick shielding made of stainless steel is present between the external shell and the internal part of the silo, which is filled with ordinary concrete. The detector is composed of two detection planes of plastic scintillator of two 2 m² placed 50 cm apart from each other with a spatial resolution $\sigma = 0.3$ cm and it is placed at the front face at 50 cm distance from the silo. Multiple uranium cubes of different sizes (2 cm, 5 cm and 10 cm) were placed inside the silos. Results showed that both techniques are able to resolve uranium objects with dimensions of 10 cm³ and greater with timescales in the region of one month. For objects of 5 cm dimensions, the identification depends on the position within the silo and/or the effective thickness and density of the background material in the path of the muon. Samples of uranium smaller than this limit were not resolvable due to the large extent of Coulomb scattering from the thick concrete.

5. Muon tomography

A different approach, suitable to investigate volumes with dimensions not exceeding tens of meters, can provide three dimensional tomographic images of the volume content. Applications in transport, industrial and nuclear controls are possible. As discussed above, the technique requires to install detectors to measure muons before and after they cross the inspection volume. It is based on multiple Coulomb scattering and consequently it is referred to as muon MCS tomography, or muon scattering tomography, although the information coming from muon absorption can be used as well, with the possibility to combine the two measurements, as discussed below in this chapter.

5.1. Basic principles

Muon scattering tomography was proposed in 2003 by a Los Alamos group [4]. When crossing a given material, cosmic muons, as all charged particles, are deflected. As discussed above, for particles of a momentum p , the scattering angle projected onto a plane is distributed approximately as a Gaussian with mean zero and a width σ which depends on the thickness x and radiation length X_0 of the crossed material:

$$\sigma_\theta \approx \frac{13.6 \text{ MeV}}{pc} \sqrt{\frac{x}{X_0}}. \quad (40)$$

which is a simplified version of Eq. (2).

Measuring the scattering angles allows to reconstruct information about the linear scattering density (LSD: $\lambda = 1/X_0$) of an unknown material. As it can be seen in Eq. (3), LSD is approximately the product of the atomic number Z times the density ρ : $\lambda \approx Z\rho$.

Eq. (40) assumes a Gaussian distribution of the scattering angle for monochromatic muons of momentum p . However, as shown in Fig. 2, the cosmic muons are not monochromatic and hence their scattering angle distribution is far from being Gaussian. Considering the momentum spectrum $f(p)$ of cosmic muons, the distribution is

$$\frac{dN}{d\theta} = \frac{1}{b\sqrt{2\pi\lambda}} \int_0^\infty pf(p) e^{\frac{-\theta^2 p^2}{2\lambda b^2}} dp \quad (41)$$

where $b = 13.6 \text{ MeV}/c$.

In general, the momentum of an individual particle is unknown. Nevertheless, one can consider the variance of the distribution:

$$\langle \theta^2 \rangle = \lambda x b^2 \left\langle \frac{1}{p^2} \right\rangle \quad (42)$$

where the individual momentum is substituted by a fixed value computed from the average value $\langle 1/p^2 \rangle$ of the $1/p^2$ cosmic muon distribution. From the approximate dependence of LSD on Z and ρ one can obtain:

$$\langle \theta^2 \rangle \propto x\lambda \propto xZ\rho \quad (43)$$

which relates the scattering measurements to the product of the density and the atomic number of a material. This approximate relation holds also for objects containing several elements provided the average atomic number of the compounds is considered.

However, for some application the loss of sensitivity due to lack of a momentum measurement could be too relevant to obtain the required results. In such cases it could be necessary to provide some information about individual muon momenta.

As stated above and sketched in Fig. 19, at least two detectors are necessary to detect muons entering and leaving the inspection volume and to measure the position and the direction of crossing particles. To obtain 3D imaging it is necessary to detect muons with large angular coverage and hence the detector dimensions must be larger than or at least comparable with the size of the volume to inspect.

5.1.1. Algorithms for 3D imaging

Several methods and algorithms have been proposed to reconstruct images from cosmic muon measurements. The simplest method assumes that the scattering of any individual muon is concentrated in a single point which coincides

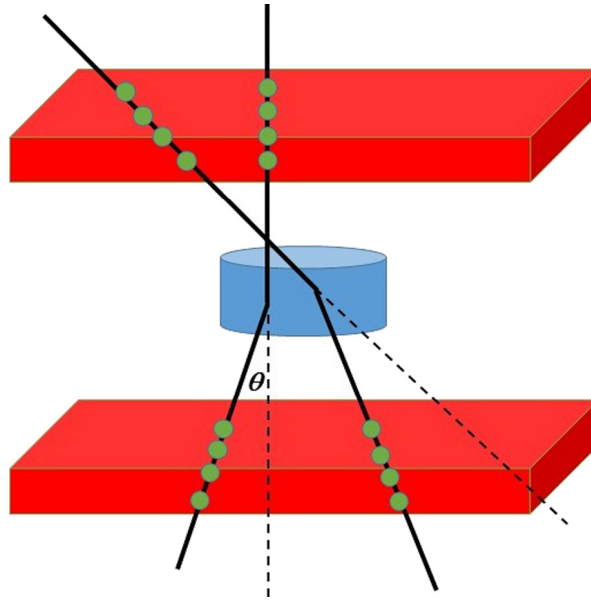


Fig. 19. Scheme of a muon MCS tomography system with two detectors (red boxes) measuring the muon trajectories before and after the volume to inspect. Scattering angles are oversized for illustrative purpose.

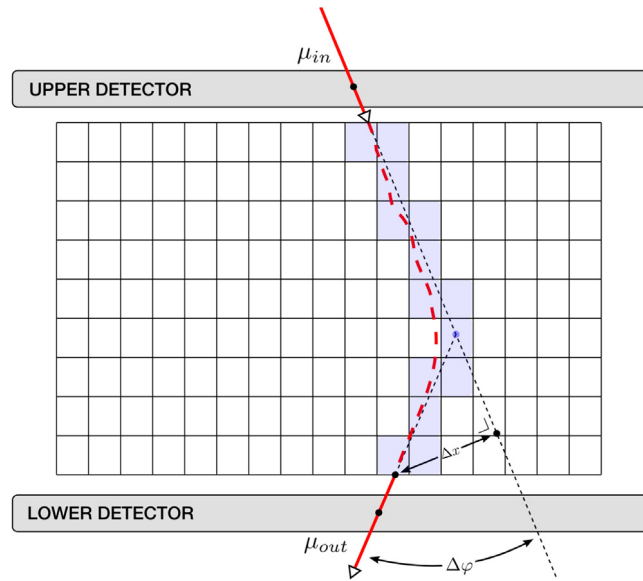


Fig. 20. Schematic representation of the scattering of a single muon. See text for details.

with the point of closest approach (POCA) of the straight lines measured by the detectors. A 3D reconstruction of the material LSD can be obtained by assigning to the POCA reconstructed for any individual muon a weight proportional to the square of the measured projected scattering angle. The method is reliable for cases with an object much denser than the rest of the volume and it is computationally very fast, but it is not precise in presence of diffused scattering centres.

A more powerful method, based on the maximum likelihood expectation maximisation (MLEM) algorithm is suitable for reconstructing volumes where the material is not homogeneous. In the following the technique will be briefly summarised. More accurate descriptions can be found in the original work of the Los Alamos group [154] and in [155,156].

The final goal of the MLEM approach is to estimate the three-dimensional distribution of the material LSD contained in the inspected volume. In particular such a volume is divided into N finite elements called *voxels*, where the LSD is supposed to be uniform. The input data are the measured scattering angle $\Delta\varphi_i$ and displacement Δx_i of each muon in the sample ($i = 0, \dots, M$) crossing the volume under inspection, as schematically represented in Fig. 20, while the result

of the overall process is the set of values of the LSD in each voxel $\{\lambda_j\}$ ($j = 0, \dots, N$). For simplicity in Fig. 20 the muon is supposed to move along a planar trajectory, perpendicular to the detectors, and the plane coincides with the drawing one. It is important to state that the displacement incorporates information about the average vertical position of the scattering process and its inclusion inside the likelihood function can improve the reconstruction quality. Another important specification is that the measurement errors must be properly handled for a reliable maximisation process.

Let us start by expressing the experimental data, that is the projected scattering angle and displacement measurements of the i th muon in a plane containing the incoming muon direction, as:

$$\Delta_i = \begin{bmatrix} \Delta\varphi_i \\ \Delta x_i \end{bmatrix} \quad (44)$$

Their covariance matrix can thus be written in the following form:

$$C_i = \begin{bmatrix} \sigma_{\Delta\varphi_i}^2 & \sigma_{\Delta\varphi_i, \Delta x_i} \\ \sigma_{\Delta\varphi_i, \Delta x_i} & \sigma_{\Delta x_i}^2 \end{bmatrix} \quad (45)$$

Considering that the i th muon has crossed n_i voxels, then the covariance matrix can be expressed as:

$$C_i = E_i + \frac{b^2}{p_i^2} \sum_{j=1}^{n_i} W_{ij} \lambda_j \quad (46)$$

where the parameter $b = 13.6$ MeV/c, p_i is the particle momentum assumed to be constant along its trajectory and E_i is the contribution of the measurement errors. Considering explicitly the length ℓ_{ij} of the path of the i th muon inside the j th voxel and the length t_{ij} of the muon path from the j th voxel to the point where the outgoing trajectory exits the inspected volume, the matrix W_{ij} takes the form:

$$W_{ij} = \begin{bmatrix} \ell_{ij} & \frac{\ell_{ij}^2}{2} + \ell_{ij} t_{ij} \\ \frac{\ell_{ij}^2}{2} + \ell_{ij} t_{ij} & \frac{\ell_{ij}^2}{3} + \ell_{ij}^2 t_{ij} + \ell_{ij} t_{ij}^2 \end{bmatrix} \quad (47)$$

The log-likelihood function of the observed scattering for the whole sample of muons, assuming Gaussian distributions for $\Delta\varphi_i$ and Δx_i , and that the muons are mutually uncorrelated, can thus be written as:

$$\log \mathcal{L} = -\frac{1}{2} \sum_i (\log |C_i| + \Delta_i^T C_i^{-1} \Delta_i) + \sum_i K_i \quad (48)$$

where K_i represents the terms not containing $\{\lambda\}$.

The maximisation of the function, to obtain the linear scattering density set $\{\lambda\}$ that best reproduces the observed measurements, is performed using an iterative process as described in [154]. If we consider the two subsequent iterative steps n and $n+1$, then the correlation between the corresponding linear scattering density sets $\{\lambda^n\}$ and $\{\lambda^{n+1}\}$ is expressed as

$$\lambda_j^{(n+1)} = \lambda_j^{(n)} + \delta_j^{(n)} = \lambda_j^{(n)} + \left(\lambda_j^{(n)} \right)^2 \frac{1}{m_j} \sum_{i, \ell_{ij} \neq 0} s_{ij} \quad (49)$$

where m_j is the number of muons crossing the j th voxel for which ℓ_{ij} is different from zero, and s_{ij}

$$s_{ij} = \frac{1}{2p_i^2} \left[\Delta_i^T C_i^{-1(n)} W_{ij} C_i^{-1(n)} \Delta_i - \text{Tr} \left(C_i^{-1(n)} W_{ij} \right) \right] \quad (50)$$

represents the contribution of the scattering of the i th muon in the j th voxel.

The method is quite complex and it may require relevant computational resources in case of large volumes to be investigated with good spatial resolution.

As an example of the image capability of the POCA and MLEM reconstruction algorithms, the acronym INFN made by lead bricks was used. Both reconstructed images are clear, as shown in Fig. 21.

The presence of detectors on both sides of the volume to investigate, allows to implement a tomographic algorithm based on the absorption rate [75,157]. Also in this approach the volume can be subdivided into voxels and, as in [75], lines of response (LOR's, lines joining elements of the external surface) are defined. The algorithm considers on each LOR the rate of absorbed muons w.r.t. the total number of muons on each LOR and compares it with the theoretical rate evaluated on the basis of the hypothetical material thickness and of the muon energy spectrum. The sum of the quadratic differences between the measured and predicted muons in each line constitutes a functional to minimise. The minimisation procedure is iterative and, at the convergence, the linear stopping power of the material in each voxel is obtained. As discussed in Section 2.2 and expressed in Eq. (1), the linear stopping power is approximately proportional to the material density ρ and then any algorithm based on absorption can produce a density map of the considered volume. Therefore, recalling the relation $\lambda \approx Z\rho$, a combination of MCS-based and absorption-based tomographic algorithms allows one to obtain a map of the atomic number of the inspected object [157,158].

Other algorithms or methods to reconstruct images are described in Refs. [159–165].

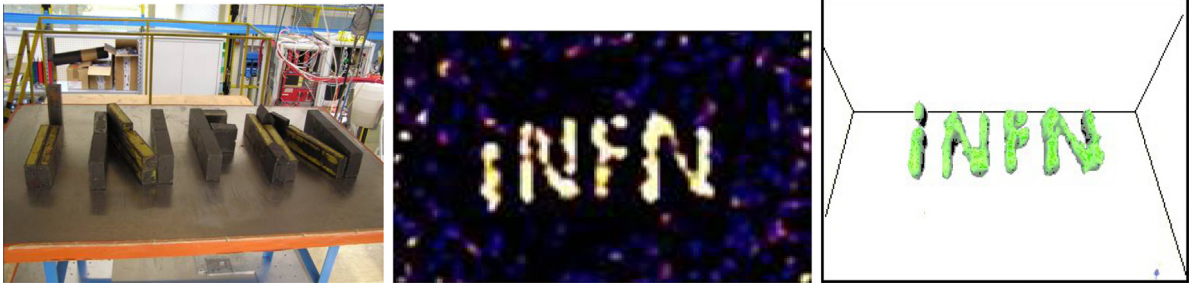


Fig. 21. From left to right: picture of the lead bricks forming the acronym INFN. Image reconstructed with the POCA algorithm. Image reconstructed with the MLEM algorithm. See text for details.

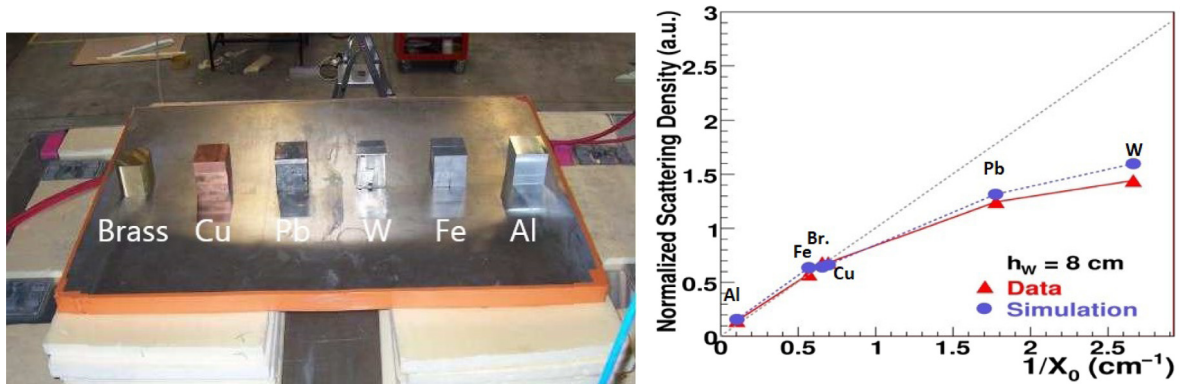


Fig. 22. Left: picture of the measured blocks of different materials. All blocks are 10 cm high except the tungsten block which is 8 cm high. Right: the measured scattering density as a function of the expected values. A saturation effect is evident and confirmed by a simulation of the same objects.

5.2. Experimental results

Several effects can complicate the description given in Section 5.1 in presence of real measurements. Clearly the detector resolution plays an important role either in the geometrical resolution of the objects to measure or in the material discrimination. On the former, it is easy to figure that the error on the reconstructed position of the muon impact on the detectors and the uncertainty on the measured particle directions would imply an amplified error, e.g. on the extrapolated position of the POCA. On the latter, the uncertainty on measured directions is affecting directly the material determination since one would have to modify $\langle \theta^2 \rangle$ in Eq. (43) with

$$\langle \theta^2 \rangle = \langle \theta_{meas}^2 \rangle - 2\sigma_{det}^2 \quad (51)$$

where $\langle \theta_{meas}^2 \rangle$ is the measured quadratic scattering and σ_{det} is the detector angular resolution assumed to be equal on the two detectors and not depending on the individual particle.

The uncertainty contributions can be taken into account when determining the material LSD as explicitly considered in Eq. (46), but other experimental effects as detector acceptance can bias the material determination. However, the largest influence on the relation between the measured scattering and the material LSD, in absence of a momentum measurement, is due to the muon energy loss and absorption of low energy particles. As a consequence, the cosmic muon spectrum is distorted and the corresponding $\langle 1/p^2 \rangle$ value changes. This effect is significant even for measurements done on relatively small objects [77] as the ones shown in Fig. 22. Six blocks of different materials (from aluminum to tungsten) have been inserted in the system described in Section 3.2.3. All samples are 10 cm high except the tungsten sample which is 8 cm high. The reconstructed scattering densities show a clear saturation effect which is reproduced by a GEANT4 simulation of the passage of cosmic muons through the same objects. Additional data recorded with Pb and W samples of different thickness show that the effect is related to the total crossed opacity.

This result illustrates the difficulty to determine the absolute value of LSD since it depends on the effective value of $\langle 1/p^2 \rangle$. Nevertheless, thanks to a proper calibration, precision measurements of LSD and of the ratio $R = \lambda/\rho$ have been obtained [166]. The measurements concerned material extracted from a blast furnace during the MU-Blast European project [74] activities. The samples had a range of LSD from coke ($\lambda = 1.30 \text{ rad}^2 \text{ m}^{-1}$) to iron oxides ($\lambda = 13.65 \text{ rad}^2 \text{ m}^{-1}$). In that case, to calibrate the absolute value of LSD, two objects of known and similar LSD were produced and measured

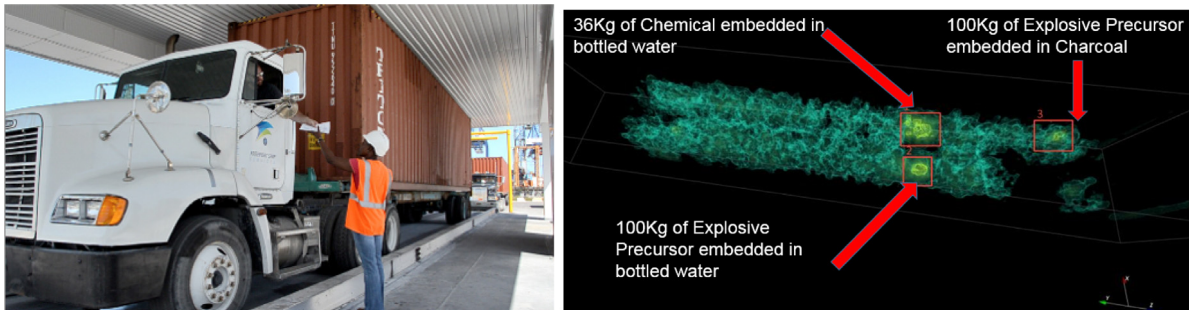


Fig. 23. Left: large area detectors of Decision Sciences® enable scanning of commercial trucks. Right: example of material anomaly detection in a three-dimensional image provided by the Decision Sciences' Discovery system.

simultaneously with the samples. Considering several systematic uncertainties that can affect the measurements, in addition to the calibration procedure, the total expected systematic error was between 7 and 10%. Since the chemical composition of all samples was known, it was possible to compute the expected value of R through the relation $R = w_i R_i$ where w_i is the mass fraction of the i th element of ratio R_i . It was then possible to compare the measured and predicted values obtaining a good correspondence: a relative r.m.s. of 4.9% with a shift of -3.2% .

5.3. Main applications: state of the art

The muon MCS tomography is perfectly suitable to study *large* volumes containing heavy materials where other techniques with more conventional probes (e.g. x/gamma ray inspection) cannot compete. The main limitation, however, is constituted by the size of detectors which can hardly exceed 10–15 m in any direction.

5.3.1. Transport controls

An important application of muon scattering tomography regards transport controls. In particular, when proposed by the Los Alamos group, the technique was indicated as a new tool to detect heavy metals in containers and trucks, to contrast nuclear contraband. This activity has reached a commercial level and portals based on drift tube technology have been realised and are now in operation [167]. As it can be seen in Fig. 23, a portal produced by Decision Sciences® can scan an entire truck and material anomalies can be detected by the system.

5.3.2. Industrial applications

An industrial application, also related to transport control, is devoted to the detection of radioactive sources in scrap metal. In containers transporting scrap metal to foundries for steel recycling radioactive sources are sometimes present. Foundry entrance is usually equipped with radiation portals but if the source is shielded by its transportation cask, realised with heavy metals as lead, the detection can fail. Consequently the source can be melted with serious consequences.

In all controls involving transports, the technique must provide a reliable response in a very short time ($\sim 2 \div 5$ min.), not to delay the transport or the industrial chain. This is an important challenge, given the cosmic muon rate. However, it has been shown, thanks to a simulation of a full scale portal for track inspection, that the technology can provide reliable controls for scrap metal contamination. Fig. 24 displays the false positive rate versus the exposition time for several lead volumes. It has also been shown that six minutes of cosmic muon collection are sufficient to guarantee 100% finding efficiency without false alarms for a small volume (2 liters).

This study, realised in the framework of the Mu-Steel European project [73], has shown that a muon tomography system, in conjunction with radiation detectors, can intercept radioactive sources within a time compatible with the metal production chain. In addition, the industrial case was emulated at the INFN muon tomography system described in Section 3.2.3. The collected data proved the capability to detect a lead volume, corresponding to a shield cask, hidden into a $\approx 1 \text{ m}^3$ box of scrap metal [156].

Another industrial application of cosmic-ray muons has been proposed for monitoring blast furnaces as described in Refs. [151,168,169]. The capability of muon scattering tomography to provide information on the distribution of the different components present in a blast furnace burden (coke, burden and reduced metal), during operation, has also been investigated thanks to the Mu-Bast project [74]. As discussed above, it has been proven, with cosmic muon data, that muon MCS tomography can measure the LSD of different materials extracted from a furnace with a precision of about 10% [166]. Furthermore, the analysis of blast furnace simulation data has shown that good images can be obtained with a complete detector coverage. On the other hand, since such a coverage would require a huge detector, a realistic setup with a pair of detectors, not exceeding 25 m^2 , placed on the opposite sides of the furnace has been simulated. The results have indicated that a measurement of individual particle momenta is necessary in order to obtain useful images of the furnace interior. It was therefore necessary to design and simulate a detector capable to provide a momentum

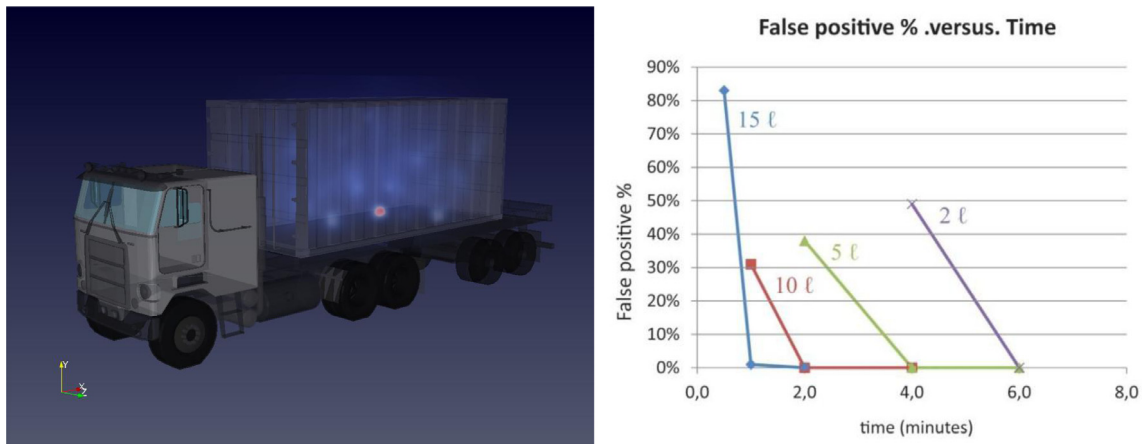


Fig. 24. Image obtained with a simulated portal for truck inspection (left); false positive rate versus the exposition time, for different volumes of lead (right).

Source: These figures are taken from Ref. [73].

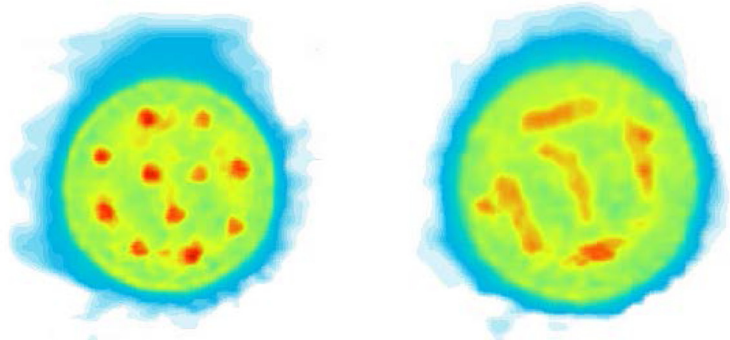
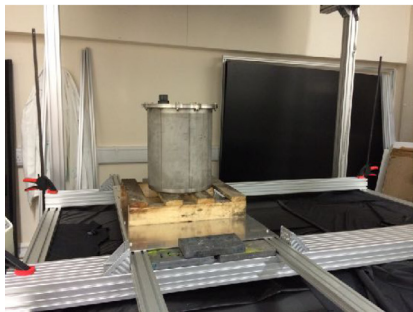


Fig. 25. From left to right: picture of the container inside the muon system. Horizontal slice (1 cm) in a region with tungsten pennies. Horizontal slice in a region with steel bars.

Source: Courtesy of R.Kaiser for Lynkeos Tech. LTD.

measurement of individual muons with reasonable precision to produce images of the interior. With a detector size of $5 \text{ m} \times 4 \text{ m}$ and a data acquisition time of 8 h, the simulation has shown that useful images can be obtained. In principle, such a long acquisition time could pose problems due to the burden displacement. However, it has been shown that it is possible to cancel the movement blur by using the data provided by the two detectors, that have a fixed position in space, as if they were moving synchronously with the burden.

5.3.3. Nuclear controls

An important field, with a lot of interest all over the world and several connected activities [170,171], is related to nuclear waste control and to the inspection of dry storage casks (DSC) for spent nuclear fuel (this item is extensively discussed in next subsection). The muon MCS tomography is a technology potentially adequate to identify and characterise nuclear materials stored in legacy waste containers. The presence of such containers is largely diffused all over the world so that the interest on this application is relevant. In general, it is required to identify high-Z materials in concrete-filled containers. Simulations [172,173] and measurements [174] have shown that the technique works. In addition, a muon imaging system from Lynkeos Technology LTD [175] has been installed at the National Nuclear Laboratory (Sellafield, UK). Images of a container with hidden metallic objects have been produced and the presence of tungsten pennies and steel bars is clearly visible, as shown in Fig. 25.

It is worth to mention here also the construction of a large drift-tube detector (two modules of $7.2 \text{ m} \times 7.2 \text{ m}$) planned to image the Fukushima Daiichi Nuclear Power Plant [46]. For reasons independent of technical aspects, the measurements in the nuclear facility were not done. On the other hand, the Tokyo Electric Power Company (TEPCO) has recently announced that its scanning efforts at Fukushima with cosmic-ray muons, even though using a radiographic method, was successful, and confirmed that nuclear plant's Reactor 1 suffered a complete meltdown following the earthquake and tsunami that struck Japan in 2011.

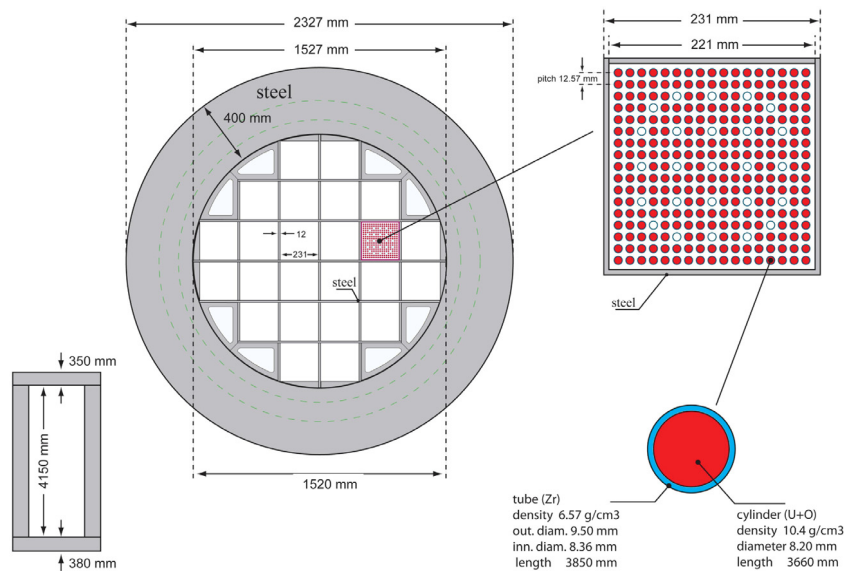


Fig. 26. Schematic view of cross sections of a CASTOR®V21. Details of a fuel assembly and of a single fuel rod are also given.

5.3.4. Historical building controls

A very interesting application regards non-destructive controls on the Florence cathedral, Santa Maria del Fiore [66]. The dome of the cathedral (*Cupola*), built in the 15th century, risks to crack under its own weight and hence activities are underway to model the structure before operating against further deterioration. According to some experts, the architect Filippo Brunelleschi might have built some reinforcement structures in the *Cupola* including iron chains inside the wall. Muon MCS tomography can be a technique to image iron substructures in the masonry, since the feasibility of the proposal has been demonstrated with measurements on a mock-up wall at the Los Alamos National Laboratory.

5.4. A detailed example: the inspection of dry storage casks

The storage of spent nuclear fuel is currently relying on transport and storage casks, in particular dry storage casks (DSC). Since spent nuclear fuel contains plutonium and uranium, the consequences of diversion of such nuclear material can be disastrous. The significant quantity (SQ) is the measure to evaluate such consequences and it corresponds to a quantity of nuclear material sufficient to produce a nuclear explosion. One DSC can contain up to 50 SQ's and in all EU there are more than 1500 DSC's (the number is rising continuously). DSC loaded with spent fuel will be stored for several decades in spent fuel storage facilities (SFSF). The safeguard is based on containment and surveillance methods, which assure the continuity of knowledge during the transfer of DSC from reactor to SFSF and during their long-term storage. Although this approach has proven to be very reliable, failures cannot be completely excluded over the long storage times and re-verification options are currently not satisfactory. Indeed, no validated methods to re-verify the content without opening the storage containers exist. Consequently, there is an urgent need to investigate techniques, which can provide a solution in terms of re-verification of a shielded spent fuel cask. Therefore, since muons are an excellent natural probe to study the content of dense and inaccessible volumes, muon tomography may constitute a very effective method to detect or exclude the presence of spent fuel assemblies. Typical DPCs are CASTOR® V casks with a typical height of about 5 m, an external diameter of 2.4 m and a mass of more than 120 tons when fully loaded. A schematic view of a CASTOR®V21 is presented in Fig. 26, where also the scheme of a single assembly is visible. This specific type is similar, in the geometrical arrangement of assemblies, to other types of casks. A pressurised water reactor (PWR) fuel assembly consists in a bundle of cylindrical rods (264 in the figure). Each rod is a Zircaloy tube of about 1 cm diameter, filled with pellets of uranium oxide ceramic.

Given the large amount of material present in DSC, both in its structure and in the stored spent fuel assemblies, the fraction of muons stopped inside the cask is not negligible. It is therefore possible to use simultaneously two techniques, based on different physical processes: the muon absorption rate and the MCS. As discussed above, a combined use of the two techniques can provide a map of the abundance of nuclei with different atomic numbers inside the cask.²

For all techniques, muon detectors should be placed around the container to measure position and direction, either of muons that enter, or of muons that exit from the cask. Based on this scheme, several studies on simulation data have

² An additional technique has been proposed [176]: the detection of neutrons from muon induced fission requiring to detect neutrons in coincidence with muons.

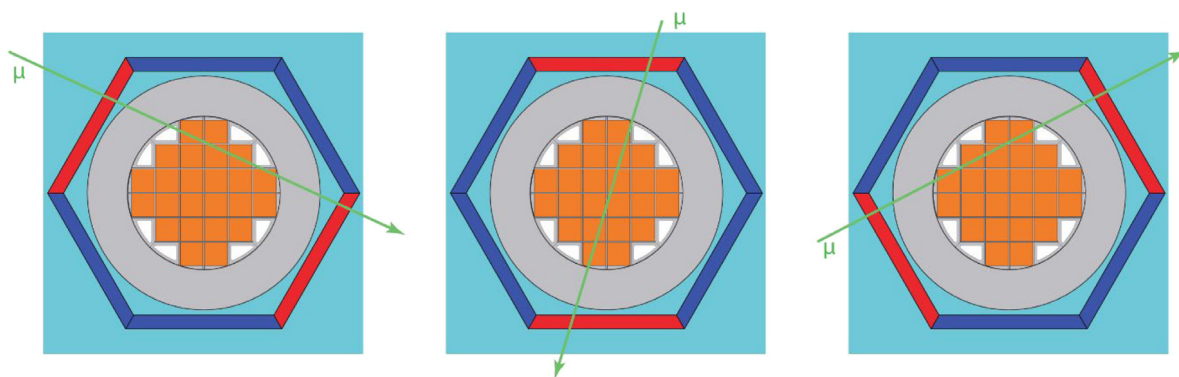


Fig. 27. Schematic view of a possible measurement of a CASTOR®V21 with a limited acceptance detector, represented by the red lines.

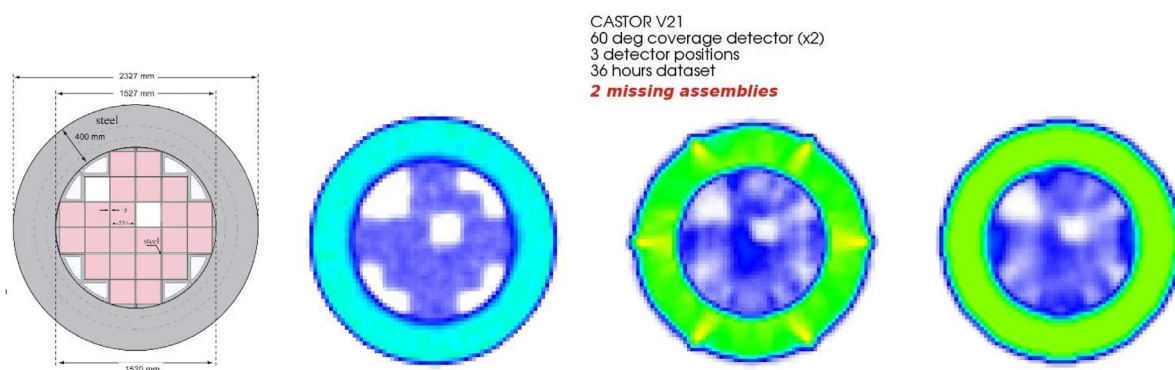


Fig. 28. From left to right: layout of a CASTOR®V21 with two missing assemblies used in the simulation. Reconstructed image obtained with a full coverage detector and simulated data equivalent to 12 h of cosmic muon collection. Reconstructed image obtained with a 1/3 coverage detector and 12 h of data taking in three positions as indicated in Fig. 27. The image obtained after fixing the SP of the cask structure to its known value.

shown that the technique should be able to recognise the absence of one or more assemblies from a cask. As reported in Ref. [171], with an ideal detector surrounding a cask, it should be possible to detect missing assemblies in less than two days of muon collection with a statistical precision of $\approx 18 \sigma$. In Ref. [177], the possibility to study the content of a CASTOR®V21 not only with a detector surrounding the cask, but also with a prototype detector with limited acceptance has been considered. Assuming to have only two modules out of six forming a surrounding detector of hexagonal shape, it has been supposed to rotate the modules as shown in Fig. 27.

Simulated data corresponding to 12 h of cosmic muons crossing a cask with two missing assemblies have been produced and analysed. The reconstruction of the cask content is based on the tomographic absorption/transmission method described above. The simulation shows that this technique can recognise the absence of fuel assemblies either with a full coverage detector or with a limited acceptance prototype, as shown in Fig. 28. The two rightmost images show that in presence of a reduced detector some artifacts can result from the limited acceptance at the detector borders and that it is possible to get rid of them by fixing the linear stopping power value of the cask structure.

It must be noticed, however, that the radioactivity escaping from the DSC walls constitutes a potential problem, given the low cosmic-ray rate. Nevertheless, two experimental tests have been performed in proximity of casks loaded with spent fuel. In the first test (2016) [178] two 1.2 m \times 1.2 m drift tube detectors were placed at the opposite sides of a Westinghouse MC-10 cask at the Idaho National Laboratory (US) as shown in Fig. 29.

In the second test (2018) [179] a small drift tube prototype 0.4 m \times 2 m was tested in proximity of a CASTOR® V19 in the interim storage facility of the EnKK nuclear power station at Neckarwestheim (Germany). In both cases muon tracks have been reconstructed reasonably well, demonstrating that the technique works even in presence of cask radioactivity (Fig. 30).

Data recorded in the American test have been taken in presence of a cask with several missing bars with respect to a fully loaded cask (Fig. 31). Measured scattering as a function of the position on the cask has been compared with GEANT4 simulations of a full and of an empty cask. As it can be seen in Fig. 31, the fourth column presents a single missing assembly. The corresponding average scattering is lower than what expected for a full cask by 2.3 standard deviations.



Fig. 29. Picture of the experimental setup with the two muon detectors on the opposite side of the cask.
Source: Courtesy of C. Morris.

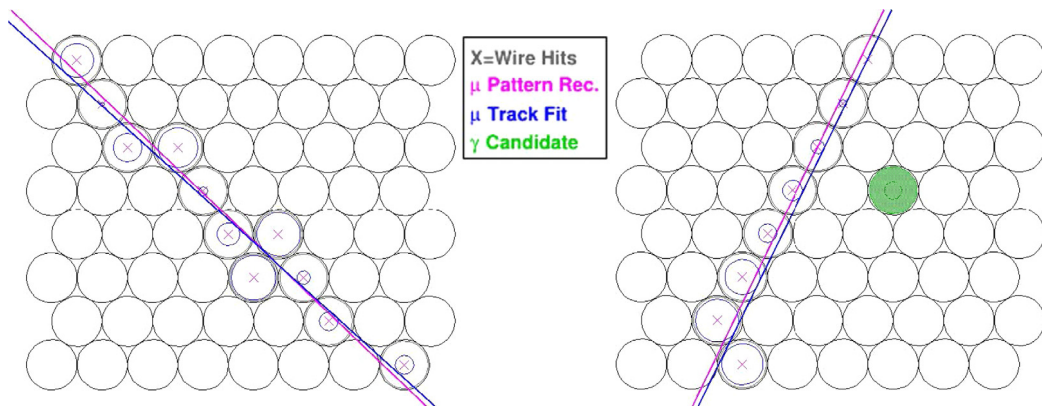


Fig. 30. Display of two reconstructed muon tracks, recorded with the detector positioned near the CASTOR®V19 [179]. The drift tubes are represented by black circles, the radial distances from the wires (pink crosses) corresponding to the measured drift time are shown as blue circles. A tube with a signal candidate to be produced by emitted radiation is represented by the green area.

In conclusion, several GEANT4 simulations show that it is possible to locate missing fuel assemblies with large confidence in a reasonable data taking time, and the first field tests indicate that using cosmic muons gives a potential tool for spent fuel casks re-verification.

6. Muon metrology

6.1. Introduction

In addition to radiography and tomography applications, cosmic muons have also been used for the track-based alignment of detectors, especially in high-energy physics (HEP) experiments, since decades. As discussed in Section 6.2, the idea is to use the parameters of the reconstructed tracks to estimate the position and orientation of all active detector elements. More recently, some authors have also investigated the possibility of using cosmic muons for the metrology of structures, such as an industrial press [5] and historical buildings [180–182]. This technique, named *muon metrology* in previous publications [70,183], is based on the assessment on how the relative alignment of a system of detectors, some integral to the structure of interest and the others to the surrounding environment, evolves over time. Changes in the alignment are then associated to movements or deformations of the structure. From a methodological point of view, this

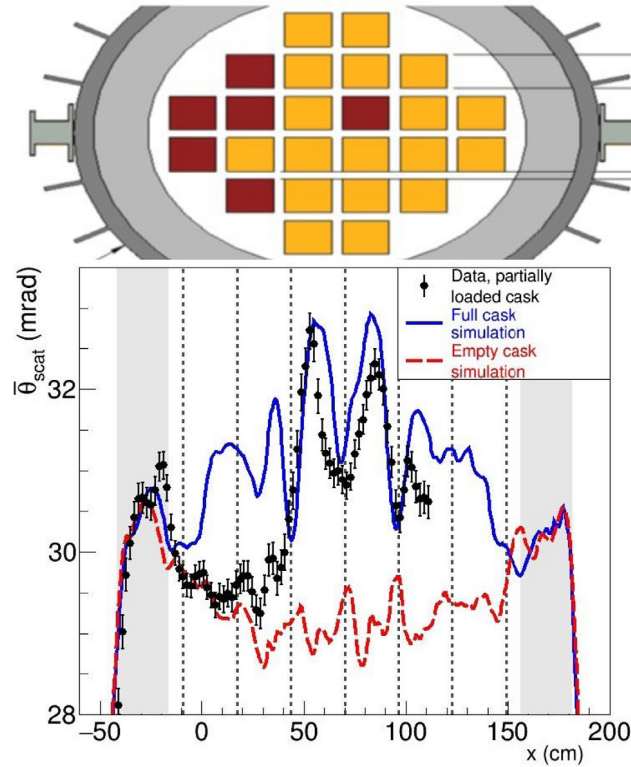


Fig. 31. Sketch of the cask filling (top panel: courtesy of C. Morris). Average scattering angle as a function of the position in the cask (bottom panel: taken from Ref. [178]). The grey areas and the dashed horizontal lines indicate the correspondence with the shielding volume and the fuel columns, respectively. Muon scattering simulations of a full and an empty cask are shown as well.

technique is basically a track-based alignment problem, even though an important difference is worth to be highlighted and it is discussed below.

In general, alignment procedures aim at providing a precise assessment of the alignment parameters, which specify the position and orientation of the different detectors of an experimental apparatus [184]. This leads to a better knowledge of the geometry of the system and, consequently, an improved track reconstruction (see Section 6.2). For the stability monitoring of structures, on the other hand, one is more interested in how the alignment parameters change over time than in their actual values. Differential measurements, which are generally less sensitive to several sources of systematic uncertainties compared to absolute ones, can thus be performed [180]. Moreover, the demands for the resolution, for this type of applications compared to those for detector alignments, are less severe, so that much less stringent requirements apply on the number of detectors, on their features and on the statistics to collect.

In Section 6.2 the use of cosmic muons for the alignment of tracking detectors is briefly discussed, whereas the focus of Section 6.3 is on its application for the metrology of structures, namely the stability monitoring of historical buildings.

6.2. Cosmic muons for the alignment of tracking detectors

The accurate reconstruction of the trajectories of charged particles (tracking) is an essential requirement for a wide range of physics topics. Indeed, large uncertainties on the estimated track parameters can have an impact, for example, on the particle identification, on the reconstruction of primary vertices, and on the momentum resolution of the tracks. These uncertainties are mainly due to the multiple scattering and the limited precision of the data recorded by the sensitive detector elements. In particular, the latter source of uncertainty is not only related to the resolution of the tracking detector, but also to the possible misalignment of its sensitive elements, as described below.

A charged particle, crossing a tracking detector, deposits energy in the sensitive elements of the detector, which results into a collection of position measurements. These measurements are usually *local*, meaning that they are computed with respect to a reference frame integral to the sensitive element they belong to. When reconstructing the particle trajectory, though, these measurements have to be located in space, so the relative position of all detector elements has to be known accurately. However, because of construction and assembly tolerances, of movements and deformations due to weight and variations of temperature or magnetic field, large differences between the design detector geometry and the one actually installed can occur. As a result, a bias on the measured positions is introduced, which translates in a degradation

of tracking performance. Therefore, a precise assessment of the alignment parameters, with a higher precision than the intrinsic detector resolution, is often a very important requirement. As alignment strategies based on lasers and cameras cannot usually cope with the requested accuracy, track-based alignment, described in the next section, is the most often used technique for high-precision tracking detectors.

6.2.1. Introduction to track-based alignment

This approach is based on the reconstruction of charged particle tracks, with a potentially misaligned detector, to infer the amount of misalignment. The biggest advantage of this technique is that it is sensitive to detector misalignment at levels smaller than the intrinsic detector resolutions. Tracks from different sources (and in different conditions) are usually used in track-based alignment, such as cosmic rays [185], beam-halo muons [186] and collision data [187].

From the mathematical point of view, most track-based algorithms for alignment are based on the minimisation of a χ^2 of the form:

$$\chi^2(\mathbf{a}, \boldsymbol{\tau}) = \sum_j \sum_i^{\text{tracks hits}} z_{ij}^2(\mathbf{a}, \boldsymbol{\tau}_j), \quad (52)$$

where

$$z_{ij}(\mathbf{a}, \boldsymbol{\tau}_j) = \frac{r_{ij}(\mathbf{a}, \boldsymbol{\tau}_j)}{\sigma_{ij}} = \frac{m_{ij} - u_{ij}(\mathbf{a}, \boldsymbol{\tau}_j)}{\sigma_{ij}} \quad (53)$$

is the normalised residual between the predicted hit location from the track model u_{ij} and the actual measurement m_{ij} . In general, the residual r depends of the track parameters $\boldsymbol{\tau}$ and of the alignment parameters \mathbf{a} , containing all degrees of freedom of the alignable elements.

Different approaches for the minimisation of the χ^2 in Eq. (52) have been proposed. Some of the most popular algorithms (especially in HEP) are:

- **Hits and Impact Points (HIP) algorithm** — It is an iterative algorithm which, independently for all alignable elements, minimises a *local* χ^2 function with fixed track parameters. After each pass over the data sample, the alignment parameters are computed and the tracks are refitted with the new alignment scenario [188]. These alignment and refitting steps are iterated until no statistically significant changes in the alignment parameters are obtained. The HIP algorithm is a local χ^2 method, that is correlations between different detector elements are neglected: each module is aligned assuming all the others are fixed. This approximation makes the algorithm computationally very light, as only a 6×6 matrix inversion is required for each alignable element.
- **Kalman Filter (KF) algorithm** — Like the HIP algorithm, also this method belongs to the family of the iterative algorithms. Based on the Kalman Filter [189], its main idea consists of a sequential update of the alignment parameters after each track [190]. This method performs a global alignment, even though, in presence of a large number of alignable elements, the update is usually limited to those elements with large correlations with the ones actually crossed by the track. This approach avoids the inversion of large matrices, but requires the bookkeeping of the correlations between the alignable modules.
- **Millepede algorithm** — It is a non-iterative linear least squares algorithm, which does a simultaneous minimisation of the χ^2 function with respect to both alignment and track parameters, preserving all correlations [191]. This approach will be described in more detail in Section 6.2.2

A major problem arising from track-based alignment is related to the so-called *weak modes*. They originate from coherent detector misalignments which leave the overall χ^2 (almost) unchanged. As a consequence, detector displacements producing weak modes cannot be detected by the track-based alignment. Two categories of weak modes are identified. The first one corresponds to global translations and rotations of the entire detector to be aligned, as those degrees of freedom are unconstrained by tracks reconstructed with the detector itself alone. The second category corresponds to coherent detector deformations that leave the χ^2 unchanged by biasing the reconstructed track parameters. Examples are elliptical distortions and twists in cylindrically symmetric detectors. Moreover, weak modes are related to the type of tracks used for the alignment. For example, for predominantly vertical cosmic tracks, shifts of all modules in the vertical direction constitutes a weak mode, which is not the case for collision data, though. Weak modes can be handled in few ways, such as adding external constraints in addition to the track quality, or using tracks from events with different topologies.

6.2.2. The Millepede and Millepede II algorithms

Millepede is a well established algorithm, which was originally developed for the alignment of the H1 experiment and later successfully used in many other HEP experiments, such as CDF, LHCb, CMS and others [184]. It is a fast and non-iterative linear least squares algorithm, which can take into account correlations between the alignment parameters. In this least squares fit problem, the alignment parameters are *global* parameters, as they are not specific to individual tracks or events, whereas the parameters of the individual tracks are *local* parameters.

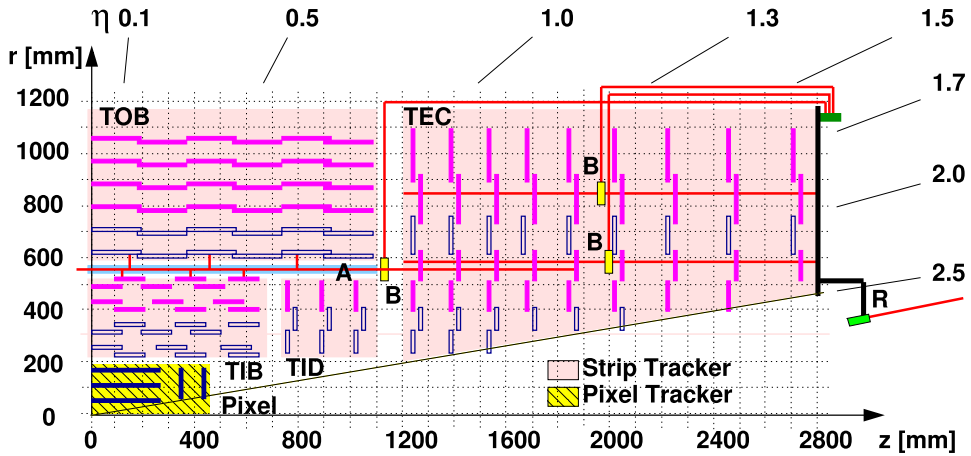


Fig. 32. Schematic view of one quarter of the CMS tracker [198].

The algorithm performs a linearisation of the χ^2 minimisation problem, by linearising the normalised residuals in Eq. (52) [192]:

$$\chi^2(\mathbf{a}, \boldsymbol{\tau}) = \sum_j \sum_i^{\text{tracks hits}} \frac{1}{\sigma_i^2} \left(m_{ij} - u_{ij}(\mathbf{a}_0, \boldsymbol{\tau}_{0,j}) + \frac{\partial r_{ij}}{\partial \mathbf{a}} \delta \mathbf{a} + \frac{\partial r_{ij}}{\partial \boldsymbol{\tau}_j} \delta \boldsymbol{\tau}_j \right)^2. \quad (54)$$

This is done around some initial values \mathbf{a}_0 and $\boldsymbol{\tau}_0$ of the alignment parameters and track parameters, respectively. The minimisation of the χ^2 function in Eq. (54) leads to a system of linear equations, whose solution would require the inversion of an extremely large matrix, as the number of the track parameters, depending on the size of the data sample, could be of the order of millions. Thanks to the fact that individual tracks are independent of each other, except for using the same detector geometry, this matrix has a special structure, which can be exploited to reduce its size: the χ^2 minimisation problem can be reduced to the inversion of a $n \times n$ matrix, \mathbf{C}' [193], where n is the number of the alignment parameters. This matrix size reduction is the core idea of the Millepede algorithm.

As the CPU time necessary to invert a $n \times n$ matrix is proportional to n^3 , the method becomes inapplicable if the number the alignment parameters is very large ($\gg 10^4$). This is, for example, the case of the alignment of the CMS tracker (see Section 6.2.3), as the number of the alignment parameters to be determined is up to 200000 [187]. For this reason a new version of the Millepede algorithm, called Millepede II, has been developed [184]. The idea is to take advantage of some techniques to solve linear equations, which are not based on the inversion of matrices [194]. They only require products of matrices with vectors, which are generally very fast for sparse matrices, which is usually the case of \mathbf{C}' [195]. Some of these fast methods are implemented in Millepede II.

In the next section, the alignment of the tracker of the CMS experiment, as an illustrative example of the use of cosmic muons for this type of metrology application, is presented.

6.2.3. Alignment of the CMS tracker with cosmic muons

The scientific goals of the Compact Muon Solenoid (CMS) experiment [79] apply strong constraints on the required tracking performance. The CMS silicon tracking detector (tracker) [196,197] consists of six sub-detectors, as shown in Fig. 32: pixel modules are arranged into the barrel pixel (BPIX) and the forward pixel (FPX); strip modules, in the central region, are arranged into the tracker inner barrel (TIB) and the tracker outer barrel (TOB); similarly, strip modules in the end-cap regions are arranged in the tracker inner disks (TID) and tracker end-caps (TEC).

The CMS tracker has been designed to measure the trajectories of charged particles with very high momentum, angle, and position resolutions. Indeed, design specifications require a resolution, on the transverse momentum, from 1.5% for 100 GeV/c momentum muons up to 10% for 1000 GeV/c ones [199].

Misalignment is one of the most limiting factors for the tracker performance: for example, misalignment at the level of only few tens of μm can seriously affect the bottom-tagging performance [200]. As the intrinsic hit position resolution is between 10 and 30 μm , an alignment precision better than 10 μm is requested in order to achieve optimal track parameter resolution. Such a precision can only be reached with track-based alignment, using tracks from different sources, such as cosmic muons and collision data.

CMS started to collect cosmic ray data, for testing and calibration purposes, in the commissioning phase of the experiment. The first long and dedicated run for cosmic muons, known as *cosmic run at four Tesla* (CRAFT) [201], was performed during October and November 2008, using the magnetic field at the nominal value (3.8 T). Approximately 200

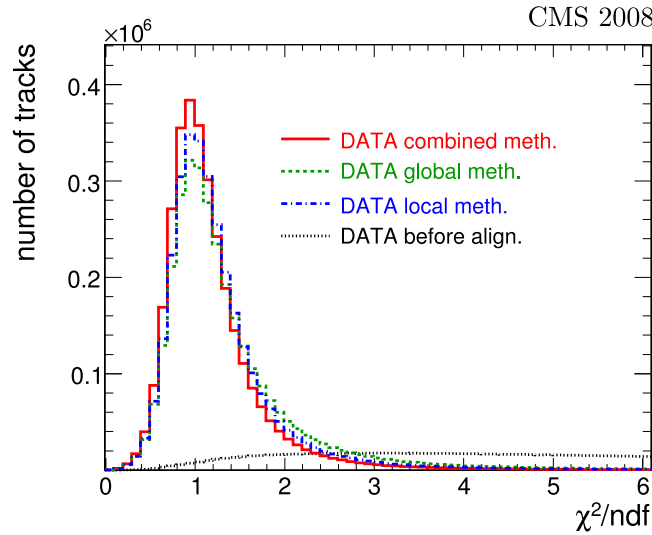


Fig. 33. χ^2/ndf distribution of the tracks before the alignment and after the alignment with the local (HIP), global (Millepede II), and combined methods [198].

Table 2

RMS of the DMR. Results from the global, local and combined methods are reported, as well as the values before any alignment (first column). For comparison, also simulation results, based on the combined method and ideal geometries, are shown. Finally the last column reports, for each detector subsystem, the number of modules, with more than 30 hits, used in the alignment procedure [198].

	Before [μm]	Global [μm]	Local [μm]	Combined [μm]	Combined MC [μm]	Ideal MC [μm]	Modules > 30 hits
BPIX (u')	328.7	7.5	3.0	2.6	2.1	2.1	757/768
BPIX (v')	274.1	6.9	13.4	4.0	2.5	2.4	757/768
FPIX (u')	389.0	23.5	26.5	13.1	12.0	9.4	393/672
FPIX (v')	385.8	20.0	23.9	13.9	11.6	9.3	393/672
TIB (u')	712.2	4.9	7.1	2.5	1.2	1.1	2623/2724
TOB (u')	168.6	5.7	3.5	2.6	1.4	1.1	5129/5208
TID (u')	295.0	7.0	6.9	3.3	2.4	1.6	807/816
TEC (u')	216.9	25.0	10.4	7.4	4.6	2.5	6318/6400

million tracks were recorded, which were used to align and calibrate the various sub-detectors. In the following, a brief description of the alignment of the CMS tracker with CRAFT data is presented.

Two different methods were used: a global approach, based on Millepede II (see Section 6.2.2), and a local one, based on HIP (see Section 6.2.1). The two techniques were also combined (combined method) to improve the results: the alignment parameters were initially determined from the global algorithm and then used as starting point for the local one, whose alignment strategy was modified to exploit the already good knowledge of the alignment parameters used as input [198]. Several quantities were monitored to validate the results, such as the residuals and the χ^2/ndf of the tracks, used in the χ^2 minimisation, and the track parameter resolutions. Fig. 33 shows the distribution of χ^2/ndf of the tracks before and after the alignment with the global, local and combined methods.

From the distribution of the hit residuals, in each module, the median was taken and histogrammed for all modules in a detector subsystem. Only modules with more than 30 recorded hits were considered. The resulting distribution of the medians of residuals (DMR) was used as a measure of the alignment accuracy [187,198]. Results, using ~ 3.2 million reconstructed cosmic muons, are summarised in Table 2. The alignment accuracy, as measured by the RMS of the DMR, was found to be in the range between 3–4 μm in the barrel and between 3–14 μm in the end-caps, using the combined method. The worse resolution in the end-caps was mainly related to the limited number of tracks in the forward regions.

The quality of the tracker alignment was not only statistically but also systematically limited. Indeed, in general, the lack of different track types makes more likely that some detector deformations result into weak modes (see Section 6.2.1), which the alignment procedure is not sensitive to. For this reason, with the first $p-p$ collision data at LHC, CMS started to include them in the alignment procedure, in order to achieve the best possible accuracy [187].

6.3. The stability monitoring of historical buildings with cosmic muons

The use of a somehow analogous technique to the track-based alignment, previously described, has been recently investigated by some authors in a completely different scenario: the stability monitoring of large structures. In this

context, a feasibility study for the monitoring of the structural alignment of a mechanical press was published in 2007 [5]. In this study, based on MC simulations, an ideal tracking detector, consisting of three 400 cm² sensitive layers, mechanically connected to the press, was used to assess relative changes in position between different parts of the structure. Results, based on a number of reconstructed muons corresponding to 1 week of data taking, showed that a performance comparable to those obtainable with standard alignment methods (such as laser scanners, theodolites, etc.) could be achieved.

A major problem for many applications, based on the use of cosmic muons, is the limited rate of muons at the Earth's surface, which is approximately 170 Hz/m². As a result, long data takings could be necessary to collect enough statistics for the set goal, and this could be a strong limiting factor in the use of the technique, especially outside of the research domain. However, for applications such as the static monitoring of historical buildings, data takings of the order of few days (or even few weeks) could not be a problem, as typical structural deformations evolve over a very long period of time. Moreover, for historical buildings, strong constraints apply on the invasiveness of the monitoring technique to be used, because of their cultural and artistic value, and this could prevent the use of some standard monitoring systems.

For these reasons, recently the possibility of using cosmic muons for the stability monitoring of historical buildings [180] has been investigated, using the vaulted roof of the *Palazzo della Loggia*, in the town of Brescia (Italy), as a benchmark case. The general idea is that, given a set of tracking detectors, some of them integral to the structure of interest and the others to the surrounding environment, relative changes in their alignment over time can be used to assess the structural modifications of the whole building. For this study, based on MC simulations, the authors considered a simpler scenario, based on a system of 2 tracking detectors, consisting of three 400 × 400 mm² sensitive elements each. All tracking elements are composed of two orthogonal layers, made of 3 × 3 mm² scintillating fibres. Three different configurations were considered, with the detectors being separated by 350 cm, 880 cm and 1300 cm, respectively. In all cases, an interposing material, consisting of a 15 cm thick wooden layer (simulating the ceiling of the *Salone Vanvitelliano* within *Palazzo della Loggia*), was present between the detectors.

6.3.1. The method

As already discussed, the idea of the method is to measure changes in the relative position between the two detectors, by means of reconstructed cosmic muons. As muons are highly penetrating particles, this technique can be used even in presence of interposing material between the detector, as it is the case of *Palazzo della Loggia*. However, when a charged particle traverses a medium, it is deflected by many small-angle scatters (multiple Coulomb scattering), as described in Section 2.2. Because of the central limit theorem, for many small-angle scatters the net angular and spatial deflections are (approximately) Gaussian-distributed random variables [13]. The expected mean values for both the angular and spatial deflections are zero. In order to reduce the impact of the multiple Coulomb scattering, a minimum χ^2 estimation method, independently applied to both $x - z$ and $y - z$ views, was implemented.

Considering, for example, the $x - z$ view of a xyz reference frame integral to the lower detector, being z the vertical coordinate, the relative position of the higher detector with respect to the lower one is fully described by the spatial variable x_D and the angular variable θ_D . A muon, crossing the entire detection system, is independently reconstructed in the two telescopes and the reconstructed tracks are extrapolated to a common plane. The differences between the position of the extrapolated tracks at the common plane ($x'_h - x'_l$) and the track directions ($\theta_h - \theta_l$) are then computed. As, in general, a roto-translation of one detector with respect to the other determines non-zero expected values for these residuals, the estimation of parameter of interest x_D and θ_D can be obtained from a minimum χ^2 estimation method, using the following χ^2 definition:

$$\chi^2 = \sum_i \left[\frac{(x'_{h,i} - x'_{l,i})^2}{\sigma_{x'_{h,i}}^2 + \sigma_{x'_{l,i}}^2} + \frac{(\theta_{h,i} - \theta_{l,i})^2}{\sigma_{\theta_{h,i}}^2 + \sigma_{\theta_{l,i}}^2} \right], \quad (55)$$

where $\sigma_{x'}$ and σ_{θ} are respectively the errors on the reconstructed x' and θ respectively, the subscripts h and l refer to the higher and lower detectors, and the i index runs over all the reconstructed muons in the data sample. Finally, it is worth to mention that the use of this technique could also be extended to the monitoring of other large vertical structures, such as dams, pillars and bridges, even though no literature on this subject is available at the time of writing this review.

6.3.2. Results

The χ^2 minimisation, described above, provides an estimation of x_D and θ_D from the reconstruction of a sample of cosmic muons, whose size affects the statistical accuracy of the estimation. For a given sample size, the estimation was repeated many times (on new samples) to assess the resolution on the parameters of interest. Of course, the expected time of data taking to collect the same statistics changes among the three configurations, because of the different geometrical acceptances. Expected rates for the $\Delta z(350 \text{ cm})$, $\Delta z(880 \text{ cm})$ and $\Delta z(1300 \text{ cm})$ configurations are (approximately) 6.0 muons/min, 1.1 muons/min and 0.5 muons/min, respectively.

Resolutions on the parameters of interest, x_D and θ_D , are shown in Fig. 34, where systematic uncertainties related to geometrical tolerances in the detectors and to their relative positioning were taken into account. The results show that, even in the most challenging scenario with $\Delta z(1300 \text{ cm})$, accuracies on the relative position between the two telescopes can be of the order of 1 mm with few days of data takings. Performance is found to be comparable to those of other monitoring systems, with few potentially appealing features, such as the applicability also in presence of interposing structures and the limited invasiveness.

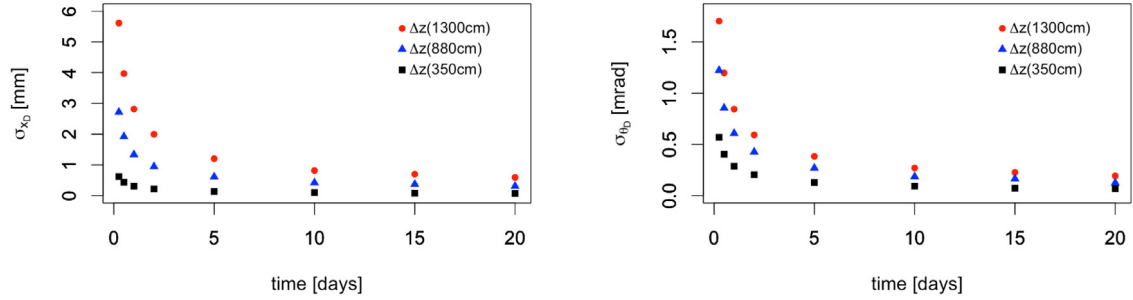


Fig. 34. Resolution on x_D (left) and θ_D (right) as a function of data taking time, for the three different configurations: ● $\Delta z(1300\text{ cm})$, ▲ $\Delta z(880\text{ cm})$ and ■ $\Delta z(350\text{ cm})$ [180].

7. Summary and conclusions

Since their discovery a century ago, cosmic-ray muons have been helpful to advance our knowledge of Nature. Indeed they were used as probes to discover many new particles and have been used to calibrate detectors and experimental apparatus in nuclear and particle physics. In the last decades, they have been also employed to develop applications in various fields. In the present review, such applications have been classified into three main categories: *muon radiography*, *muon tomography* and *muon metrology*. The nomenclature is somehow arbitrary since other authors have used different ways to refer to these new techniques, especially for muon radiography and muon tomography. For this reason, throughout the article, other synonymous have been used. In particular muon radiography has been also called *muon absorption radiography* and *muography*, while muon tomography has also been cited as *muon MCS tomography*, where MCS stands for Multiple Coulomb Scattering. The main difference between the two techniques is that the first one counts the number of muons crossing a given structure, while the second one relies on the measurement of the deflection of the particle and for this reason needs detectors at two sides of the object under study.

In this review, after an introduction about the origin of cosmic rays in Section 1 and their interaction with matter in Section 2, an overview of the main detectors used in cosmic-ray applications (nuclear emulsions, scintillators, and gas detectors) has been presented in Section 3. In Section 4, the basic principles of muon radiography have been summarised. In particular, data analysis techniques to extract information on the structure under investigation, such as the density distribution, relative transmission and 3D imaging, have been presented and described. Such techniques are now used in many research areas such as in volcanology, archeology, civil engineering and for industrial applications. The studies of big structures, such as pyramids and volcanoes, if we exclude the pioneer experiment of E. P. George in 1955, have been historically the first ones to be introduced. On the other hand, mineral exploration, monitoring of carbon dioxide geostorages, bedrock profiling, hydrological and geophysical measurements, archeological surveys and industrial applications are now being developed and they promise important results in the near future. For what concerns muon tomography, it has been presented and described in Section 5. Through the measurement of the deflection of muons crossing the object under study, 3D images can be reconstructed. To perform such reconstructions a sophisticated algorithm needs to be used, as described in Section 5.1. Applications of muon tomography are mainly concentrated in the fields of safeguards, nuclear security and safety, controls of transport, such as containers and trucks, for the detection of illicit or dangerous materials (for example radioactive and nuclear materials), and in the field of nuclear energy (for example for the inspection of dry storage casks). In particular DecisionScience, a spin-off of the Los Alamos National Laboratory, has been able to overcome the research stage and is now on the market with a full portal for the inspection of trucks at borders and ports. Also industrial applications are now under study for the inspection of large structures such as blast furnaces. In the end, in Section 6, also muon metrology has been presented and described. Cosmic-ray muons have been used for many decades to align detectors, in experiments at CERN and in other laboratories around the world. Recently it has been suggested to use the same technique for civil applications such as the stability monitoring of vertical structures. A detailed example for historical buildings has been presented in Section 6.3.

There are many advantages in the use of cosmic-ray muons in several applications, as pointed out throughout the review. Summarising: they rely on a natural and continuous radiation source, so that no radiological risks are present; they can count on very well known detectors, used since many decades in experiments in nuclear and particle physics; in many cases, given the capability of the muons to cross big volumes of materials, there are no other technologies that can be used. Concerning the limitations, an intrinsic boundary is the fact that the muon flux is limited by Nature. The precision of the measurements depends on the available statistics. In other words, cosmic-ray muon applications are not suitable where measurements need to be done in seconds or in many cases even minutes or hours. They can be applied only to static or *quasi static* situations. On the other hand, waiting the appropriate time and with specific detector and reconstruction techniques, systems based on muon radiography or tomography can be efficiently used. This field of research, even if it is a relatively recent one, is evolving rapidly and we believe that there is room for improvement and refinement of present and past applications, and for the development of new ones that, in the long term, can have an impact on our daily life.

References

- [1] L.W. Alvarez, et al., *Science* 167 (1970) 832.
- [2] E.P. George, *Commonw. Eng.* 455 (1955).
- [3] K. Nagamine, et al., *Nucl. Instrum. Methods A* 356 (1995) 585.
- [4] K.R. Borozdin, et al., *Nature* 422 (2003) 277.
- [5] I. Bodini, et al., *Meas. Sci. Technol.* 18 (2007) 3537.
- [6] D. Pacini, *Nuovo Cimento VI-3* (1912) 93–100.
- [7] V.F. Hess, *Phys. Z.* 13 (1912) 1084–1091.
- [8] C.D. Anderson, *Phys. Rev.* 43 (1933) 491.
- [9] C.D. Anderson, S.H. Neddermeyer, *Phys. Rev.* 50 (1936) 263.
- [10] C.M.G. Lattes, G.P.S. Occhialini, C.F. Powell, *Nature* 160 (1947) 453.
- [11] G.D. Rochester, C.C. Butler, *Nature* 160 (1947) 855.
- [12] V.D. Hopper, S. Biswas, *Phys. Rev.* 80 (1950) 1099.
- [13] M. Tanabashi, et al., (Particle Data Group), *Phys. Rev. D* 98 (2018) 030001.
- [14] L. Bonechi, et al., *Proceedings of the 29th International Cosmic Ray Conference*, 2005, pp. 101–104.
- [15] W.R. Leo, *Techniques for Nuclear and Particle Physics Experiments*, Springer Berlin Heidelberg, ISBN: 978-3-642-57920-2, 1994, pp. 17–68.
- [16] H.A. Bethe, *Ann. Phys.* 397 (1930) 325.
- [17] D.E. Groom, N.V. Mokhov, S. Striganov, *At. Data Nucl. Data Tables* 76–2 (2001) 1.
- [18] J. Beringer, et al., (Particle Data Group), *Phys. Rev. D* 86 (2012) 010001.
- [19] H.A. Bethe, *Phys. Rev.* 89 (1953) 1256.
- [20] W.T. Scott, *Rev. Mod. Phys.* 35 (1963) 231.
- [21] W. Motz, H. Olsen, H.W. Koch, *Rev. Mod. Phys.* 36 (1964) 881.
- [22] G.R. Lynch, O.I. Dahl, *Nucl. Instrum. Methods B* 58 (1991) 6.
- [23] S. Agostinelli, et al., *Nucl. Instrum. Methods A* 506 (2003) 250.
- [24] R.S. Fletcher, et al., *Phys. Rev. D* 50 (1994) 5710;
J. E-Ahn, R. Engel, T.K. Gaisser, P. Lipari, T. Stanev, FERMILAB-PUB-09-304-A (arXiv:0906.4113v3 [hep-ph]).
- [25] C. Hagmann, D. Lange, D. Wright, *2007 IEEE Nuclear Science Symposium Conference Record*, 2007, pp. N24–36.
- [26] G. Battistoni, et al., *Proceedings of the 31st International Cosmic Ray Conference*, 2009.
- [27] M. Bazzotti, et al., *Proceedings of the 31st International Cosmic Ray Conference*, 2009.
- [28] P. Biallass, T. Hebbeker, arXiv:0907.5514v1 [astro-ph.IM].
- [29] X. Yue, et al., *Nuclear Science Symposium and Medical Imaging Conference (NSS/MIC)*, IEEE, 2012.
- [30] P. Baesso, et al., *JINST* 8 (2013) P08006.
- [31] S. Riggi, et al., *J. Phys.: Conf. Ser.* 409 (2013) 012046.
- [32] P. Baesso, et al., *JINST* 9 (2014) C10041.
- [33] G.V. Russo, et al., *JINST* 9 (2014) P11008.
- [34] J. Marteau, et al., *Meas. Sci. Tech.* 25 (2014) 035101.
- [35] S. Xiang, et al., *Proceedings of the 19th IEEE-NPSS Real Time Conference*, 2014, pp. 1–6.
- [36] M. Biglietti, *Proceedings of the Technology and Instrumentation in Particle Physics Conference (PoS TIPP2014)*, 2014, p. 290.
- [37] L.G. Dedenko, et al., *Bull. Lebedev Phys. Inst.* 41 (8) (2014) 235.
- [38] X. Wang, et al., *Nucl. Instrum. Methods A* 784 (2015) 390.
- [39] P. La Rocca, et al., *Nucl. Instrum. Methods A* 787 (2015) 236.
- [40] A.B. Aleksandrov, et al., *Phys. Part. Nuclei Lett.* 12 (2015) 713.
- [41] F. Riggi, et al., *EPJ Web Conf.* 117 (2016) 05003.
- [42] D. Varga, et al., arXiv:1607.08494, 2016.
- [43] J. Burns, et al., *JINST* 10 (2015) P10041.
- [44] H.K.M. Tanaka, et al., *Earth Planet. Sci. Lett.* 306 (2011) 156.
- [45] A.A. Borisov, et al., *Instrum. Exp. Tech.* 55 (2) (2012) 151.
- [46] M. Kume, et al., *JINST* 11 (2016) P9008.
- [47] M. Del Santo, et al., *Nucl. Instrum. Methods A* 876 (2017) 111–114.
- [48] C.F. Powell, et al., *G. Sci. Instrum.* 23 (1946) 102.
- [49] S. Aoki, et al., *Nucl. Instrum. Methods B* 51 (1990) (1990) 466–472.
- [50] H.K.M. Tanaka, et al., *Nucl. Instrum. Methods A* 575 (2007) 489–497.
- [51] A. Alexandrov, G. De Lellis, V. Tioukov, *Sci. Rep.* 9 (2870) (2019) 1–10.
- [52] H.K.M. Tanaka, et al., *Nucl. Instrum. Methods A* 507 (2003) 657–669.
- [53] D. Carbone, et al., *Geophys. J. Int.* 196 (2014) 633–643.
- [54] A. Anastasio, et al., *Nucl. Instrum. Methods A* 732 (2013) 423–426.
- [55] A. Anastasio, et al., *Nucl. Instrum. Methods A* 718 (2013) 134–137.
- [56] G. Saracino, et al., *Ann. Geophys.* 60 (2017) 1–6.
- [57] G. Baccani, et al., *JINST* 13 (2018) P11001.
- [58] A. Pla-Dalmau, A.D. Bross, V.V. Rykalin, *Proceedings of the IEEE Nucl. Sci. Symp.*, 2003.
- [59] V. Antonuccio, et al., *Proceedings of the IEEE Nucl. Sci. Symp.*, 2013.
- [60] L. Consiglio, et al., *JINST* 14 (2019) P01014.
- [61] M. Basset, et al., *Nucl. Instrum. Methods A* 567 (2006) 298–301.
- [62] M. Menichelli, et al., *Nucl. Instrum. Methods A* 567 262–265.
- [63] J. Gluyas, et al., *Phil. Trans. R. Soc. A* 377 (2018) 2137.
- [64] A. Bonneville, et al., *Phil. Trans. R. Soc. A* 377 (2018) 2137.
- [65] J. Flygare, et al., *IEEE Transactions on Nuclear Science* 65 2724–2731.
- [66] E. Guardincerri, et al., *Phil. Trans. R. Soc. A* 377 (2018) 2137.
- [67] C. Cârloganu, *2011 Europhysics Conference on High Energy Physics-HEP*, 2011.
- [68] C. Cârloganu, et al., *Geosci. Instrum. Methods Data Syst.* 2 (2013) 55–60.
- [69] L. Oláh, et al., *Sci. Rep.* 8 (2018) 3207.
- [70] S. Bouteille, et al., *Nucl. Instrum. Methods A* 834 (2016) 223.
- [71] Z. Luo, et al., *IEEE Nucl. Sci. Symp. and Medical Imaging Conference*, 2013.
- [72] K. Gnanvo, et al., arXiv:1011.3231, 2010.

- [73] Mu Steel project, Research Fund for Coal and Steel RFSR-CT-2010-00033 final report available from: https://ec.europa.eu/research/industrial_technologies/pdf/rfcs/summaries-rfcs_en.pdf.
- [74] Mublast project, Research found for coal and steel RFSR-CT-2014-00027 available from: https://ec.europa.eu/research/industrial_technologies/pdf/rfcs/summaries-rfcs_en.pdf.
- [75] S. Vanini, et al., Phil. Trans. R. Soc. A 377 20180051.
- [76] V. Anghel, et al., Nucl. Instrum. Methods A 789 (2015) 12.
- [77] S. Pesente, et al., Nucl. Instrum. Methods A 604 (2009) 738.
- [78] P. Checchia, et al., Phil. Trans. R. Soc. A 377 (2018) 20180065.
- [79] The CMS collaboration, J. Instrum. 3 08 (2008) S08004.
- [80] <http://mutomweb.pd.infn.it:5210/>.
- [81] A. Lechmann, et al., Solid Earth 9 (2018) 1517–1533.
- [82] O. Catalano, et al., Nucl. Instrum. Methods A 807 (2016) 5–12.
- [83] W. Lohmann, E. Kopp, R. Voss, CERN 85-03 experimental physics division, 1985.
- [84] N. Lesparre, et al., Geophys. J. Int. 183 (2010) 1348–1361.
- [85] T. Gaisser, T. Stanev, Phys. Lett. B 667 (2008) 254–260.
- [86] D. Heck, et al., Forschungszentrum Karlsruhe Report FZKA, Vol. 6019, Karlsruhe University, 1998.
- [87] M. Guan, et al., arXiv:1509.06176, 2015.
- [88] T. Hebbeker, C. Timmermans, Astropart. Phys. 18 (2002) 107–127.
- [89] G. Saracino, et al., Sci. Rep. 7 (2017) 1181.
- [90] G. Saracino, et al., Phil. Trans. R. Soc. A 377 (2018) 2137.
- [91] L. Cimmino, et al., Sci. Rep. 9 (2019) 2974.
- [92] R. Nishiyama, S. Miyamoto, N. Naganawa, Geosci. Instrum. Methods Data Syst. 3 (2014) 29–39.
- [93] A. Tarantola, et al., Rev. Geophys. Space Phys. 20 (2) (1982) 219.
- [94] H.K.M. Tanaka, Solid Earth 115 (2010).
- [95] H.K.M. Tanaka, et al., Geophys. Res. Lett. 34 (2007).
- [96] N. Lesparre, J. Cabrera, J. Marteau Geophys. J. Int. 208 (2016) 1579–1591.
- [97] D. Bryman, Society of Economic Geologists, Vol. 18, Inc. Special Publication, 2014, pp. 235–241.
- [98] D. Bryman, J. Bueno, J. Jansen, 24th International Geophysical Conference and Exhibition, 2015.
- [99] D. Schouten, P. Ledru, JGR: Solid Earth 123 (2018) 8637–8652.
- [100] D. Schouten, Phil. Trans. R. Soc. A 377 (2018) 2137.
- [101] K. Davis, D.W. Oldenburg, ASEG Extended Abstracts 2012: 22nd Geophysical Conference, 2012, pp. 1–4.
- [102] K. Jourde, D. Gibert, J. Marteau, Geosci. Instrum. Methods Data Syst. 4 (2015) 177–188.
- [103] M. Rosas-Carbajal, et al., Geophys. Res. Lett. 44 (2017) 6743–6751.
- [104] P.G. Lelièvre, et al., Geophys. J. Int. 218 (2019) 1685–1701.
- [105] L. Bonechi, et al., J. Instrum. 10 (2015) P02003.
- [106] L. Bonechi, et al., Phil. Trans. R. Soc. A 377 (2018) 2137.
- [107] R. Nishiyama, et al., Geophys. J. Int. 206 (2016) 1039–1050.
- [108] H.K.M. Tanaka, et al., Hyperfine Interact. 138 (2001) 521–526.
- [109] K. Nagamine, et al., Nucl. Instrum. Methods A 356 (1995) 585–595.
- [110] D. Lo Presti, et al., Sensors 19 (2019) 1183.
- [111] H.K.M. Tanaka, et al., Geophys. Res. Lett. 36 (2009) L01304.
- [112] H. Shinohara, H.K.M. Tanaka, Earth Planet. Sci. Lett. 349–350 (2012) 87–97.
- [113] K. Jourde, et al., arXiv:1307.6758v1 [physics.ins-det], 2013.
- [114] N. Lesparre, et al., Geosci. Instrum. Methods Data Syst. 1 (2013) 33–42.
- [115] M. De Serio, et al., Nucl. Instrum. Methods A 512 (2003) 539–545.
- [116] F. Ambrosino, et al., Solid Earth 120 (2015) 7290–7307.
- [117] H. Gómez, et al., J. Instrum. 12 (2017) P12018, 1–15.
- [118] V. Neiss, et al., Comput. Phys. Comm. 229 (2017) 54–67.
- [119] H.K.M. Tanaka, T. Kusagaya, H. Shinohara, Nature Commun. 5 (2014) 3381.
- [120] D. Varga, et al., Nucl. Instrum. Methods A 958 (2020) 162236.
- [121] H.K.M. Tanaka, et al., Earth Planet. Sci. Lett. 263 (2007) 104–113.
- [122] H.K.M. Tanaka, M. Ohshiro, Geosci. Instrum. Methods Data Syst. 5 (2016) 427–435.
- [123] S. Okubo, H.K.M. Tanaka, Meas. Sci. Technol. 23 (2012) 4.
- [124] G. Ambrosi, et al., Nucl. Instrum. Methods A 628 (2011) 120–123.
- [125] F. Ambrosino, et al., J. Instrum. 9 (2014).
- [126] P. Noli, et al., Anna. Geophys. 60 (2017) 1.
- [127] L. Cimmino, et al., Anna. Geophys. 60 (2017) 1.
- [128] R. D'Alessandro, et al., Phil. Trans. R. Soc. A 377 (2018) 2137.
- [129] V. Tioukov, et al., Sci. Rep. 9 (2019) 6695.
- [130] G. Gallo, et al., Nucl. Instrum. Methods A 958 (2020) 162052.
- [131] D. Lo Presti, et al., Nucl. Instrum. Methods A 904 (2018) 195–201.
- [132] S. Vercellone, et al., EPJ Web Conf. 121 (2016) 1–6.
- [133] A. Barnoud, et al., Geophys. J. Int. 218 (2019) 2179–2194.
- [134] K. Jourde, et al., Sci. Rep. 6 (2016) 23054.
- [135] Y. Le Gonidec, et al., Sci. Rep. 9 (2019) 3079.
- [136] L. Malmqvist, et al., Geophysics 44 (1979) 1549–1569.
- [137] J. Klinger, et al., Int. J. Greenh. Gas Control 42 (2015) 644–654.
- [138] V.A. Kudryatsev, et al., Int. J. Greenh. Gas Control 11 (2012) 21–24.
- [139] R. Nishiyama, et al., Geophys. Res. Lett. 44 (2017) 12.
- [140] R. Nishiyama, et al., Sci. Rep. 9 (2019) 6970.
- [141] H.K.M. Tanaka, Nuclear Phys. B (Proc. Suppl.) 243–244 (2013) 239–248.
- [142] H.K.M. Tanaka, H. Muraoka, Geosci. Instrum. Method Data Syst. 2 (2013) 145–150.
- [143] F. Hivert, et al., E3S Web Conf. 4 (2014) 01003.
- [144] K. Jourde, et al., Sci. Rep. 6 (2016) 1–10.
- [145] S. Aguilar, et al., X Latin American Symposium on Nuclear Physics and Applications (X LASNPA), 2013.

- [146] K. Morishima, et al., *Nature* 552 (2017) 386–390.
- [147] E. Caffau, F. Coren, G. Giannini, *Nucl. Instrum. Methods A* 385 (1997) 480–488.
- [148] G.G. Barnafoldi, et al., *Nucl. Instrum. Methods A* 689 (2012) 60–69.
- [149] G. Baccani, et al., *Universe* 5 (2019) 34.
- [150] H.K.M. Tanaka, et al., *Nucl. Instrum. Methods A* 555 (2005) 164–172.
- [151] W.B. Gilboy, P.M. Jenneson, N.G. Nayak, *Radiat. Phys. Chem.* 74 (2005) 454–458.
- [152] K. Chaiwongkhot, et al., *IEEE Trans. Nucl. Sci.* 65 (2018).
- [153] F. Ambrosino, et al., *JINST* 10 (2015).
- [154] L.J. Schultz, et al., *NIMA* 519 (2004) 687.
- [155] P. Checchia, *Pure Math. Appl.* 20 (1–2) (2009) 127–139.
- [156] M. Benettoni, et al., *JINST* 8 (2013) P12007.
- [157] T.B. Blackwell, V.A. Kudryavtsev, *JINST* 10 (2015) T05006.
- [158] C. Morris, et al., *AIP Adv.* 2 (2012) 042128.
- [159] M.S. Mitra, P.K. Sarkar, V.A. Kudryavtsev, *Nucl. Instrum. Methods A* 604 (2009) 684.
- [160] D. Mitra, K. Day, M. Hohlmann, *IEEE Nucl. Sci. Symp. Med. Imag. Conf.*, 2014.
- [161] M. Stapleton, et al., *JINST* 9 (2014) P11019.
- [162] M. Bandieramonte, et al., *J. Phys. Conf. Ser.* 608 (2015) 012046.
- [163] C. Thomay, et al., *JINST* 11 (2016) 03008.
- [164] S. Chatzidakis, et al., *J. Appl. Phys.* 123 (2018) 124903.
- [165] L. Frazão, et al., *JINST* 14 (2019) P08005.
- [166] E. Åström, et al., *JINST* 11 (2016) P0701.
- [167] <https://www.decisionsciences.com/our-product/>.
- [168] K. Nagamine, et al., *Proc. Japan Acad. B* 81 (2005) 257.
- [169] Jan Sauerwald, et al., Technical Contribution to the 6th International Congress on the Science and Technology of Ironmaking - ICSTI, 42nd International Meeting on Ironmaking and 13th International Symposium on Iron Ore, Rio de Janeiro, RJ, Brazil, 2012.
- [170] G. Gustafsson, UU-NF 05#08 uppsala university neutron physics report (ISSN: 1401-6269) 2005.
- [171] D. Poulson, et al., *Nucl. Instrum. Methods A* 842 (2017) 48.
- [172] A. Clarkson, et al., *Nucl. Instrum. Methods A* 745 (2014) 138.
- [173] A. Clarkson, et al., *Nucl. Instrum. Methods A* 746 (2014) 64.
- [174] A. Clarkson, et al., *JINST* 10 (2015) P03020.
- [175] <https://www.lynkeos.co.uk/>.
- [176] LANL report LA-UR-13-28292.
- [177] D. Ancius, et al., ESARDA 41st Annual Meeting, Symposium on Safeguards and Nuclear Material Management, 14–16 2019, Stresa (Italy) 142.
- [178] J.M. Durham, et al., *Phys. Rev. Appl.* 9 (2018) 044013.
- [179] P. Checchia, et al., IAEA Symposium on International Safeguards CN267-048, 2018.
- [180] G. Bonomi, et al., *Meas. Sci. Technol.* 30 (2019) 045901.
- [181] A. Zenoni, et al., arXiv:1403.1709, 2014.
- [182] A. Donzella, *Il Nuovo Cimento C* 37 (2014) 223–232.
- [183] S. Procureur, *NIMA* 878 (2018) 169–179.
- [184] V. Blobel, *NIMA* 566 (2006) 5–13.
- [185] ALICE collaboration, *JINST* 5 (03) (2010) P03003.
- [186] The CMS collaboration, *JINST* 5 (3) (2010) T03020.
- [187] The CMS collaboration, *JINST* 9 (6) (2014) P06009.
- [188] V. Karimäki, T. Lampén, F.P. Schilling, *IEEE Trans. Nucl. Sci.* 53 (6) (2006) 3830–3833.
- [189] R. Frühwirth, *NIMA* 262 (1987) 444–450.
- [190] E. Widl, R. Frühwirth, W. Adam, CERN CMS Note, 2006, 2006/022.
- [191] V. Blobel, C. Kleinwort, F. Meier, *Comput. Phys. Comm.* 182 (9) (2011) 1760–1763.
- [192] V. Blobel, E. Lohrmann, Teubner, ISBN 3-519-03242-0, 1998.
- [193] V. Blobel, C. Kleinwort, *Advanced Statistical Techniques in Particle Physics. Proceedings, Conference, Durham, UK, March 18–22, 2002, 2002, hep-ex/0208021*.
- [194] C.C. Paige, M.A. Saunders, *SIAM J. Numer. Anal.* 12 (4) (1975) 617–629.
- [195] G. Flucke, et al., *JINST* 3 (09) (2008) P09002.
- [196] The CMS collaboration, CMS TDR 5, 1998, CERN-LHCC-98-006.
- [197] The CMS collaboration, CMS TDR 5, 2000, Addendum 1, CERN-LHCC-2000-016.
- [198] The CMS collaboration, *JINST* 5 (3) (2010) T03009.
- [199] The CMS collaboration, CMS TDR 8.1, 2006, CERN-LHCC-2006-001.
- [200] The CMS collaboration, *JINST* 8 (04) (2013) P04013.
- [201] The CMS collaboration, *JINST* 5 (2010) T03001.